The Antarctic Circumpolar Current: Dynamics of a circumpolar channel with blocked geostrophic contours

Der Antarktische Zirkumpolarstrom: Dynamik in einem zirkumpolaren Kanal mit blockierten geostrophischen Konturen

---

Daniel Borowski

Ber. Polarforsch. Meeresforsch. 453 (2003)
ISSN 1618 - 3193

Daniel Borowski

Stiftung Alfred-Wegener-Institut
für Polar- und Meeresforschung
in der Helmholtz-Gemeinschaft
27515 Bremerhaven

Die vorliegende Arbeit ist die inhaltlich unveränderte Fassung einer Dissertation, die im März 2003 dem Fachbereich Physik der Universität Bremen vorgelegt wurde.

Contents

Übersicht

Die Dynamik des Antarktischen Zirkumpolarstroms unterscheidet sich fundamental von der des restlichen Weltozeans. In den geographischen Breiten der Drake Passage ist der Ozean zonal nicht durch Kontinente begrenzt, und daher ist die Sverdrup Theorie nicht anwendbar. Jedoch werden die meisten geostrophischen Konturen an der Drake Passage durch Kontinente blockiert, und daraus ergibt sich eine wichtige dynamische Bedingung für die Vorticity-Gleichung der vertikal gemittelten Strömung.

Die meisten globalen gekoppelten Ozean-Atmosphäre Klimamodelle erzeugen einen modellierten ACC Transport der nicht mit den auf Beobachtungen basierenden Schätzungen übereinstimmt. Mit einem besseren Verständnis der Dynamik des ACCs in grobauflösenden Modellen könnte vielleicht auch die Darstellung des ACCs in gegenwärtigen Klimamodellen verbessert werden.

Diese Arbeit widmet sich den dynamischen Balancen f"uhrender Ordnung der Strömung eines geschichteten zirkumpolaren Kanals mit blockierten geostrophischen Konturen in einem grobauflösenden numerischen Modell. Die Effekte des thermohalinen und des Windantriebs auf die großräumige Zirkulation, sowie die Sensitivität gegenüber Parameteränderungen werden untersucht.

Der Transport über einen merdionalen, die geostrophischen Konturen blockierenden Rücken ist in der niedrigsten Ordnung durch den JEBAR-Effekt bestimmt. In den in dieser Arbeit betrachteten Konfigurationen folgt daraus eine meridionale Impuls-Balance erster Ordnung zwischen dem meridionalen Gradienten der baroklinen potentiellen Energie und dem zonalen, vertikal integrierten Transport. Der zirkumpolare Transport ist also durch die Dichte-Verteilung bestimmt, und diese wird im wesentlichen von drei Prozessen beeinflußt: a) die Dichteänderungen an der Oberfläche, die in einem meridionalen Dichtegradienten resultieren, b) die Konvergenz des Ekman Transportes, der das Dichtesignal in göẞere Tiefen bringt, c) und den Transporten durch meso-skalige Eddies, die diesen Gradienten abbauen. Ein vereinfachtes, analytisches Modell wird entwickelt, das in der Lage ist, die qualitative Abhängigkeit des zirkumpolaren Transportes vom thermohalien und vom Windantrieb zu reproduzieren.

Bezüglich der Sensitivität gegenüber Parameteränderungen läßt sich folgendes sagen: Die lokale meridionale Impuls-Balance ist bei allen untersuchten Konfigurationen näherungsweise geostrophisch. Doch die zonal integrierte zonale Impuls-Balance zeigte sich sensitiv gegenüber Änderungen der horizontalen Viskosität. Mit einer hohen Viskosität ist der zonale Impuls-Eintrag des Windes durch Reibung und mit niedrigen Viskositäten durch den Bottom Form Drag balanciert. Gleichzeitig ändert sich die Strömung des Kanals von einer mehr oder weniger zonalen zu einer mäandrierenden Strömung und dann zu einer mäandrierenden Strömung mit zwei großen Wirbeln stromabwärts des meridionalen Rückens. Der zirkumpolare Transport nimmt in der Stärke deutlich ab. Diese Sensitivität der Strömung gegenüber Änderungen der horizontalen Viskosität ist auch abhängig von anderen Parametern, wie der meridionalen Ausdehnung des Kanals und der Parameterisierung der Eddy-induzierten Transporte. Mit einem low-order Modell wird die zugrundeliegende Dynamik in einer vereinfachten Form untersucht.

Abstract

The Antarctic Circumpolar Current is governed by unique dynamics. Because the latitude belt of Drake Passage is not zonally bounded by continents, the Sverdrup theory does not apply to the Antarctic Circumpolar Current. However, most of the geostrophic contours are blocked at Drake Passage, which provides an important dynamic constraint for the vorticity equation of the depth averaged flow.

Most global coupled ocean-atmosphere general circulation climate models produce an ACC transport that is clearly not in agreement with the estimates based on observations. A better understanding of the dynamics of the ACC of coarse resolution models could help to improve the representation of the ACC in current climate models.

This thesis addresses the leading order dynamical balances of a stratified circumpolar current with blocked geostrophic contours in coarse resolution numerical models. The effects of thermohaline and wind forcing on the large scale transport and the sensitivity of the flow to parameter variations are studied.

The transport across a meridional ridge blocking the geostrophic contours is to leading order determined by a balance between barotropic advection of planetary vorticity and the joint effect of baroclinicity and relief (JEBAR) at that meridional ridge. For the configurations studied in the present thesis this implies a leading order meridional momentum balance between the meridional gradient of the baroclinic potential energy and the zonal, depth integrated transport. Thus, the total transport is determined by the density field, which is set up by the action of a) surface buoyancy flux which results in a meridional density gradient, b) convergence of Ekman transport that brings the density signal to larger depths, and c) meso-scale eddies that transport buoyancy downgradient. A simplified analytical model is developed that reproduces the qualitative dependence of the circumpolar current transport on the imposed thermohaline and wind forcing.

The local meridional momentum balance was approximately geostrophic for all configurations studied in this thesis. But, the zonally integrated zonal momentum balance turned out to be sensitive to the horizontal eddy viscosity within the parameter range studied. The zonally integrated zonal wind stress was balanced by horizontal friction for high viscosities and by bottom form drag for low viscosities. Parallel to the shift from a frictional to a geostrophic zonal momentum balance the flow changed from a more or less zonal flow to a meandering flow and then to a meandering flow with a double gyre circulation downstream of the ridge. The magnitude of the total channel transport was substantially decreased. The sensitivity of the flow to a variation of the horizontal eddy viscosity depends on other parameters like the meridional extent of the channel and the parameterization of the eddy tracer fluxes. A low-order model is used to study the dynamics connected with the parameter sensitivities in a more simplified form.

Chapter 1

Introduction and Motivation

1.1 Why to bother about ACC dynamics?

What is the connection of the specialized topic of the dynamics of the Antarctic Circumpolar Current (ACC) with questions of more general interest in climate physics, namely the processes governing energy fluxes in the climate system? To clarify this connection, the rôle of the global oceans for the global climate and the rôle of the Southern Ocean and the ACC for the global ocean circulation are discussed in the following two subsections. The subsequent evaluation of the performance of state of the art climate models in representing the ACC demonstrates the need of improving the understanding of ACC dynamics.

1.1.1 Global oceans and climate change

The ocean is of significant importance in the context of the climate change discussion for at least the following three reasons:

1. The ocean is one major sink of atmospheric CO_2 (see Prentice et al. (2001)) and a suitable representation of the ocean carbon processes is essential for a reliable projection of the atmospheric CO_2 concentration and thus of the radiative forcing.

2. Due to the large heat capacity of the world oceans, the time scales of climate change and climate variability are largely controlled by ocean heat storage (see Stocker et al. (2001)).

3. The global ocean circulation is responsible for a significant amount of the total (atmospheric plus oceanic) poleward heat transport. This results in a reduction of the pole-to-equator temperature gradient and influences the global radiative energy balance (see Stocker et al. (2001)).

During the last decades, the oceanic heat transport by the global thermohaline circulation (THC) and its stability have been subject of intensive study. The THC consists of a poleward surface flow of warm water in the North Atlantic (the Gulf Stream System), the formation of North Atlantic Deep Water (NADW) within the subpolar North Atlantic, a deep southward flow of NADW, upwelling of water in the Pacific Ocean, the Indian Ocean, and the Southern Ocean, and the closure of the circulation by surface return flows into the Atlantic (e.g., Broecker (1991), Schmitz (1995), and Gordon (1996)). The THC is thought to be responsible for the relatively mild climate in Northern Europe; a shutdown of the THC would result in a drastic cooling in this region with tremendous economic and societal consequences.

Stommel (1961), Broecker et al. (1985), Bryan (1986), and Hughes & Weaver (1994) showed that the THC could possibly have more than one stable mode of operation. The hypothesis of a THC operating on different stable modes has been applied to changes and variability in paleo climate (e.g., Stocker & Wright (1991), Rahmstorf (1994), Weaver & Hughes (1994), Broecker (1997), Stocker & Marchal (2000), and Ganopolski & Rahmstorf (2001)). The possibility of a complete shutdown of the THC induced by anthropogenic greenhouse gas emissions is discussed e.g. by Manabe & Stouffer (1993), Broecker (1997), Stocker & Schmittner (1997), Dixon et al. (1999), and Joos et al. (1999). The stability of the THC is, due to its severe potential impacts one of the central questions within the present climate change discussion. The possible effects of the processes occurring within the Southern Ocean on the stability of the THC are addressed in the next subsection. In addition, the Southern Ocean may play a leading rôle in regulating the atmospheric CO_2; however, this is still controversial (see e.g., Anderson et al. (2002)).

1.1.2 The Southern Ocean and the global circulation

The ACC is, with a volume transport of about 130 Sv (see Rintoul et al. (2001), $1\,\mathrm{Sv} \mathrel{\widehat{=}} 10^6\,\mathrm{m}^3/\mathrm{s}$) through the Drake Passage and a horizontal extent of 24.000 km one of the most energetic ocean currents. As pointed out in the overview of Rintoul et al. (2001), the absence of land barriers in the latitude band of Drake Passage has profound consequences on the climate of the Southern Ocean as well as the global climate. On one hand, the ACC connects all major ocean basins and distributes water mass properties, nutrients, and organisms within the Southern Ocean zonally around Antarctica. On the other hand, a net geostrophic meridional flow can not exist across the unblocked latitudes of the ACC. The result is a partial thermal isolation of the Antarctic continent from warmer waters north of the ACC and contributes to conditions suitable for the formations of Antarctic Bottom Water (AABW). Thus there are various ways, by which the processes of the Southern Ocean could stabilize or destabilize the global THC:

- **The AABW-NADW seesaw:** Stocker et al. (1992), Stocker (1998), Broecker (1998), Fieg & Gerdes (2001), Brix (2001), and Brix & Gerdes (2002) discuss indications from coarse resolution ocean models and some proxy data for a possible anticorrelation of the formation rates of AABW and NADW, sometimes phrased as the seesaw effect. Thus an enhanced AABW formation could weaken the NADW formation and could therefore reduce the THC. However, the seesaw effect is still under debate and the physical mechanisms that could result in such an effect are not yet fully understood.

- **The Drake Passage effect:** Toggweiler & Samuels (1993, 1995) found in their coarse resolution ocean model a close connection of the westerly winds at the latitudes of the Drake Passage and the formation of NADW, the so called Drake Passage effect. The physical explanation goes as follows: The northward Ekman transport due to the westerly winds at the Drake Passage latitudes must be balanced by a southward return flow. A net geostrophic southward flow across the unblocked latitudes is only possible at depth intersected by topography. To feed such a deep southward return flow, light near surface waters must be converted into deep dense water masses, which could only occur through the formation of NADW, so the interpretation of Toggweiler & Samuels (1995). However, high resolution models and observations indicate an eddy driven southward return flow at shallower depth (e.g., Rintoul et al. (2001) and Olbers & Ivchenko (2001)). Thus, by disregarding eddy processes in their coarse resolution model, Toggweiler & Samuels (1995) could well have overestimated the Drake Passage effect. Secondly, the stated connection between the Southern Ocean westerlies and the formation of NADW is also be weakened by the inclusion of an atmospheric feedback mechanism into the model, as shown by Rahmstorf & England (1997).

- **Interocean exchange:** The current picture of the global THC offers two possible return paths of water masses back into the North Atlantic: (*a*) The warm water route, westwards through the Indonesian Throughflow, the Indian Ocean, and the Agulhas Leakage around South Africa (see Gordon (1985, 1986, 1996), Gordon et al. (1992), and the review of De Ruijter et al. (1999)), and (*b*) the cold water route, eastwards with the ACC through the Drake Passage, entering the Falkland/Malvinas Current and the Brazil-Malvinas Confluence Region, where a small fraction of the waters becomes then entrained into the South Atlantic subtropical gyre (e.g., Rintoul (1991), Schmitz (1995), Park & Gamberoni (1997), and Boebel et al. (1999)). Weijer et al. (1999, 2001), and Weijer (2000) investigated the impacts of interocean fluxes of heat and salt on the strength and stability of the THC. They found the present-day interocean exchange to stabilize the present northern sinking THC, where especially the Indian-Atlantic exchange through the Agulhas Leakage turned out to be an important stimulus. This supports the ideas of Gordon et al. (1992), where the Indian-Atlantic interocean exchange is suggested to play a key rôle in the global THC.

Though the processes of the Southern Ocean certainly do have impacts on the stability of the global THC, and though these processes are closely connected to the ACC dynamics in general (Rintoul et al. (2001)), it is less clear whether the ACC itself could have an important rôle for the stability and strength of the THC. The ACC advects the water masses of the Southern Ocean around Antarctica. But for the ACC to contribute to an interbasin exchange of global water masses the water masses must be first advected towards the ACC, they must then be mixed into the ACC and must later (after being advected with the ACC) spread away from the ACC to enter the ocean basins. The interocean exchange from the Indian Ocean to the Atlantic Ocean mainly occurs through the Agulhas Leakage (De Ruijter et al. (1999)) and not through the ACC. The ACC takes part in the exchange from the Pacific Ocean to the Atlantic Ocean, but to enter the South Atlantic the water masses of the ACC must be entrained into the subtropic gyre through eddy mixing (Boebel et al. (1999)). Thus, the impacts of the ACC on the interbasin exchange of global water masses do more rely on indirect and second order effects, and the exact strength of the ACC must not necessarily be very important for the stability of the global THC.

1.1.3 The representation of the ACC in climate models

The ACC transport of state of the art coupled climate models considered in the most recent IPCC report (see McAvaney et al. (2001)) and of a selection of ocean-only models are given in tables 1.1 and 1.2, respectively. The model results are spread over a large interval surrounding the estimate based on observations. The reasons for this diversity of model results are not fully understood. But wind forcing and thermohaline processes (e.g., Cai & Baines (1996), and Gent et al. (2001)), model resolution and the representation of topography (Best et al. (1999) and Ivchenko, pers. comm.), as well as the parameterization of subgrid scale tracer fluxes (e.g., Danabasoglu & McWilliams (1995), and Fritzsch et al. (2000)) are known to be important factors. McAvaney et al. (2001) note that it is not clear whether transport errors have appreciable effects on the models atmospheric climate or on the models climate change response. Nevertheless, one would demand that a state of the art coupled ocean-atmosphere general circulation model should produce a reasonable ACC transport, since the ACC is one of the most energetic global ocean currents. The question of the rôle of the ACC in the global climate system can only be answered on the basis of a reasonable representation of the ACC in climate models. A better understanding of the dynamics of the ACC and of the factors determining the ACC transport could help to improve the ability of the climate models to produce a reasonable ACC.

MODEL NAME	ACC TRANSPORT	REFERENCE
ARPEGE/OPA1	60 Sv	Guilyardi & Madec (1997)
ARPEGE/OPA2	143 Sv	Barthelet et al. (1998a,b)
CCSR/NIES	200 Sv	Emori et al. (1999)
CGCM1	62 Sv	Boer et al. (2000) Flato et al. (2000)
COLA1	10 Sv	Schneider et al. (1997) Schneider & Zhu (1998)
CSIRO Mk 2	103 Sv	Gordon & O'Farrell (1997)
CSM 1.0	236 Sv	Boville & Gent (1998)
CSM 1.3	178 Sv	Boville et al. (2001)
ECHAM1/LSG	100 Sv	Cubasch et al. (1992) von Storch (1994) von Storch et al. (1997)
ECHAM3/LSG	112 Sv	Cubasch et al. (1997) Voss et al. (1998)
ECHAM4/OPYC3	122 Sv	Roeckner et al. (1996)
GFDL_R15_a	70 Sv	Manabe et al. (1991) Manabe & Stouffer (1996)
GISS1	75 Sv	Miller & Jiang (1996)
GOALS	74 Sv	Wu et al. (1997) Zhang et al. (2000)
HadCM2	216 Sv	Johns (1996) Johns et al. (1997)
HadCM3	204 Sv	Gordon et al. (2000)
IPSL-CM1	66 Sv	Braconnet et al. (2000)
IPSL-CM2	164 Sv	Laurent et al. (1998)
MRI1	50 Sv	Tokioka et al. (1996)
MRI2	83 Sv	Yukimoto et al. (2000)
NCAR1	79 Sv	Meehl & Washington (1995) Washington & Meehl (1996)
NRL	66 Sv	Hogan & Li (1997) Li & Hogan (1999)
OBSERVED	123 Sv	Whitworth & Peterson (1985)

Table 1.1: Volume transport of the ACC, diagnosed from the set of coupled ocean-atmosphere general circulation models (AOGCMs) considered in the Third Assessment Report (TAR) of the Intergovernmental Panel on Climate Change (IPCC), see McAvaney et al. (2001).

coarse resolution ocean models:		
MODEL NAME	ACC TRANSPORT	REFERENCE
BG02 CTRL	236 Sv	Brix & Gerdes (2002)
CB96 1IW	120 Sv	Cai & Baines (1996)
CB96 2IW	75 Sv	Cai & Baines (1996)
GH00 BA	207 Sv	Gnanadesikan & Hallberg (2000)
NCAR GLB01 A	120 Sv	Gent et al. (2001)
NCAR GLB01 B	117 Sv	Gent et al. (2001)
NCAR GLB01 C	250 Sv	Gent et al. (2001)
NCAR GLB01 D	231 Sv	Gent et al. (2001)
OMIP-HOPE	88 Sv (Jan) to 97 Sv (Sep)	Fritzsch et al. (2000)
OMIP-MOM2	91 Sv (Jan) to 99 Sv (Sep)	Fritzsch et al. (2000)
OMIP-MOM2 V1.3	170 Sv	Fritzsch et al. (2000)
OMIP-MOM2 V1.4	< 60 Sv	Fritzsch et al. (2000)

eddy permitting and eddy resolving models:		
MODEL NAME	ACC TRANSPORT	REFERENCE
FRAM	195 Sv	The FRAM Group (1991) Webb et al. (1991)
OCCAM - 1/4°	152 Sv	Webb et al. (1997)
POP11	136 Sv	Maltrud et al. (1998)
SC92 - 1/2°	180 Sv	Semtner & Chervin (1992)
SC92 - 1/4°	163 Sv	Semtner & Chervin (1992)

Table 1.2: Volume transport of the ACC, diagnosed from ocean-only models.

1.2 What is so special about ACC dynamics?

Despite of its not fully understood rôle in the global climate system, the ACC is a worthwhile subject of study for its unique dynamics, which result from the existence of unblocked latitudes (see Rintoul et al. (2001) for a recent overview). In the following, some of the peculiarities of ACC dynamics are restated and an important dynamical constraint is introduced: the existence of blocked geostrophic contours the ACC must cross. This dynamical constraint partly mitigates the lack of zonal boundaries.

1.2.1 Upsetting the Sverdrup balance

With the exception of the Southern Ocean and the central Arctic Ocean, all major oceans are zonally bounded by continents, preventing zonal currents to encircle the globe along latitude circles. This fact is utilized by the classical Sverdrup Theory to calculate the barotropic circulation within ocean basins from the wind stress curl. This is done by integrating the Sverdrup balance

$$\beta \frac{\partial \Psi}{\partial x} = \frac{1}{\rho_0} \operatorname{curl}_z(\vec{\tau}) \tag{1.1}$$

eastwards along constant latitudes (see e.g. Pedlosky (1996) for a textbook). Here, Ψ is the barotropic streamfunction, β the meridional gradient of the Coriolis frequency f, $\vec{\tau}$ the wind stress, and ρ_0 a constant reference density. The condition of no flow across the continental boundary is implemented by setting the streamfunction Ψ to an arbitrary constant value along the continental boundary. To close the circulation, western boundary currents are added.

Balance (1.1) is valid over a flat bottom and applies to the steady state large scale circulation outside boundary layers. A more general form can be obtained from the vertically integrated momentum balance:

$$-f\vec{\nabla}\Psi = -\vec{\nabla}\chi - \frac{H}{\rho_0}\vec{\nabla}p_b + \frac{1}{\rho_0}\vec{\tau} - \vec{G} \tag{1.2}$$

(where χ is the baroclinic potential energy (see subsection 2.2.2 and 2.2.3), H the depth of the ocean, p_b the pressure at the bottom, and $\vec{G}$ collects the nonlinear and frictional terms). Taking the curl of (1.2) gives the vorticity balance of the steady state vertically integrated flow:

$$\beta \frac{\partial \Psi}{\partial x} = \mathcal{J}(p_b, H) + \frac{1}{\rho_0} \operatorname{curl}_z(\vec{\tau}) - \operatorname{curl}_z\left(\vec{G}\right) \tag{1.3}$$

where $\mathcal{J}(A, B)$ is the Jacobian of A and B. Outside boundary layers, the last term on the rhs may be disregarded, and the first term on the rhs (the bottom pressure torque) vanishes for zero topographic elevation or zero geostrophic bottom flow across topographic contours. In closed basin geometry, the interior deep geostrophic flow across topography is cut off due to the propagation of baroclinic Rossby waves (e.g., Anderson & Gill (1975), Pedlosky (1996), and Rintoul et al. (2001)) and since (1.3) then simplifies to (1.1) the Sverdrup Theory is applicable to closed basins.

In the Southern Ocean, the situation is fundamentally different. Due to the presence of unblocked latitudes, the condition of no flow across continental boundaries cannot be used to limit the zonal transport. As pointed out by Hughes (1997), since (1.1) alone only determines the meridional but not the zonal transport, any circumpolar zonal flow that does not intersect topography can be added without violating the Sverdrup balance - this flow is not constrained by (1.1) and is referred to as the so called free mode. Thus, within the framework of classical Sverdrup Theory, the calculation of the circulation within the Southern Ocean becomes ambiguous. Thus either friction or the bottom pressure torque (or both and/or nonlinear advection) must be present somewhere at every unblocked latitude to balance the wind stress curl.

With respect to the cut off of the deep flow across topography due to the westward propagation of baroclinic Rossby waves, the eastward background transport with the ACC is of the same order of magnitude as the westward group velocity of the baroclinic Rossby waves, and the above mechanism is thus not efficient within the Southern Ocean (e.g., Hughes (1996), Killworth et al. (1997), Hughes et al. (1998), and Rintoul et al. (2001)). The bottom pressure torque must thus not vanish within the Southern Ocean, and in their analysis of the vorticity budget of the FRAM model Wells & de Cuevas (1995) indeed found the bottom pressure torque to be a leading term at many places within the Southern Ocean. Therefore, the Sverdrup balance is not applicable to ACC dynamics.

Despite the above facts, some authors used to propose the application of the Sverdrup Theory to the Southern Ocean, however, in a modified form. Stommel (1957) suggested that the island arc made up by the South Shetland - South Orkney - South Sandwich islands could be considered as an effective extension of the Antarctic Peninsula which blocks the latitudes of the Drake Passage. The ACC is then suggested to consist of an eastern boundary current in the eastern Scotia Sea, a western boundary current in the western Argentine Basin and a Sverdrup-balanced current elsewhere, whereby the introduction of an eastern boundary current into the Sverdrup Theory is controversial from a dynamical point of view. To obtain an estimate for the ACC transport one then only needs to integrate (1.1) from South America eastwards to the Scotia Island Arc. Baker (1982) observed, within experimental uncertainties, a quantitative (but rather crude) agreement of Stommel's theory with observational estimates. More recent promoters of Stommel's ideas are Warren et al. (1996).

However, as emphasized by Olbers (1998), in any multiply connected domain, like the Southern Ocean, the difference of the streamfunction between the boundaries, here Antarctica and South America, is not determined solely by the vorticity balance (1.3).

The dynamical system must be completed by an additional dynamical constraint. Applying the Island Rule of Godfrey (1989) (originally Kamenkovich (1961)) this can be achieved with the closed integral of the momentum balance (1.2) along a closed path encircling Antarctica (e.g., Olbers (1998) and Hughes (2002)).

Webb (1993) proposed an ACC model, which relates the ACC transport to the northward Ekman transport instead of the wind stress curl. This model is reformulated by Hughes (2002) and is placed together with Stommel (1957) in the context of Sverdrup-like models of the ACC. In the formulation of this review, a northern barrier (i.e., South America) and an effective southern barrier (i.e., the Scotia Island Arc in Stommel's model, and the Kerguelen Plateau in Webb's model) do zonally overlap, and the bottom is taken to be flat. Both models assume western boundary currents at the northern barrier, but with respect to the southern barriers the two models differ. Stommel's model assumes an eastern boundary current at the southern barrier and implies that the ACC transport is determined by the wind stress curl. Webb's model assumes western boundary currents for both barriers and implies that the ACC transport is determined through Godfrey's Island Rule by the zonal wind stress. In this light, the above indeterminateness of the streamfunction difference could be related to the question of assuming eastern or western boundary currents (or both) at the southern continental barrier. Hughes (2002) combines the two models of Stommel (1957) and Webb (1993) within a generalized model which now includes bottom topography and shows for this generalized model that the question of whether the ACC transport is determined by the wind stress curl or by the wind stress itself does depend on the spatial distribution of bottom form drag.

1.2.2 The importance of form drag

Within ACC dynamics the bottom form drag is important to balance the input of zonal momentum through the wind stress at the surface. Integrating the momentum balance (1.2) along a closed unblocked latitude circle yields:

$$\frac{1}{\rho_0}\oint p_b \frac{\partial H}{\partial x}\,\mathrm{d}x + \frac{1}{\rho_0}\oint \tau^x\,\mathrm{d}x - \oint G^x\,\mathrm{d}x = 0 \tag{1.4}$$

where τ^x and G^x are the x-components of $\vec{\tau}$ and $\vec{G}$, respectively. For flat bottom cases, the first term on the lhs (the bottom form drag) vanishes and the wind stress can then only be balanced through the effects collected in $\vec{G}$. As can be seen from Munk & Palmén (1951), Hidaka & Tsuchiya (1953), and Gill (1968), a balance between the wind stress and friction (applied to the ACC) would either require unrealistic high values for the eddy viscosity or would result in unrealistic high transport values - the so called Hidaka's Dilemma (Wolff et al. (1991)). The currently accepted solution to this problem is the inclusion of topography and then a balance between the bottom form drag (first term on the lhs) and the wind stress (second term on the lhs). This balance was first proposed by Munk & Palmén (1951) and was confirmed for high resolution ocean models by Gille (1997) and Stevens & Ivchenko (1997). (For the bottom form drag to become non zero, the bottom pressure can not be a function of topography height only and a zonal phase shift in the Fourier series is needed.)

A question that then arises is that of how the zonal momentum which is input at the surface can be transferred down to the ocean floor where it is taken up by the bottom form drag. Munk & Palmén (1951) suggested this to be done through the meridional overturning circulation. Another candidate is the interfacial form drag, nicely illustrated in Johnson & Bryden (1989). Just as the momentum can be transferred between ocean and sea floor by a phase shift of bottom topography and bottom pressure, it can be transferred between isopycnal layers by a phase shift of isopycnal height and pressure along the isopycnals. Such a zonal phase shift is connected with a meridional transport of buoyancy. By completely ascribing this meridional buoyancy transport as well as the interfacial form drag to the action of meso-scale transient eddies, and by applying the parameterizations for baroclinic instability processes of Green (1970) and Stone (1962, 1972), Johnson & Bryden (1989) obtained a theoretical estimate of the shear transport of the ACC.

However, quasigeostrophic models (e.g., Treguier & McWilliams (1990), and Wolff et al. (1991)) and high resolution 3-D models (e.g., Stevens & Ivchenko (1997) and Olbers & Ivchenko (2001)) show, that the vertical momentum transfer occurs through both, transient as well as standing eddies, and the theory of Johnson & Bryden (1989) is in this respect uncomplete. Standing eddies are here introduced as the zonal deviation from the zonal mean and can be illustrated as the steady spatial meandering of the flow or as standing waves in the displacement of the isopycnals. A modified Johnson & Bryden theory which includes a diagnosis of standing eddies is proposed by Olbers & Ivchenko (2001).

The vertical momentum transfer through standing eddies is addressed within an analytically solvable low-order model by Völker (1995, 1999), and Olbers & Völker (1996). In analogy to atmospheric blocking (see Charney & DeVore (1979), Charney & Straus (1980), and, for an introductory textbook, (James, 1994, section 8.6)), Völker applies the mechanism of baroclinic topographic resonance to a zonally periodic ocean channel (as an idealization of the ACC): The eastward wind stress accelerates a zonal flow which excites baroclinic Rossby waves by interaction with bottom topography. For a suitable flow speed, these waves become trapped by the counteraction of advection and wave propagation, and with a suitable phase shift theses waves can support an interfacial and bottom form drag that prevents a further acceleration of the flow.

The process of blocking by barotropic or baroclinic topographic resonance is more commonly known from atmospheric literature. Another such process (which is reported for ACC dynamics but more commonly known from the atmosphere) is the upgradient eddy transfer of zonal momentum by Reynolds stress, the so called negative viscosity effect[1]. Beside the non applicability of Sverdrup Theory, the similarity of certain processes to atmospheric processes is the second major feature unique to ACC dynamics.

1.2.3 Blocked geostrophic contours

Geostrophic contours (i.e. contours of constant f/H) are important dynamic characteristics for the depth integrated flow. By dividing (1.2) by H and taking the curl thereafter, one obtains the vorticity equation of the steady state depth averaged flow:

$$\mathcal{J}\left(\Psi, \frac{f}{H}\right) = \mathcal{J}\left(\chi, \frac{1}{H}\right) - \mathrm{curl}_z\left(\frac{\vec{\tau}}{\rho_0 H}\right) + \mathrm{curl}_z\left(\frac{\vec{G}}{H}\right) \tag{1.5}$$

The first term on the rhs is called the JEBAR term and represents the combined effects of baroclinicity and topography on the depth integrated flow. (e.g., Mertz & Wright (1992)). In the absence of baroclinicity and forcing, the flow would have to follow geostrophic contours, but in a stratified ocean the circulation can decouple from the geostrophic contours (e.g., Marshall (1995a,b), Hughes & Killworth (1995), and Cane et al. (1998)).

Figure 1.1 shows that most of the geostrophic contours in the Southern Ocean are blocked at Drake Passage, which provides an important dynamic constraint for the vorticity equation (1.5). The fundamental rôle of blocked geostrophic contours can be illustrated by the barotropic model of Krupitsky & Cane (1994) and Wang & Huang (1995). In a homogeneous zonally periodic channel with topography, they observed two different dynamical regimes, depending on the height of a meridional ridge placed across the channel. If the height of the ridge is below a critical value, some of the geostrophic contours close through the periodic continuation of the channel. For a

---

[1] McWilliams et al. (1978), Treguier & McWilliams (1990), and Wolff et al. (1991) found in quasi-geostrophic ocean channel models that the Reynolds stress tends to redistribute momentum horizontally with a zero net effect and thereby contributes to an intensification of the zonal flow in the center of the channel. Due to the interaction with the zonal jet, the eddies are tilted in such a manner that the net transport of eastward zonal momentum is directed towards the center of the jet (e.g., Wolff et al. (1991), Wardle & Marshall (2000), or, for references to atmospheric literature, Starr (1948) and (James, 1994, section 5.2)). An upgradient transport of zonal momentum was also observed in high resolution ocean models (e.g., Hughes (1996), Ivchenko et al. (1996), Stevens & Ivchenko (1997), and Best et al. (1999)). However, the negative viscosity effect occurred more locally, especially in regions of very strong jets. Several parameterizations of eddy transports are able to produce upgradient momentum fluxes (e.g., Ivchenko (1984), Wardle & Marshall (2000), Olbers et al. (2000), and Wolff (1999)). The analysis of altimeter data by Johnson et al. (1992), Morrow et al. (1992), and Morrow et al. (1994)) tends to confirm the picture of a negative viscosity effect within the Southern Ocean, but, more recently, Hughes & Ash (2001)) reassessed the data and put this picture to a challenge.

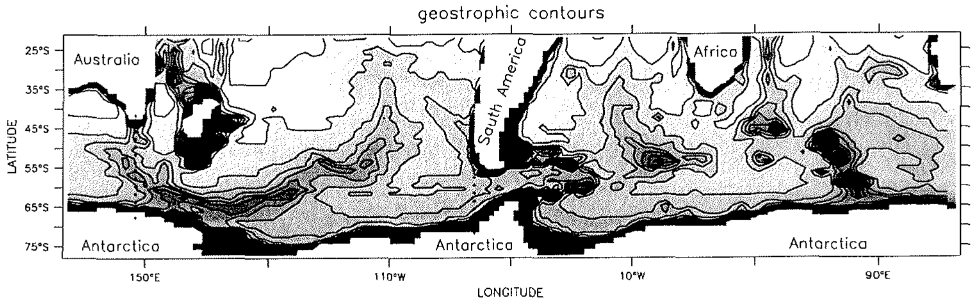

Figure 1.1: Geostrophic contours (f/H) in the Southern Ocean. There are two prominent regions where geostrophic contours are blocked by continents: The region between Australia and Antarctica, and Drake Passage between South America and Antarctica. Here, the ACC must cross geostrophic contours. Although the geostrophic contours are not blocked there, the ACC also crosses the geostrophic contours at the East Pacific Rise and several other locations.

circumpolar current that follows these closed contours, balance (1.5) reduces to a balance between the last two terms on the rhs. Strong zonal jets result in accordance with Hidaka's Dilemma. If the height exceed the critical value, all geostrophic contours are blocked either by the northern or the southern boundary of the channel (or both), and no circumpolar current following any single geostrophic contour can exist. In Krupitsky & Cane (1994) and Wang & Huang (1995) the flow is then substantially weaker and must be closed through boundary layer currents. Utilizing the self-similarity of the ACC in the vertical found by Killworth (1992) (see also Killworth & Hughes (2002)) and developing an equivalent barotropic model of the ACC Krupitsky et al. (1996) extended the application of these ideas to a stratified ocean by effectively reducing the height of topographic elevations. The equivalent barotropic model is quantitatively assessed in Ivchenko et al. (1999).

The existence of blocked geostrophic contours within the Southern Ocean is in the center of this thesis, and the ACC is considered as a current across such contours. In Chapter 2, a circumpolar flow is sought that can cross blocked geostrophic contours without being closed through strong boundary layer currents.

1.3 The problems addressed in this thesis

Subject of this thesis is to further the understanding of the dynamics of the Antarctic Circumpolar Current (ACC). As an idealization of the ACC, a circumpolar channel with blocked geostrophic contours is used, and various coarse resolution numerical experiments are conducted to study the dynamics of such a channel. In this thesis the notion "coarse resolution" is used for horizontal grid sizes that are clearly larger than the first baroclinic Rossby radius. Thus, in coarse resolution models the realization of meso-scale eddies is not possible. Due to the high degree of idealization, the coarseness of the numerical model, and various general problems with numerical representations of physical processes, one must be very cautious with transferring the results to the dynamics of the real ACC. But, since observational data are very sparse, and since controlled experiments on global scale are neither feasible nor justifiable, one must to a certain extent rely on idealized model results. By including more realistic model configurations and by comparing the model results with observations and results from high resolution models, the applicability to the ACC is discussed. The use of a coarse resolution has two main reasons. First, with the limited computer capacity (one always has), a larger variety of experiments can be archived by using coarse resolutions. Second, all current coupled climate models are using coarse resolutions for the ocean component, and to improve the representation of the ACC in these models, one must understand the ACC of coarse resolution ocean models.

The following aspects are addressed in this thesis:

- Various models demonstrate the importance of both, thermohaline and wind forcing of the ACC, and point to an interaction between the thermohaline and wind driven circulation (e.g., Cai & Baines (1996), Gnanadesikan & Hallberg (2000), and Gent et al. (2001)). These effects are studied in chapter 2. There, the channel transport is found to be largely determined by meridional density gradients. The wind can substantially influence the channel transport through its effects on the density field. The chapter has previously been published in Borowski et al. (2002), and preliminary work has been done in Borowski (1999).

- Ocean models usually contain a number of parameters whose values can not be completely determined from observations or (for reasons of numerical stability) must be set clearly outside the range supported by observations. For example, especially coarse resolution ocean models often require unrealistically high values for the "eddy viscosity". In chapter 3 the sensitivity of the flow of a zonally periodic channel on a variation of the eddy viscosity is studied. Both, the shape as well as the strength of the flow, turned out to depend strongly on the values chosen for the viscosity. The dynamical balances are studied to get some insights into the physics of the observed changes.

- In chapter 4 the sensitivity of the channel flow to a variation of the horizontal eddy viscosity and other parameters is studied from the point of view of the theory of dynamical systems. To do so, a modified version of the low-order model of Völker (1995), Olbers & Völker (1996), and Völker (1999) is used. With this model it is possible to study the channel dynamics in a highly simplified form and to concentrate on processes that are relevant in this context.
- Chapter 5 summarizes the discussion of the previous chapters and sketches some recommendations that could be given on the basis of this thesis to increase the reliability of the representation of the ACC in climate models.

Chapter 2

Thermohaline and wind forced flows in channel geometry

2.1 Introduction

In the recent years much interest has been attributed to the effects of topography and stratification on the transport of the Antarctic Circumpolar Current (ACC). Attention has been drawn to the question of how the circulation can decouple from the contours of f/H (e.g. Marshall (1995b), Krupitsky et al. (1996) and Ivchenko et al. (1999)) and of how the momentum input by surface wind stress can be transferred down to the ocean floor (e.g. Johnson & Bryden (1989), Treguier & McWilliams (1990), Wolff et al. (1991), Ivchenko et al. (1996), Olbers (1998) and Völker (1999)). Taking a slightly different perspective, Olbers & Wübber (1991), Cai & Baines (1996), Samelson (1999), Gnanadesikan & Hallberg (2000), and Gent et al. (2001) pointed out the active rôle of stratification in driving the ACC. The physical mechanism discussed in the last few papers is appealingly simple (basically geostrophy), evidence from numerical models can be found as early as in Gill & Bryan (1971), and the theoretical concepts involved are known for a long time (e.g. Rattray & Dworski (1978) and Mertz & Wright (1992)).

Samelson (1999) proposed a simple analytical theory for the steady state, large scale geostrophic circulation of a stratified fluid in the Gill & Bryan (1971) geometry of a rectangular basin with a circumpolar connection. The abyssal interior fluid is assumed to be stagnant and the thermal wind equation is applied to determine the channel transport. Beside convective adjustment to maintain static stability, Samelson (1999) neglected mixing of tracers all together. Thus he found the vertical structure of the stratification to depend on the imposed thermal surface forcing and the geometry, but not on the wind forcing, and he did not observe any influence of the wind forcing on the channel transport. However, Toggweiler & Samuels (1995, 1998), McDermott (1996), Gnanadesikan (1999) and Vallis (2000) discuss, how the wind affects deep stratification, which in turn would influence the baroclinic contribution to the channel transport as well.

In their illustrative numerical study Cai & Baines (1996) observed strong interactions between the thermohaline and the wind driven circulation in the Southern Ocean. Driving an ocean model both by thermohaline (restoring to SST and SSS) and wind forcing, they obtained an ACC with a depth integrated transport significantly stronger than the sum of the transport of a pure wind driven (homogeneous) and a pure thermohaline driven ocean model. By analyzing the zonally and vertically integrated momentum balance Cai & Baines (1996) identified the bottom form stress as the term responsible for driving the ACC in the pure thermohaline driven ocean. Considering the case of a thermohaline and wind driven ocean Cai & Baines (1996) argued that, while the direct effect of the wind forcing on the ACC is small, a wind induced enhancement of the bottom form stress could be responsible for the additional forcing driving the ACC. Though this numerical study is an enlighting demonstration of an indirect wind effect on the ACC, the physical explanation must be rejected. The proposed mechanism of a bottom form stress driving the ACC and lateral friction balancing the bottom form stress is inconsistent with the findings of Stevens & Ivchenko (1997) and Gille (1997) in eddy resolving models, which support the balance proposed by Munk & Palmén (1951) instead. The balance found by Cai & Baines (1996) must be ascribed to the unrealistic strong lateral friction used in this study.

More recently, Gnanadesikan & Hallberg (2000) investigated the effects of Southern Hemisphere winds on the ACC using a two layer model with interface restoring and a coarse resolution General Circulation Model. They argued that the northward Ekman flux of light water connected with increased eastward winds within the Southern Ocean would produce a deeper pycnocline and warmer deep water in the subtropics of the Southern Hemisphere. This in turn results in a much larger thermal wind shear across the Circumpolar Current. By assuming relatively small near bottom velocities an increase in ACC transport can be derived. Their discussion of the dynamical balance left one question open: the assumption of a nearly motionless abyss might be consistent with model results and observations, but nevertheless it would be desirable to give dynamical reasons for the claim that the contribution of the bottom flow to the ACC transport is negligible.

This chapter investigates the effects of the thermohaline and the wind forcing on the large scale steady state transport in a circumpolar channel with blocked geostrophic contours (i.e. contours of f/H), which serves as a model of the ACC. This is done by using three coarse resolution General Circulation Models with different geometries and by employing some analytical arguments to the model geometries. In particular a indirect wind effect similar to the one proposed by Gnanadesikan & Hallberg (2000) is supported, but matters are treated differently in two important respects: firstly, instead of using the assumption of a motionless abyss, some consequences of blocked geostrophic contours and vorticity conservation are worked out. Thereby a more complete discussion of the dynamic balance is offered in section 2.2. Secondly, the thermodynamic balance is treated in a more simplified way. The possible feed back of the Southern Ocean winds through their impact on the North Atlantic Deep Water formation is disregared, and the focus is put on the wind effects that take place mainly within the Southern Ocean region. This simplified treatment in section 2.3 allows to formulate a simple analytical model, which is able to reproduce the qualitative dependence of the channel transport on wind forcing, thermohaline forcing, and diffusion parameters.

2.2 Balancing the channel flow

2.2.1 A zonally periodic channel with topography

In the following a idealized model of a channel flow across topography is used (see figure 2.1), which includes the important dynamical feature of blocked geostrophic contours. This model is a zonally periodic channel, that extends from 55°S to 65°S and covers 80° longitude. The depth of the channel is 4000 m, and a meridional ridge with a zonal extent of L is arranged to block the deep part of the passage. At the center of the ridge the depth reduces to H_{Top}, where three different values have been used in various configurations (see table 2.1). In all configurations, the geostrophic contours are blocked at the ridge (as sketched in figure 2.2) and the channel flow must cross the geostrophic contours at the ridge.

2.2.2 Vorticity conservation and channel transport

The transport across geostrophic contours is constrained by the vorticity equation of the depth averaged flow. Assuming the hydrostatic approximation, the Boussinesq approximation as well as the rigid lid approximation, and summarizing the frictional and the nonlinear terms in a vector $\vec{G}$, the steady state vorticity equation of the depth averaged flow can be written as:

$$\vec{\nabla}\frac{f}{H}\cdot\vec{U} = \mathcal{J}\left(\chi, \frac{1}{H}\right) + \frac{f}{H}\vec{\nabla}\cdot\vec{U}_{\mathrm{Ek}} + \vec{\nabla}\frac{f}{H}\cdot\vec{U}_{\mathrm{Ek}} + \mathrm{curl}_z\left(\frac{\vec{G}}{H}\right) \tag{2.1}$$

where the vertically integrated transport $\vec{U}$, the baroclinic potential energy χ, and the Ekman transport $\vec{U}_{\mathrm{Ek}}$ are used:

$$\vec{U} = \int_{-H}^{0} \vec{u}\,\mathrm{d}z \;=\; \vec{k}\times\vec{\nabla}\Psi \;; \qquad \chi = \frac{g}{\rho_0}\int_{-H}^{0} z\,\rho'\,\mathrm{d}z \;; \qquad \vec{U}_{\mathrm{Ek}} = -\frac{1}{\rho_0 f}\vec{k}\times\vec{\tau}$$

Here $\mathcal{J}(A,B)$ is the Jacobian of A and B, $\vec{u}$ the horizontal velocity field, Ψ the streamfunction, g is the gravitational acceleration, ρ' the density ρ minus a horizontal

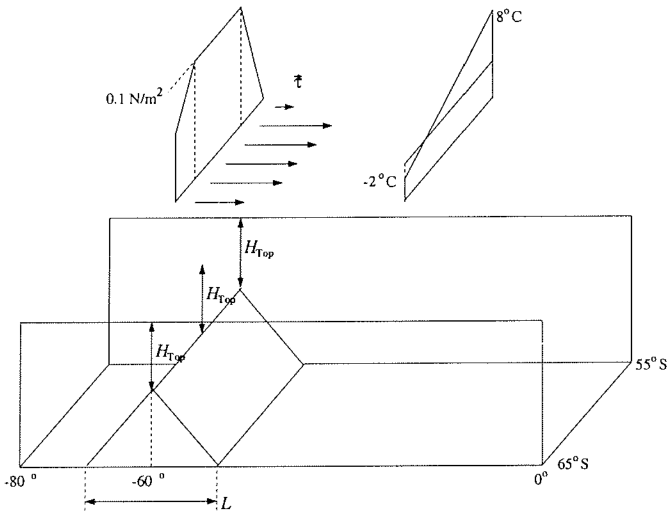

Figure 2.1: Geometry of the zonally periodic channel with topography. The flow in this channel is forced by eastward wind stress and an imposed south-north temperature gradient at the surface (see upper panel). The channel flow must cross the geostrophic contours that are blocked at the topographic barrier.

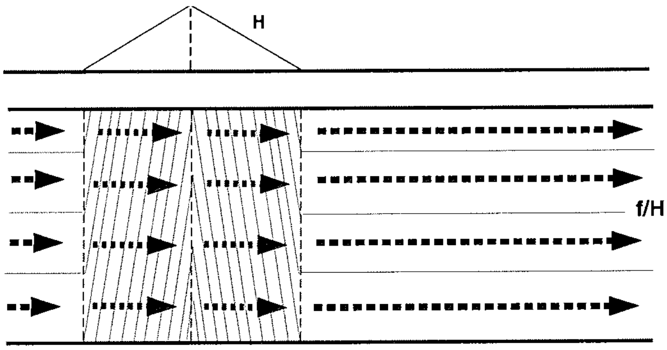

Figure 2.2: Topography H (upper panel) and geostrophic contours f/H (thin solid lines, lower panel) of the zonally periodic channel with topography (figure 2.1). At the topographic obstacle, the circumpolar current within this channel (dashed arrows) must cross geostrophic contours.

mean density profile $\bar{\rho}$, ρ_0 a constant reference density, $\vec{\tau}$ the surface wind stress, z the vertical coordinate, and $\vec{k}$ the unit vertical vector.

Equation (2.1) expresses the transport across geostrophic contours (lhs) in terms of the JEBAR term (first term on the rhs), the divergence of the Ekman transport (second term on the rhs), the Ekman transport across geostrophic contours (third term on the rhs), and frictional as well as non linear effects (last term on the rhs). It is assumed that frictional and nonlinear effects can only become relevant within narrow boundary layer currents. Thus $\vec{G}$ can be neglected in the interior. The Joint Effect of Baroclinicty and Relief (JEBAR) is discussed e.g. in Mertz & Wright (1992), it represents the difference between the bottom pressure torque and that which would occur if bottom pressure gradients were equal to depth-averaged pressure gradients. In the case of blocked geostrophic contours (as assumed in this thesis) the complete transport through the channel must be balanced by the terms on the rhs of (2.1).

The question then is, which of the rhs terms of (2.1) can generate a substantial transport not only across geostrophic contours but also across the meridional ridge of the channel. Figure 2.3 is an illustration of (2.1). If there is any transport across the meridional ridge, the lhs of (2.1) must change sign at the top of the ridge. This is sketched in the upper left panel of figure 2.3. Thus, in order to obtain a substantial transport across the ridge, the rhs of (2.1) must change sign in a corresponding manner. This must be due to one or more of the following effects expressed by the terms of the rhs:

- **JEBAR:**

  With a predominantly meridional density gradient (as found in the climatological state of the ACC) the JEBAR term changes sign at the top of the ridge (see upper right panel of figure 2.3). Thus a flow across the meridional ridge (as sketched in the upper left panel of figure 2.3) can be balanced by the JEBAR term, and a substantial circumpolar channel transport can be generated by meridional density gradients.

- **Ekman divergence:**

  Assuming an upward Ekman pumping within the whole area of the channel (see lower right panel of figure 2.3), the Ekman divergence has an uniform sign. The resulting flow would converge over the meridional ridge, but would not cross it (lower left panel of figure 2.3). In order to obtain a substantial circumpolar transport across the ridge, one would either need to include further effects (e.g. frictional effects within boundary layer currents), or a special wind stress field, where the Ekman divergence term would change the sign in a manner suitable to the topography. The transport within a homogeneous, zonally periodic β-channel with topography (similar to the one used here), where the current is driven by Ekman pumping, was investigated by Krupitsky & Cane (1994) and

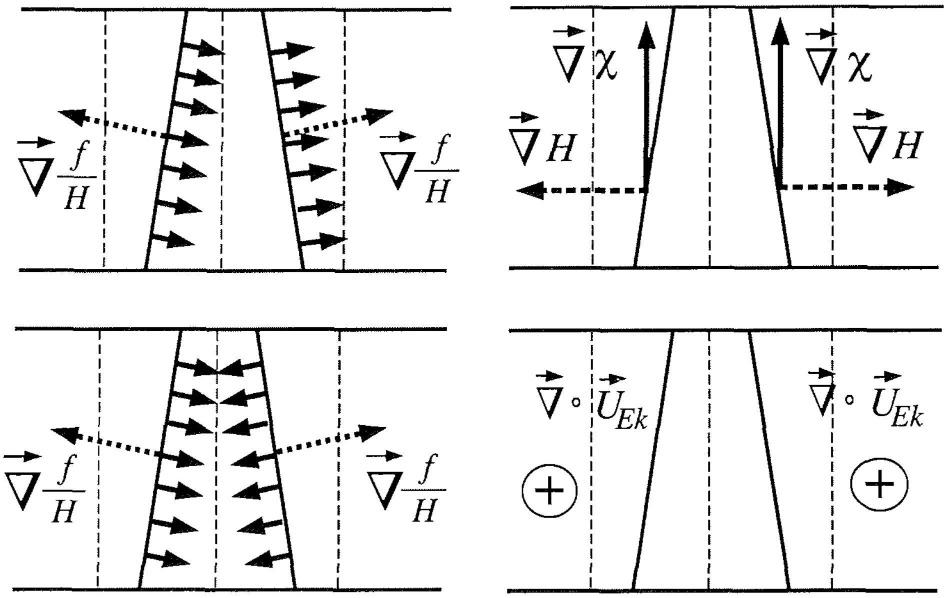

Figure 2.3: Illustration of equation (2.1) for the zonally periodic channel. All four panels show two selected geostrophic contours (thick solid diagonal lines) at the meridional ridge (indicated by thin dashed vertical lines - compare with figure 2.2). The two left panels illustrate the lhs of (2.1). The dashed arrows display the gradient of f/H and the normal components of the transport across geostrophic contours are sketched by the small solid arrows. The upper left panel depicts the case, where the lhs of (2.1) changes sign at the top of the ridge, and the lower left panel the case, where the sign of the lhs of (2.1) remains constant. The JEBAR term is sketched in the upper right panel (where dense water is assumed at the south, near the pole, and lighter water is assumed to the north, towards the equator). $\vec{\nabla}H$ changes sign at the top of the meridional ridge and thus the JEBAR term changes sign, too. In the lower right panel the second term of the rhs of (2.1) is sketched for the case of upward Ekman pumping within the whole area. The sign of this term is constant. A forcing as sketched in the upper right panel would result in a flow as sketched in the upper left panel, and a forcing as sketched in the lower right panel would result in a flow as sketched in the lower left panel.

Wang & Huang (1995). They obtained a circumpolar channel current which was mainly restricted to very narrow frictional boundary layer currents at the southern and northern walls, joined by a narrow jet along a particular geostrophic contour. Choosing a ridge height of a realistic value for the Southern Ocean, the models of Krupitsky & Cane (1994) and Wang & Huang (1995) would lead to a channel transport of only a few Sv, which is not realistic for the ACC transport.

- **Ekman transport:**

  The Ekman transport across geostrophic contours (third term on the rhs of (2.1)) can in principle generate a transport across the meridional ridge. But assuming, consistent with the conditions within the Southern Ocean, a wind stress which is mostly eastward, the Ekman transport is mostly northward. In such a case it does not substantially contribute to the channel transport.

- **Nonlinear and frictional effects:**

  Nonlinear and frictional effects can be relevant within boundary layer currents only. The are dominant in the experiments of Krupitsky & Cane (1994) and Wang & Huang (1995), where the channel transport occurs in the boundary layers. However, in the numerical model experiments considered in the present chapter, a dynamic regime is realized in which the transport is not dominated by boundary currents, and thus the nonlinear and fritional terms turned out to be (to leading order) negligible in the dynamic balance (see subsections 2.2.4, 2.2.5 and 2.3.1).

Concluding the discussion above, it is suggested that a circumpolar current with blocked geostrophic contours can most efficiently be driven by meridional density gradients, and the channel transport is to leading order determined by the distribution of the baroclinic potential energy χ. At the meridional ridge, where the geostrophic contours are blocked, an approximate balance of the transport across geostrophic contours and the JEBAR term is proposed:

$$\vec{\nabla}\frac{f}{H}\cdot\vec{U}=\mathcal{J}\left(\Psi,\frac{f}{H}\right)\approx\mathcal{J}\left(\chi,\frac{1}{H}\right) \tag{2.2}$$

A circumpolar current which is dominantly driven by baroclinic effects is consistent with the findings of Gill & Bryan (1971), Olbers & Wübber (1991), Marshall (1995b), Cai & Baines (1996), Samelson (1999), and Gnanadesikan & Hallberg (2000).

2.2.3 Shear transport and deep transport

Among others, Samelson (1999) and Gnanadesikan & Hallberg (2000) estimated the transport of the Antarctic Circumpolar Current using the thermal wind equation. If the abyssal velocities are small compared to the depth averaged velocities, this approach will lead to satisfactory results. However, Samelson (1999) and Gnanadesikan & Hallberg (2000) did not provide any dynamical arguments, why the abyssal velocities should be small. Here, some ideas concerning the deep flow are promoted and an estimate for the deep transport across geostrophic contours is given. Since the ACC must cross the geostrophic contours at some locations within the Southern Ocean, the transport across the geostrophic contours is relevant.

Now, using the thermal wind balance, the depth integrated shear transport $\vec{U}_{\mathrm{shear}}$ (relative to the bottom layer) is written as

$$\vec{U}_{\mathrm{shear}} = \frac{1}{f}\,\vec{k} \times \left(\vec{\nabla}\chi + \frac{gH}{\rho_0}\rho_{\mathrm{b}}\vec{\nabla}H\right) \tag{2.3}$$

and the deep geostrophic transport $\vec{U}_{\mathrm{deep}}$ (geostrophic bottom velocity times depth) is given by:

$$\vec{U}_{\mathrm{deep}} = \frac{H}{\rho_0 f}\,\vec{k} \times \left(\vec{\nabla}p\right)_{\mathrm{b}} \tag{2.4}$$

where $\rho_{\mathrm{b}} = \rho'\,(z = -H)$ is the bottom density, p the pressure, and $\left(\vec{\nabla}p\right)_{\mathrm{b}}$ the horizontal pressure gradient at the bottom. (Note $\left(\vec{\nabla}p\right)_{\mathrm{b}} + g\rho_b\vec{\nabla}H = \vec{\nabla}p_b$, where p_b is the bottom pressure.) The depth integrated momentum balance takes the form

$$f\vec{\nabla}\Psi = \vec{\nabla}\chi + \frac{gH}{\rho_0}\rho_{\mathrm{b}}\vec{\nabla}H + \frac{H}{\rho_0}\left(\vec{\nabla}p\right)_{\mathrm{b}} - \frac{1}{\rho_0}\vec{\tau} + \vec{G} \tag{2.5}$$

The curl of $1/H$ times this equation results in the voriticty balance (2.1). The momentum balance (2.5), on the other hand, may be expressed in terms of transports if one writes the total depth integrated transport $\vec{U} = \vec{k} \times \vec{\nabla}\Psi$ as the sum of the shear transport $\vec{U}_{\mathrm{shear}}$, the deep transport $\vec{U}_{\mathrm{deep}}$, the Ekman transport $\vec{U}_{\mathrm{Ek}}$, and an additional term allowing for nonlinear and frictional effects:

$$\vec{U} = \vec{U}_{\mathrm{shear}} + \vec{U}_{\mathrm{deep}} + \vec{U}_{\mathrm{Ek}} + \left(\frac{1}{f}\,\vec{k} \times \vec{G}\right) \tag{2.6}$$

Evaluation of the divergence of (2.6) yields an expression for the deep transport across geostrophic contours,

$$\vec{\nabla}\frac{f}{H} \cdot \vec{U}_{\mathrm{deep}} = -\frac{1}{H}\,\vec{\nabla}f \cdot \vec{U}_{\mathrm{shear}} + \frac{f}{H}\,\vec{\nabla} \cdot \vec{U}_{\mathrm{Ek}} + \frac{f}{H}\mathrm{curl}_z\left(\frac{\vec{G}}{f}\right) \tag{2.7}$$

The deep geostrophic transport across geostrophic contours is thus induced by the meridional component of the shear transport, the divergence of the Ekman transport, and frictional as well as nonlinear effects. Adding $\vec{\nabla}\frac{f}{H}\cdot\vec{U}_{\text{shear}}$ to both sides of (2.7) one obtains:

$$\vec{\nabla}\frac{f}{H}\cdot\vec{U} = -\frac{f}{H^2}\vec{\nabla}H\cdot\vec{U}_{\text{shear}} + \frac{f}{H}\vec{\nabla}\cdot\vec{U}_{\text{Ek}} + \frac{f}{H}\,\text{curl}_z\left(\frac{\vec{G}}{f}\right) \qquad (2.8)$$

and the ratio of (2.7) and (2.8) gives:

$$\frac{\vec{\nabla}\frac{f}{H}\cdot\vec{U}_{\text{deep}}}{\vec{\nabla}\frac{f}{H}\cdot\vec{U}} = \frac{\frac{1}{f}\vec{\nabla}f\cdot\vec{U}_{\text{shear}}-\Gamma}{\frac{1}{H}\vec{\nabla}H\cdot\vec{U}_{\text{shear}}-\Gamma} \qquad (2.9)$$

with:

$$\Gamma = \vec{\nabla}\cdot\vec{U}_{\text{Ek}} + \text{curl}_z\left(\frac{\vec{G}}{f}\right)$$

From (2.9) one can see:

a) If the shear transport $\vec{U}_{\text{shear}}$ is parallel to geostrophic contours, then the total transport across geostrophic contours can be completely found in the deep transport (i.e. LHS of (2.9) $= 1$);

b) if the divergence of the Ekman transport plus the fricitonal and nonlinear terms are negligible (i.e. Γ is small), then a zonal shear transport $\vec{U}_{\text{shear}}$ leads to a small contribution of the deep transport to the total transport across geostrophic contours (i.e. small LHS of (2.9));

c) if the term Γ is small, then a shear transport $\vec{U}_{\text{shear}}$, which is parallel to topographic contours, leads to a large contribution of the deep transport to the total transport across geostrophic contours (i.e. large LHS);

d) if $\Gamma = 0$ and the transport $\vec{U}_{\text{shear}}$ is parallel to contours of f/H^{α}, then LHS $= \alpha$.

The Ekman transport $\vec{U}_{\text{Ek}}$ is about two orders of magnitude smaller than the shear transport $\vec{U}_{\text{shear}}$, and the frictional and nonlinear effects are, by assumption, considered negligible outside boundary layer currents. Thus Γ can be considered small, and the LHS of (2.9) is small if $\vec{U}_{\text{shear}}$ is 'closer' to zonal than to following f/H contours, in the sense defined by d) above, i.e. if α is close to zero. In the numerical experiments of the present chapter, this condition is met at the meridional ridge of the stratified, zonally periodic channel (see subsection 2.2.4 and figure 2.7 below), as well as at some locations (relevant to our discussion) in the model with more realistic topography (see subsection 2.2.5 below). At these locations, one should expect from the discussion above a small deep transport across geostrophic contours compared to the total transport across geostrophic contours.

So far, only the component of the deep transport across geostrophic contours has been considered. Its component along geostrophic contours does not enter the arguments above. However, concentrating on the regions where the geostrophic contours are blocked, the component across the geostrophic contours is the relevant component for the circumpolar transport. Thus in the regions, where 1.) the LHS of (2.9) is small, 2.) the geostrophic contours are blocked, 3.) the Ekman transport is small compared to the total transport, and 4.) nonlinear and frictional effects can be disregarded, the total transport (or at least the component of the total transport, which contributes to the circumpolar transport) can be estimated by the shear transport,

$$\vec{U} \approx \vec{U}_{\mathrm{shear}} \tag{2.10}$$

which can be equivalently expressed in the form

$$f\vec{\nabla}\Psi \approx \vec{\nabla}\chi + \frac{gH}{\rho_0}\rho_b\vec{\nabla}H \tag{2.11}$$

Similar ideas concerning the smallness of the bottom flow are put forwards in Hughes & Killworth (1995).

Provided the channel is bounded by vertical walls, replacing f by a constant f_0 (taken at a central latitude), and integrating (2.11) along a topographic contour from the southern to the northern channel boundary, gives an approximate balance for the channel transport $\Delta\Psi$

$$\Delta\Psi \approx \frac{\Delta\chi}{f_0} \tag{2.12}$$

The balance (2.11) is the central result of this section. It is important for at least two reasons. First, it allows to calculate the barotropic transport in the case of blocked geostrophic contours from the density field alone. Second, it implies that the strength of the ACC at, say, Drake Passage is determined by the processes that establish the large scale density structure, especially the meridional density gradient. In the following two subsections, the balance (2.11) is compared with numerical results of a large suite of experiments.

2.2.4 Numerical experiments with the channel model

To test the validity of (2.11) and the arguments of the preceding subsections concerning the dynamical balance, numerical experiments with a three-dimensional primitive equation model (MOM 2; see Pacanowski (1995)) were conducted, using the geometry specified in subsection 2.2.1. Because the density field, especially the deep density field, governs (2.11) one needs integration times long enough for the density field to adjust to the imposed surface forcing. Thus, a coarse resolution model is necessary, although eddy effects, that could be important in the ACC, are then neglected. The horizontal resolution is 1° × 2° (meridional × zonal), and the length and width of the channel are 80° in longitude and 10° in latitude, respectively; the vertical is resolved by 16 levels with a spacing varying from 34 m at the surface to 300 m at 1002 m depth and an uniform spacing of 300 m below 1002 m down to 4002 m depth. The parameters of the turbulent viscosity are 10^5 m^2/s in the lateral and 10^{-3} m^2/s in the vertical direction, and the turbulent diffusivity was set to 10^{-4} m^2/s in both the lateral and vertical directions. The FCT-scheme (Gerdes et al. (1991)) was applied, which allows the use of very small lateral turbulent diffusivities. In order to minimize the integration time necessary to obtain an approximate steady state, the distorted physics technique of Bryan (1984) was applied and different time steps for the tracer and momentum variables were chosen.

Various numerical experiments were conducted, switching the thermohaline and the wind forcing on and off, as well as using different values for the geometric parameters L and H_{Top} of the meridional ridge. All experiments started with a homogeneous channel at rest and were then integrated for 2000 years to a near steady state. In the configurations with wind forcing, a zonally constant zonal wind stress with a maximum of 0.1 N/m^2 is applied (see upper panel of figure 2.1), and for the configurations with thermohaline forcing, the surface temperature is restored to a linear function of latitude with −2°C at 65°S and 8°C at 55°S, while the salinity was kept constant at 34 psu. In the configurations without thermohaline forcing, homogeneous density with a constant potential temperature of 4°C and a constant salinity of 34 psu is used. The configurations are summarized in table 2.1. The results of the numerical experiments are summarized in table 2.2 and figure 2.4.

Figure 2.6 shows the streamfunction Ψ for the configuration C2h, in which the thermohaline forcing is switched off and the channel flow is driven by wind stress only. Consistent with the results of Krupitsky & Cane (1994) and Wang & Huang (1995), and the discussion of subsection 2.2.2, the current is concentrated in boundary layers. Table 2.2 and figure 2.4 indicate a channel transport of only a few Sv for the experiments with homogeneous density.

In contrast, a substantial channel transport can be obtained by adding thermohaline forcing. Figure 2.7 shows the streamfunction Ψ and the baroclinic potential energy χ/f_0 for the configuration C2a, where thermohaline and wind forcing are used. The comparison shows an approximate correspondence of both fields. While there are small scale deviations of χ/f_0 from the streamfunction Ψ in the area of the ridge, the over all transport $\Delta\Psi$ through the channel is very well captured by $\Delta\chi/f_0$. This holds for all experiments with thermohaline forcing (see table 2.2 and figure 2.4). Both quantities differ by only a few Sv for all topographic parameters used and for wind and no wind cases. The scatter plot of the lhs of (2.12) against the rhs (figure 2.5) demonstrates that the balance (2.12) holds in these experiments.

configuration	geometric ridge parameters		imposed forcing	
	zonal extent L	depth H_{Top}	wind	thermohaline
C1a	20°	1000 m	yes	yes
C2a	20°	2000 m	yes	yes
C3a	20°	3000 m	yes	yes
C1b	20°	1000 m	no	yes
C2b	20°	2000 m	no	yes
C3b	20°	3000 m	no	yes
C1h	20°	1000 m	yes	no
C2h	20°	2000 m	yes	no
C3h	20°	3000 m	yes	no
C4a	40°	1000 m	yes	yes
C5a	40°	2000 m	yes	yes
C6a	40°	3000 m	yes	yes
C4b	40°	1000 m	no	yes
C5b	40°	2000 m	no	yes
C6b	40°	3000 m	no	yes
C4h	40°	1000 m	yes	no
C5h	40°	2000 m	yes	no
C6h	40°	3000 m	yes	no

Table 2.1: Configurations used for the numerical experiments with the channel geometry (see figure 2.1).

thermohaline and wind forcing					
configuration	$\Delta\chi/f_0$	$\Delta\Psi$	configuration	$\Delta\chi/f_0$	$\Delta\Psi$
C1a	61.23 Sv	65.47 Sv	C4a	41.78 Sv	43.70 Sv
C2a	88.26 Sv	89.38 Sv	C5a	88.08 Sv	89.06 Sv
C3a	91.85 Sv	89.18 Sv	C6a	90.72 Sv	88.13 Sv
only thermohaline forcing					
configuration	$\Delta\chi/f_0$	$\Delta\Psi$	configuration	$\Delta\chi/f_0$	$\Delta\Psi$
C1b	12.71 Sv	13.27 Sv	C4b	11.74 Sv	12.36 Sv
C2b	12.60 Sv	12.56 Sv	C5b	13.75 Sv	13.87 Sv
C3b	9.706 Sv	8.081 Sv	C6b	10.90 Sv	9.589 Sv
only wind forcing					
configuration	$\Delta\chi/f_0$	$\Delta\Psi$	configuration	$\Delta\chi/f_0$	$\Delta\Psi$
C1h	0.000 Sv	1.187 Sv	C4h	0.000 Sv	0.791 Sv
C2h	0.000 Sv	2.966 Sv	C5h	0.000 Sv	2.745 Sv
C3h	0.000 Sv	9.664 Sv	C6h	0.000 Sv	8.976 Sv

Table 2.2: Results from the numerical experiments with the channel model, using the configurations specified in table 2.1. The table compares the channel transport $\Delta\Psi$ and the baroclinic potential energy difference $\Delta\chi/f_0$. (f_0 is the Coriolis parameter at a central latitude (60°S).) See figure 2.4 for a graphical comparison.

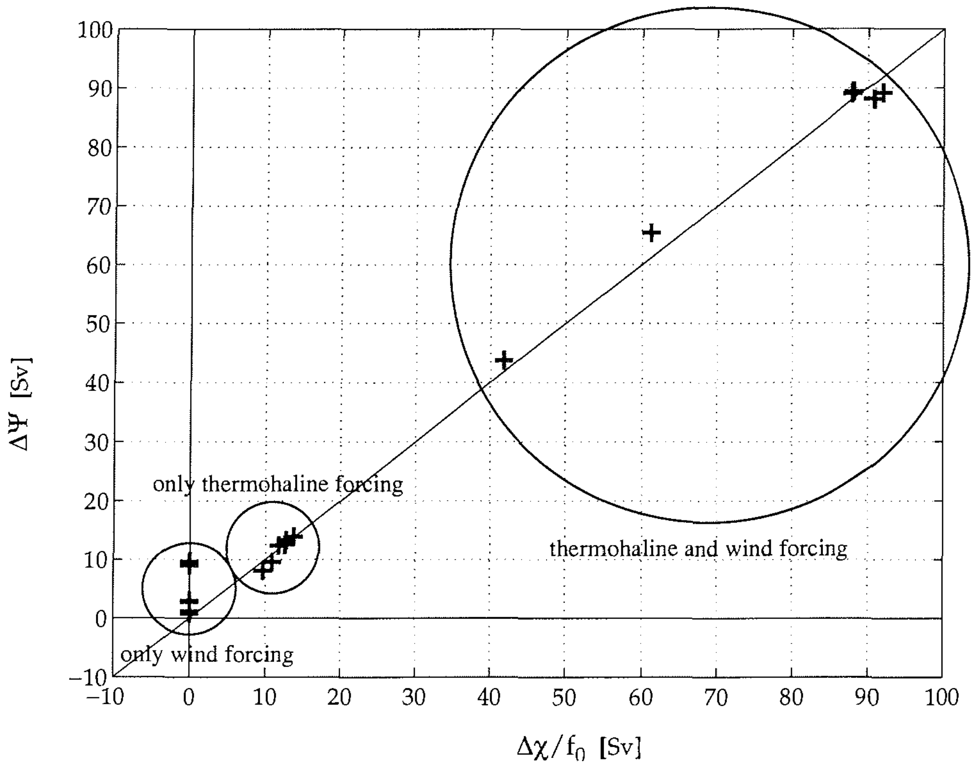

Figure 2.4: Results from the numerical experiments with the channel model, using the configurations specified in table 2.1. The plot compares the channel transport $\Delta\Psi$ and the baroclinic potential energy difference $\Delta\chi/f_0$, and indicates the experiments with 'only wind forcing', 'only thermohaline forcing', and 'thermhaline and wind forcing'. (Compare table 2.2).

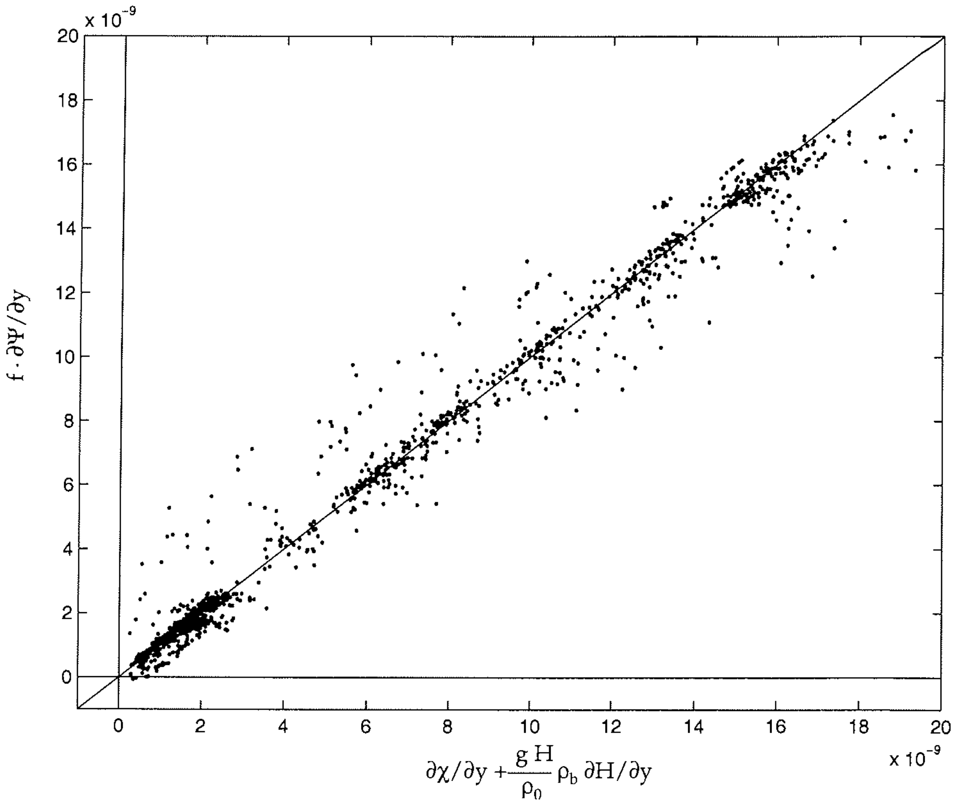

Figure 2.5: Scatter plot of (2.11) for the numerical experiments with the channel model, where thermohaline forcing was included. In this scatter plot, (2.11) was evaluated for all grid point above the topographic barrier, blocking the geostrophic contours.

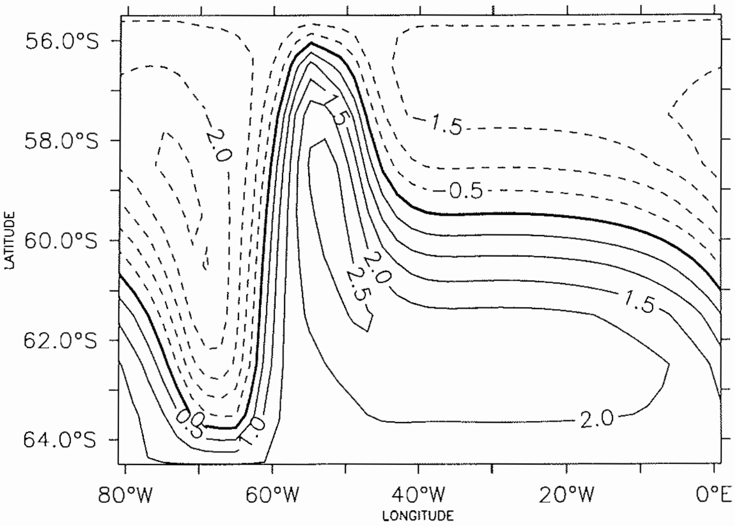

Figure 2.6: Streamfunction Ψ in Sv for the configuration C2h (homogeneous channel with wind forcing only, see table 2.1).

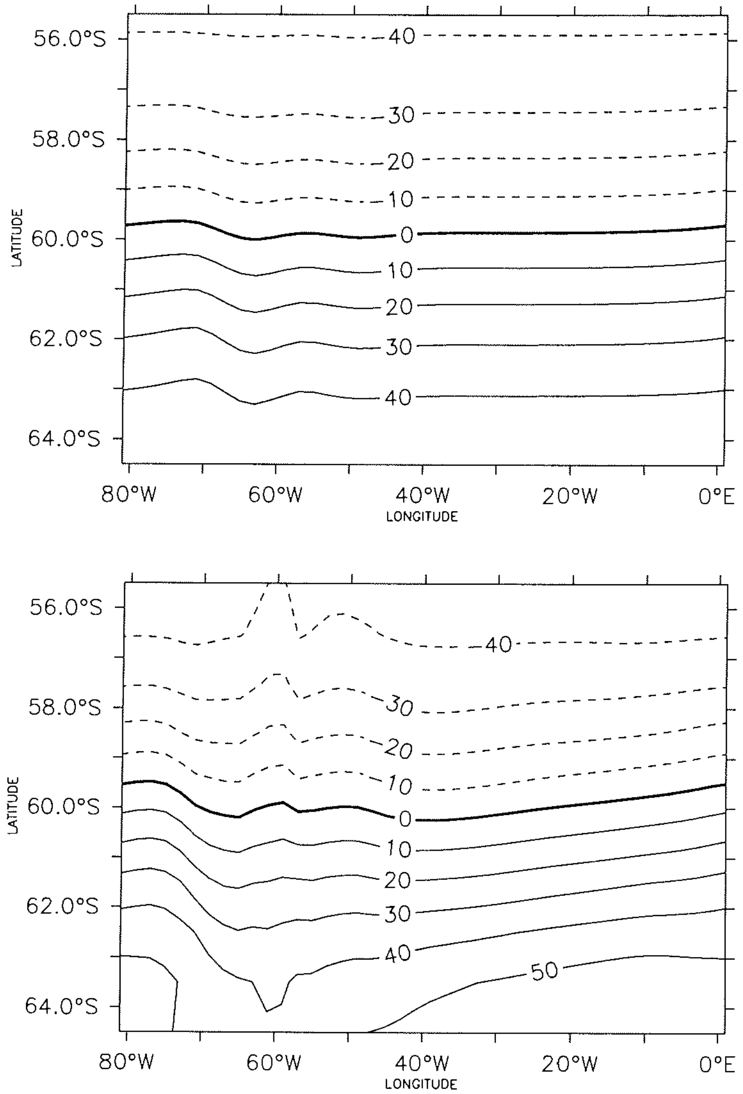

Figure 2.7: Streamfunction Ψ in Sv (upper panel) and baroclinic potential energy χ/f_0 in Sv (lower panel) for the configuration C2a (thermohaline and wind forcing are both applied, see table 2.1). f_0 is the Coriolis parameter at a central latitude (60°S).

2.2.5 A global model with realistic topography

It remains to be shown that (2.11) is useful under realistic conditions. Therefore additional experiments were conducted, using a global model with realistic topography (figure 2.8). To adequately resolve the topographic features in the Southern Ocean and especially at the Drake Passage, a spatially varying horizontal resolution is used. In the vicinity of the Drake Passage the resolution is 1° × 2° (meridional × zonal), whereas it is 3° × 4° in the Northern Pacific. The meridional extent of the model is limited by solid walls at 78° N and 78° S, where restoring zones have been supplemented, to maintain realistic water mass properties in the deep ocean. The vertical is resolved by 25 levels with a vertical spacing varying from 30 m at the surface to 300 m at a depth of 2475 m and an uniform vertical spacing of 300 m down to a depth of 5475 m. The vertical turbulent viscosity is set to 10^{-3} m^2/s, and the horizontal turbulent viscosity is proportional to the cube of the horizontal grid resolution Δx, where 10^4 m^2/s is the value at $\Delta x = 100$ km. This allows a sufficient resolution of the boundary layers as well as an optimal use of the enhanced horizontal resolution at Drake Passage. The vertical hybrid mixing scheme of Bryan & Lewis (1979), the FCT scheme discussed by Gerdes et al. (1991), and the isopycnal thickness mixing parameterization of Gent & McWilliams (1990) were implemented. A isopycnal diffusivity of 10^3 m^2/s was chosen and the isopycnal thickness diffusion coefficient was set to 10^2, $5 \cdot 10^2$, or 10^3 m^2/s for different numerical experiments (see table 2.3). Surface temperatures and salinities are restored to annual mean values from Levitus (1982). Hellerman & Rosenstein (1983) annual mean wind stresses are applied at the surface. In each numerical experiment the model was first initialized with the Levitus (1982) climatology and then run for 100 years, where again the distorted physics technique of Bryan (1984) was applied. While the adjustment of the deep density field to the surface forcing is clearly not finished after 100 years, the velocity field can be considered to be in equilibrium with the density field and wind forcing, thus the validity of (2.11) can be tested already. The configurations and results of the experiments conducted are summarized in table 2.3.

The bottom topography of the global model is much more complicated than the one of the channel model of the previous subsection. An integration of (2.11) along topographic contours to obtain (2.12) is not straightforward, and thus a direct comparison of the streamfunction Ψ with the baroclinic potential energy χ (as done for the channel model) is not appropriate for the global model. A reconstruction of the streamfunction Ψ can instead be obtained by integrating the meridional component of (2.11) in the meridional direction:

$$\Psi_{\mathrm{reconstruction}} = \Psi_{y_{\mathrm{south}}} + \int_{y_{\mathrm{south}}}^{y_{\mathrm{north}}} \frac{1}{f} \left(\frac{\partial \chi}{\partial y} + \frac{gH}{\rho_0} \rho_{\mathrm{b}} \frac{\partial H}{\partial y} \right) \mathrm{d}y \tag{2.13}$$

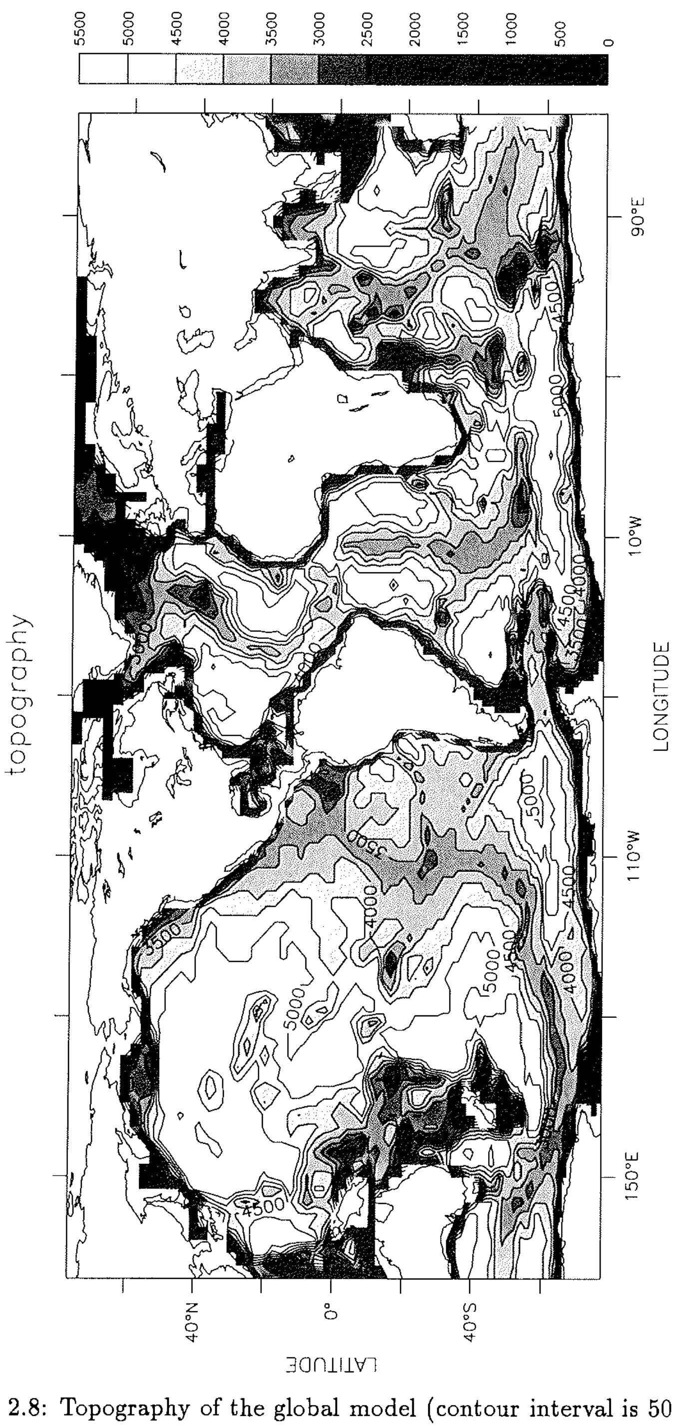

Figure 2.8: Topography of the global model (contour interval is 500 m)

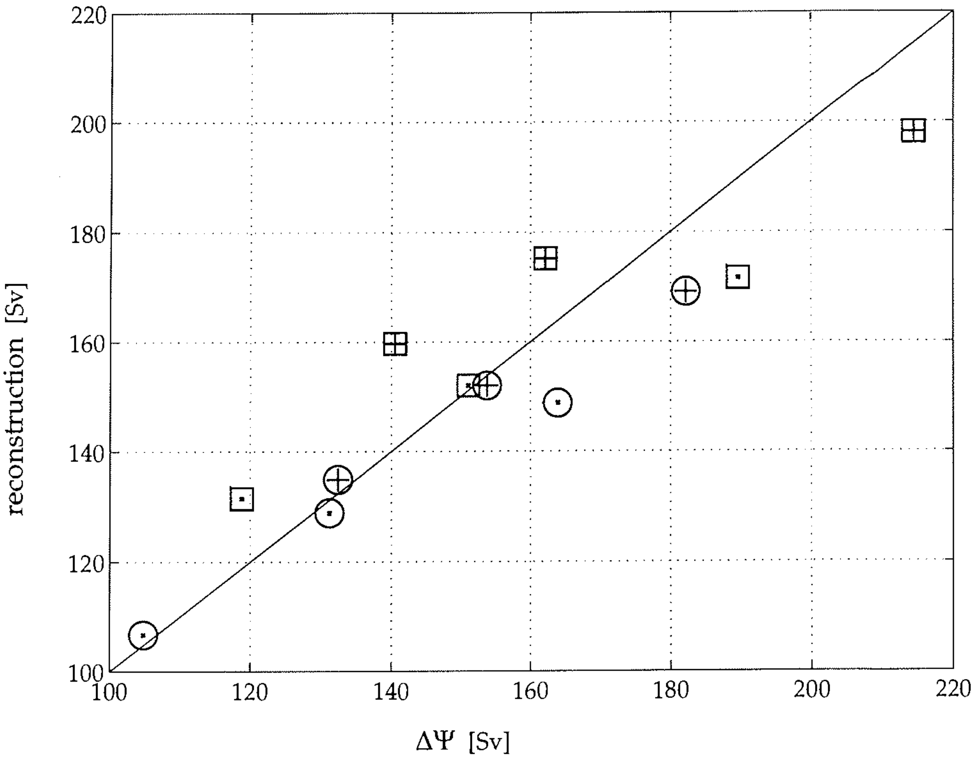

Figure 2.9: Comparison of the depth integrated transports $\Delta\Psi$ through the Drake Passage (marked by circles) and across the section between Tasmania and Antarctica (marked by squares) obtained from the model runs with estimates of the depth integrated transport derived from (2.13). The experiments with a restoring zone at the northern and the southern boundary of the model domain are labeled by "+". In the case of exact correspondence of $\Delta\Psi$ and the reconstruction by (2.13) all marks would be on the straight solid line. The observed transport $\Delta\Psi$ and the reconstruction of this transport agree within a range of about 10%.

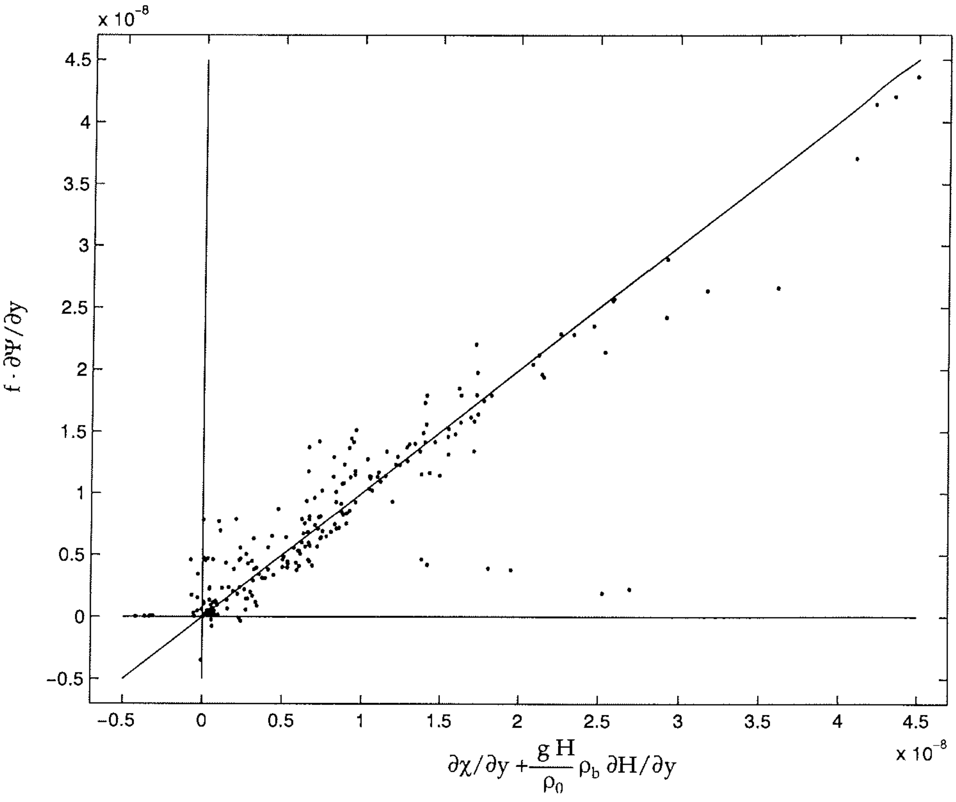

Figure 2.10: Scatter plot of (2.11) for the six experiments with the global model, evaluated at the two meridional cross sections (one near the Drake Passage and one between Tasmania and Antarctica) described in the text. The six outliners to the right of the diagonal line (one for each experiment) do all belong to the same grid point, located just south of Tasmania. There, the shear flow is not close to being zonal and is more like following f/H^{α}-contours with a negative α.

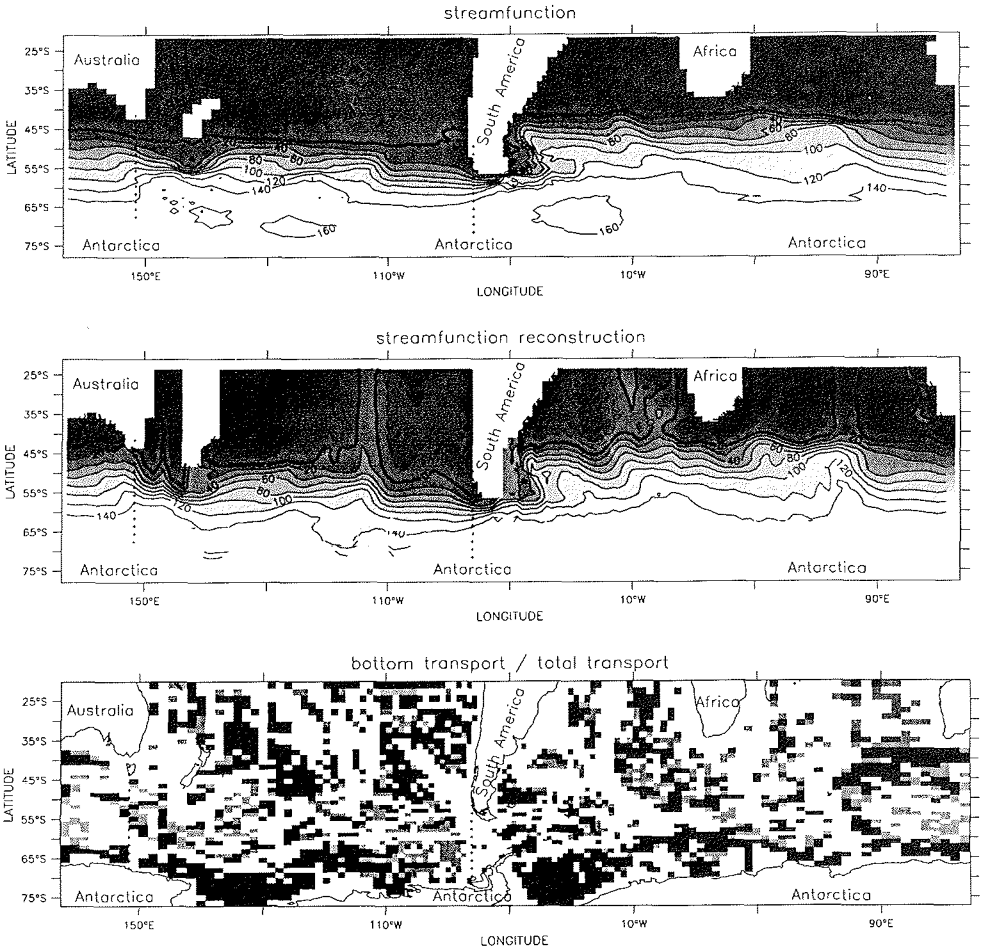

Figure 2.11: Results of the experiment G5 (see table 2.3). **Upper panel:** streamfunction Ψ in Sv. **Middle panel:** reconstruction of the streamfunction with (2.13). **Lower panel:** ratio of the magnitude of the bottom transport $\vec{U}_{\mathrm{deep}}$ (see (2.4)) and the magnitude of the total transport $\vec{U}$. In the light shaded areas this ratio is less than 10%, in the middle grey shaded areas it is between 10% and 25%, and in the dark shaded areas more than 25%. In all panels above as well as in figure 1.1 the sections chosen for the comparison of the transports $\Delta\Psi$ with the estimates of these transports with (2.13) are marked with lines of +. These sections are located between Tasmania (Australia) and Antarctica at 146° E and across the Drake Passage at 54° W.

exp.	restoring zones	A_{iso}	Tasmania		Drake Passage	
			$\Delta\Psi$	estimate	$\Delta\Psi$	estimate
G1	northern only	$0.1 \cdot 10^3\ \text{m}^2/\text{s}$	189.7 Sv	171.6 Sv	163.9 Sv	148.8 Sv
G2	northern only	$0.5 \cdot 10^2\ \text{m}^2/\text{s}$	151.1 Sv	152.0 Sv	131.2 Sv	128.9 Sv
G3	northern only	$1.0 \cdot 10^3\ \text{m}^2/\text{s}$	118.8 Sv	131.5 Sv	104.8 Sv	106.7 Sv
G4	northern & southern	$0.1 \cdot 10^3\ \text{m}^2/\text{s}$	214.3 Sv	198.1 Sv	182.2 Sv	169.1 Sv
G5	northern & southern	$0.5 \cdot 10^3\ \text{m}^2/\text{s}$	162.1 Sv	175.2 Sv	153.8 Sv	152.0 Sv
G6	northern & southern	$1.0 \cdot 10^3\ \text{m}^2/\text{s}$	140.5 Sv	159.7 Sv	132.4 Sv	134.9 Sv

Table 2.3: Summary of the configurations and results of the numerical experiments with the global model. All experiments used a 10° latitude wide restoring zone near the northern boundary. In the experiments G4 to G6 a restoring zone with a latitudenal extent of 7° was also added in the south. Different values for the isopycnal thickness diffusion coefficient A_{iso} were used. The resulting depth integrated transports $\Delta\Psi$ through the Drake Passage and across the section between Tasmania and Antarctica (see figure 2.11) are shown and compared with estimates from the density distribution with (2.13).

The streamfunction Ψ and the reconstruction of the streamfunction by (2.13) are compared in the top two panels of figure 2.11. While there are clear differences in the closed basins of the major oceans, the overall agreement of the streamfunction and its reconstruction is rather good within the ACC region. This agreement is not trivial. As argued in subsection 2.2.3, the total transport $\vec{U}$ can be obtained from the thermal wind equation if one can assume that the deep transport $\vec{U}_{\text{deep}}$ is negligible. This would immediately give (2.13) and $\Psi_{\text{reconstruction}}$ can be considered as the integral of the shear transport $\vec{U}_{\text{shear}}$. Clearly the deep transport $\vec{U}_{\text{deep}}$ is not negligible everywhere in the ocean. In subsection 2.2.3 it was found that the deep transport across geostrophic contours is small compared to the total transport across geostrophic contours, if the shear transport is 'closer' to zonal than to following geostrophic contours. At locations, where the ACC has to cross the geostrophic contours, this is the criterion that must be considered.

In subsection 1.2.3 two regions were identified where the ACC must cross geostrophic contours: Drake Passage and the region between Australia and Antarctica. In these regions the above criterion is mostly satisfied, with few exceptions: East of Drake Passage, the ACC bends to the north into the Malvinas/Falkland Current and there the flow is not zonal at all. Consequently the deep transport is responsible for more than 25% of the total transport of the Malvinas/Falkland Current (see lower panel of figure 2.11). In the western part of Drake Passage, the ACC is nearly zonal, and in this region the deep transport contributes less than 10% to the total transport.

In the region between Australia and Antarctica the shear transport has a meridional component, though moderate (see middle panel of figure 2.11); thus some contribution of the deep transport to the total transport is indicated in the lower panel of figure 2.11, but it is still less than 25% in most of the areas. In regions, where the depth integrated transport is not across but mostly along geostrophic contours, the above criterion does not apply and the deep transport can become quite strong. This is the case e.g. in the Weddell and Ross seas as well as in the vicinity of Kerguelen Plateau.

Two cross sections were selected (one in the Drake Passage region and one between Tasmania and Antarctica), where the ACC has to cross geostrophic contours and the above criterion is satisfied to a reasonable degree. These selected cross sections are indicated in the figures 1.1 and 2.11 by lines of +-marks. The cross sections are located at 146° E and 75° W. The transports $\Delta\Psi$ across the cross sections and the estimate of these transports by (2.13) are compared in table 2.3 and figure 2.9; while figure 2.10 shows a scatter plot of (2.11). Several results are worth to be noted: a.) The transport across the section at Tasmania is 10 to 30 Sv stronger than the transport through the Drake Passage. b.) The inclusion of a southern restoring zone enhances the transport by about 20 Sv. c.) The transport across the sections decreases with increasing isopycnal thickness diffusion. And most important for our discussion: d.) The observed transports $\Delta\Psi$ and the reconstruction of these transports by (2.13) agree within a range of about 10%. Thus the relation (2.11) proved to be a useful diagnostic within the Southern Ocean for realistic topographies as well. This is also supported by the scatter plot shown in figure 2.10.

2.2.6 Observations and results of inverse models

The two cross sections above were subject of intense observational studies during the International Southern Ocean Studies (ISOS) experiment in the 1970s and early 1980s and the World Ocean Circulation Experiment (WOCE) in the 1990s. Here the results of subsection 2.2.3 are compared with observational estimates. In particular it is examined, whether the proposed smallness of the contribution of the deep transport to the total transport across these two cross sections is consistent with observations.

In the ISOS experiment shipboard hydrographic sections, data from moored hydrographic instruments, pressure gauges, and current meters were combined to estimate the mean volume transport through the Drake Passage (Nowlin & Whitworth (1977), Whitworth et al. (1982), Whitworth (1983), and Whitworth & Peterson (1985); for reviews see Nowlin & Klinck (1986) and Rintoul et al. (2001)). The agreement of the geostrophic shear derived from hydrographic sections with the vertical shear taken from direct current meter measurements was verified in Nowlin & Whitworth (1977) and Whitworth et al. (1982) for an appropriate time average of several days. A considerable variability in the Drake Passage throughflow ranging from 98 to 154 Sv was observed, and the mean volume transport was estimated to be 134 ± 13 Sv (Whitworth (1983) and revised estimates in Whitworth & Peterson (1985)), where the estimates for the mean transport above the reference level of 2500 m, above and relative to the reference level, below the reference level, and below and relative to the reference level are 125, 87, 9.1, and -6.7 Sv, respectively. Thus 70% of the transport above 2500 m is found in the baroclinic shear (above and relative to 2500 m). In the context of this chapter, the transport relative to the bottom layer is more relevant than the transport relative to the 2500 m level, but Whitworth (1983) and Whitworth & Peterson (1985) did not provide values for this transport. However, since part of the flow at 2500 m is already a baroclinic flow relative to the bottom layer, one would expect the contribution of the transport relative to the bottom layer to the total transport to be somewhat greater than the comparison on the basis of the 2500 m reference level suggests.

The WOCE hydrographic repeat section SR3 is very similar to the cross section between Tasmania and Antarctica considered in the global model above. Rintoul & Bullister (1999) and Rintoul & Sokolov (2001) estimated the geostrophic transport across this section relative to the deepest common depth at each hydrographic station pair, and obtained transport values between 146 and 181 Sv. In addition, Rintoul & Bullister (1999) and Rintoul & Sokolov (2001) provided estimates for the geostrophic transport relative to a deep "best guess" reference level consistent with water mass properties and float trajectories. This "best guess" reference level approximates a near-bottom reference level, except at the southern end of the hydrographic section, where the the "best guess" reference level allows for a westward flow above the upper continental slope of Antarctica. The transport relative to this "best guess" reference level ranges from 135 to 158 Sv with a mean value of 147 ± 10 Sv. With an inverse model, applying the least squares dynamically constrained optimization technique to hydrographic, wind stress, and current meter data, Yaremchuk et al. (2001) estimated the total transport across SR3 to range from 137 ± 29 to 161 ± 30 Sv with a mean of 151 ± 50 Sv. Comparing the estimates of the total transport by Yaremchuk et al. (2001) with the transport relative to the "best guess" reference level estimated by Rintoul & Sokolov (2001), the estimates agree within the limits of the error bars. The transport relative to the deepest common depth reference level, which can be considered as an approximation of the shear transport relative to the bottom (see subsection 2.2.3), tends to overestimate the total transport by around 10%.

By applying (2.13) to the Levitus (1982) data set one obtains 158.6 Sv for the Drake Passage transport and 171.8 Sv for the transport across the Tasmania cross section. These estimates lie about 18% above the estimate by Whitworth (1983) and Whitworth & Peterson (1985) for the Drake Passage transport, and 14% above the estimate by Yaremchuk et al. (2001) for the transport across SR3. Some of these differences can be explained e.g. by the westward flow at the Antarctic continental slope, where the current is more parallel than across the geostrophic contours. Apart from this, the observations in principle confirm the assumption, that the deep transport ascribed to the bottom flow makes a negligible contribution to the total transport at the two cross sections considered. This is also consistent with the inverse box model of Macdonald (1998). Rintoul et al. (2001) questioned, whether the inverse models of Yaremchuk et al. (2001) and Macdonald (1998) can really provide conclusive arguments for a small contribution of the deep transport to the total transport, since the inverse models start with a first guess of zero bottom flow. Losch (2000) and Losch & Schröter (2001) assimilated altimeter data into the model of Yaremchuk et al. (2001), to improve the estimate of the barotropic transport across SR3. However, obtaining a total volume transport of 210 ± 27 Sv and a structure of the flow, which they argued to be inconsistent with hydrography, Losch (2000) and Losch & Schröter (2001) rejected this result and considered this as an indication, that the published errors of the EGM96 geoid model could be too small. To conclude this subsection: the assumption of a small contribution of the deep transport to the total transport through the Drake Passage and across the SR3 section, for which some dynamical arguments were provided in subsection 2.2.3, can be considered to be consistent with the observations currently available.

2.3 Determining the density distribution

So far, only the dynamic balance has been considered, and the approximate balances (2.2), (2.11) and (2.12) were suggested. According to these approximate balances, the circumpolar channel transport is to leading order determined by the density field summarized in χ. A direct influence of the wind stress field $\vec{\tau}$ on the transport is not seen in (2.2), (2.11) or (2.12). The wind stress does not affect the circumpolar transport through a vertical frictional flux of zonal momentum. However, the wind may influence the circumpolar transport in a more indirect way through its effect on the density field. Such effects were investigated e.g. by Cai & Baines (1996) and Gnanadesikan & Hallberg (2000) and are addressed in this section.

2.3.1 A periodically connected rectangular basin

To study the effects of wind forcing on the density field, a further idealized numerical model was used (figure 2.12). The chosen geometry is similar to the one used by Gill & Bryan (1971), but is restricted to the latitudes south of 35°S with solid walls at the boundaries. This geometry allows Ekman pumping and water mass conversion to occur north and south of a circumpolar connection. The horizontal resolution is $2^\circ \times 2^\circ$ and the model contains 15 unequally spaced levels with a resolution varying from 30 m at the surface to 730 m at the bottom at 5700 m depth. The circumpolar connection is 3000 m deep and extends from 62°S to 42°S. Subgrid scale mixing is parameterized

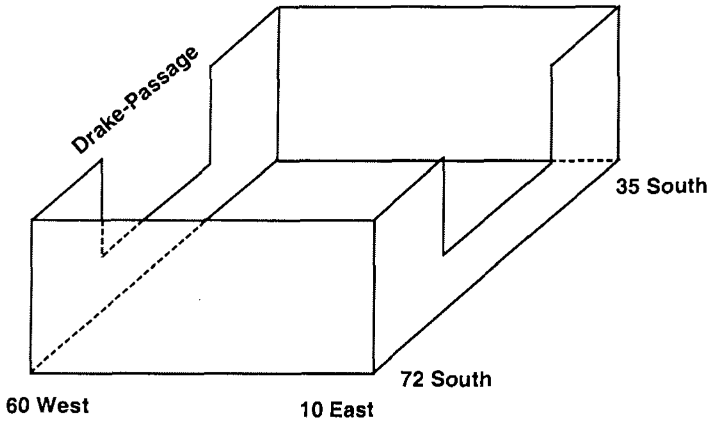

Figure 2.12: Geometry of the periodically connected rectangular basin.

with a turbulent viscosity of $2 \cdot 10^5$ m^2/s in the horizontal and 10^{-3} m^2/s in the vertical and a turbulent diffusivity of $2 \cdot 10^3$ m^2/s in the horizontal and 10^{-4} m^2/s in the vertical. Again, the distorted physics technique of Bryan (1984) was applied, to accelerate the convergence to an approximate steady state. Surface temperatures and salinities are restored to zonal mean values based on averages of Levitus (1982) and a zonally constant zonal wind stress is applied using zonal averages of Hellerman & Rosenstein (1983). In the experiments, the wind stress was varied by multiplication with a factor of -1, -1/2, 0, 1/2 or 1. The model was restored to different sea surface temperatures and salinities, and the sensitivity to the parameterization of turbulent diffusion was investigated. Starting with homogeneous water masses at rest the model was integrated for 2000 years to a near steady state.

A comparison of the streamfunction Ψ with the baroclinic potential energy χ/f_0 for the experiments with positive wind stress, zero wind stress, and negative wind stress in the figures 2.13, 2.14 and 2.15 by and large confirms the balance (2.11) for the periodically connected rectangular basin. With positive wind stress, a channel transport of 189 Sv is obtained, while the potential energy integral yields about 160 Sv, estimated at eastern side of the rectangular basin, or 180 estimated at its western side. The density field is characterized by a very weak stratification at high latitudes and a pronounced permanent pycnocline in middle latitudes. In the latitude band of the circumpolar connection the model produces a strong meridional density gradient in the upper 2 km of the water column. The zonally averaged transport features a pronounced southern sinking cell and a Deacon cell where around 4 Sv are carried southward below the sill depth of the passage. The Deacon cell vanishes with zero

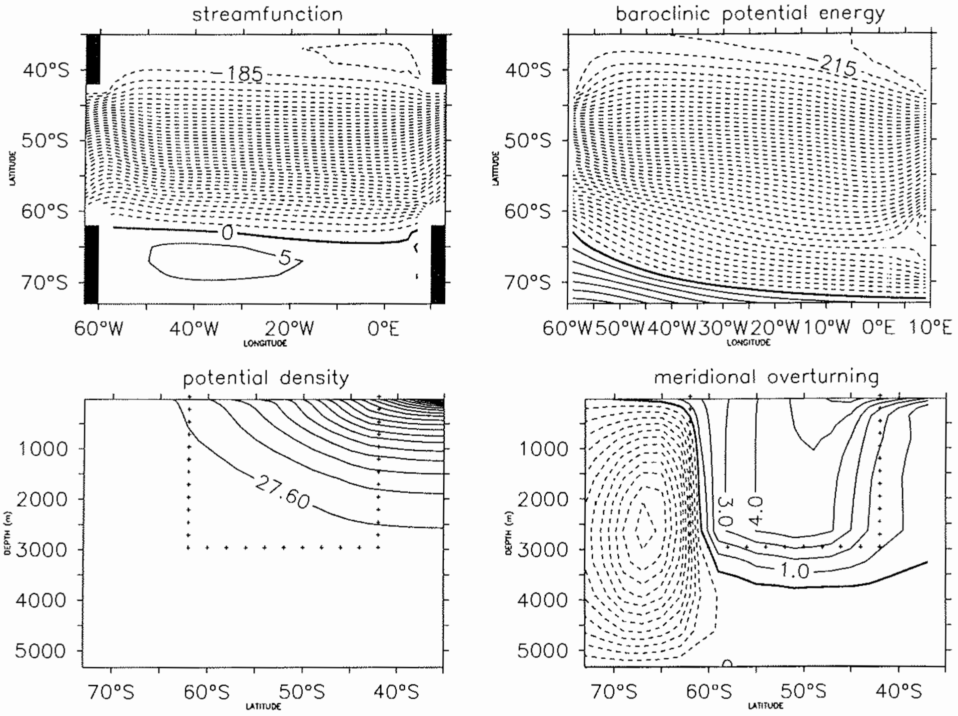

Figure 2.13: **Positive wind case:** Streamfunction Ψ in Sv, baroclinic potential energy χ/f_0 in Sv, zonally averaged potential density $\overline{\sigma}$, and meridional overturning Φ in Sv. The lines marked by crosses indicate the position of the circumpolar connection. f_0 is the Coriolis parameter at 50°S.

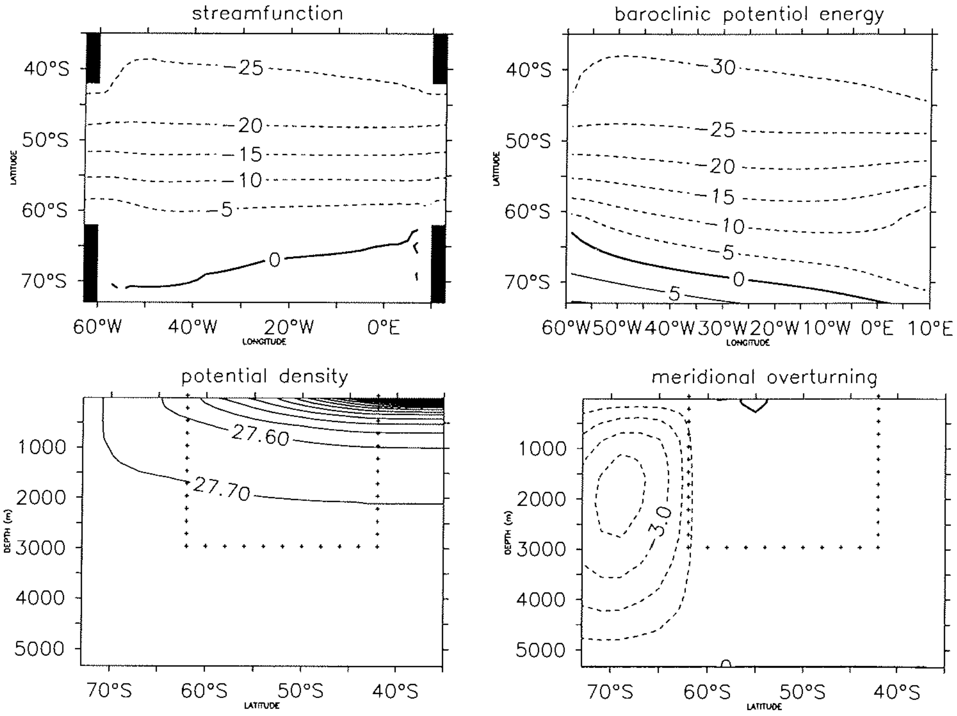

Figure 2.14: **Zero wind case:** Streamfunction Ψ in Sv, baroclinic potential energy χ/f_0 in Sv, zonally averaged potential density $\overline{\sigma}$, and meridional overturning Φ in Sv. The lines marked by crosses indicate the position of the circumpolar connection. f_0 is the Coriolis parameter at 50°S.

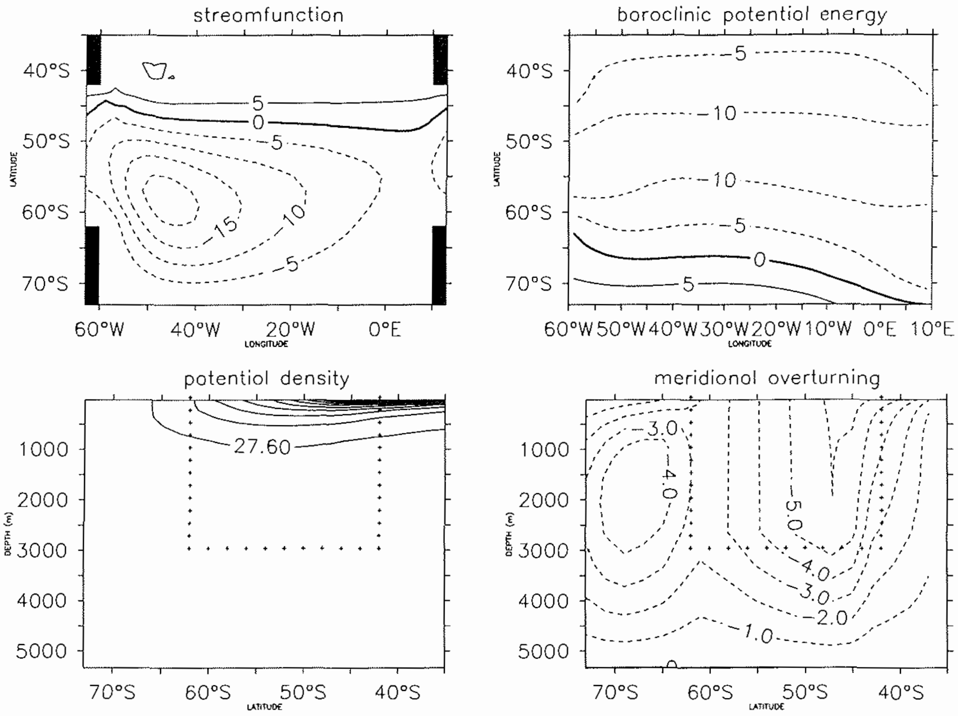

Figure 2.15: **Negative wind case:** Streamfunction Ψ in Sv, baroclinic potential energy χ/f_0 in Sv, zonally averaged potential density $\overline{\sigma}$, and meridional overturning Φ in Sv. The lines marked by crosses indicate the position of the circumpolar connection. f_0 is the Coriolis parameter at 50°S.

wind stress (figure 2.15), and the southern sinking cell is weakened. The pycnocline and the meridional density gradient are much weaker. Correspondingly, one finds a much weaker contrast in the potential energy integral, that is, again, in good agreement with the streamfunction for the vertically integrated flow.

The negative wind stress case reveals a strongly nonlinear response of the model to the wind forcing. A westward transport establishes, however, the strength is only around 10 Sv, far away from the 20 times larger response to positive wind forcing. In the interior of the rectangular basin, where the topography is flat, the fields of the streamfunctions and the baroclinic potential energy deviate significantly. While the streamfunction shows a closed gyre, as would be expected from Sverdrup theory, the contours of the baroclinic potential energy are mainly zonal. However, at the topographic barrier located at the circumpolar connection, where the geostrophic contours are blocked and the arguments of the preceding section should apply, good agreement between streamfunction and potential energy integral can be found. The reversal in the meridional gradient of the potential energy integral is related to a depression of isopycnals in the latitude band of the circumpolar connection. This depression in turn is related to the two upwelling branches of the meridional overturning circulation at around 60°S and north of 45°S. The influence of the wind forcing, the meridional overturning circulation, and the parameter values of the turbulent diffusivity on the deep stratification and on the channel transport will be discussed to some detail in following subsections.

2.3.2 Ekman transport and deep stratification

The experiments with the periodically connected rectangular basin showed a relation between the distribution of the zonally averaged potential density $\overline{\sigma}$ and the meridional overturning streamfunction Φ in addition to the close correspondence of the streamfunction Ψ and the baroclinic potential energy χ that was elaborated before.

1. Ekman convergence (divergence) north of the circumpolar connections leads to downwelling (upwelling) there. The vertical extent of this motion is reflected in a zonally integrated sense in the overturning streamfunction Φ. The northward (southward) Ekman transport connected with the eastward, i.e. positive, (westward, i.e. negative) winds in the latitudes of the circumpolar connection must be balanced by a southward (northward) return flow below the depth of the circumpolar connection of 3000 m. Thus the zonally integrated meridional overturning streamfunction Φ indicates a deep reaching downwelling (upwelling) branch north of the circumpolar connection.

2. The downwelling (upwelling) leads to a deepening (shallowing) of the pycnocline to the north of the circumpolar connection. This in turn enhances (weakens) the meridional gradient of the baroclinic potential energy χ.

3. According to our discussion of section 2.2, an enhanced (weakened) meridional gradient of the baroclinic potential energy χ must result in a stronger (weaker) channel transport $\Delta\Psi$.

In a steady state, the balance of the zonally averaged density field $\bar{\sigma}$ is written as

$$\mathcal{J}\left(\Phi, \bar{\sigma}\right) = K_v \frac{\partial^2 \bar{\sigma}}{\partial z^2} + K_h \frac{\partial^2 \bar{\sigma}}{\partial y^2} - \left(\frac{\partial \overline{v^\star \sigma^\star}}{\partial y} + \frac{\partial \overline{w^\star \sigma^\star}}{\partial z} \right) \tag{2.14}$$

where the overbar denote zonal mean, starred quantities the deviations from the zonal mean, e.g. $\sigma^\star = \sigma - \bar{\sigma}$, and subgrid mixing is simply represented by turbulent diffusion. In the experiments with the rectangular basin with circumpolar connection, it was found that the standing eddy components are irrelevant below a depth of, roughly, 500 m. Thus, in the subsequent discussion of the thermodynamic balance, these standing eddy components are omitted and we consider the proposed physical mechanism as appropriate to the model configuration used for the experiments. A more detailed discussion of the eddy induced transports will follow in section 2.3.5.

2.3.3 An idealized analytical model

The above mechanism is here summarized in a simple analytical model of the circumpolar current in the periodically connected rectangular basin. With this simple model it is attempted to reproduce the qualitative dependence of the channel transport on the thermohaline and wind forcing as well as on the parameter values of turbulent diffusion. A schematic diagram of the model is given in figure 2.16.

At high southern latitude the stratification is weak. For the present purpose, it is sufficient to assume a homogeneous density ϱ_0 south of the circumpolar connection. Below the depth of the gap, this water can geostrophically spread to the north and is supposed to fill the whole abyss of the rectangular basin. Assume that Φ has the overall structure of the Deacon cell, revealed in the experiments, with an amplitude set by the Ekman transport T_{Ek}. Then $\bar{w} \approx -T_{\mathrm{Ek}}/L_1$ in the northern downwelling branch, and one can approximate (2.14) by

$$-\frac{T_{\mathrm{Ek}}}{L_1}\frac{\partial \varrho}{\partial z} = K_v \frac{\partial^2 \varrho}{\partial z^2} + \frac{K_h}{L_2^2}\left(\varrho_0 - \varrho\right) \tag{2.15}$$

$$\Rightarrow \frac{\partial^2 \varrho}{\partial z^2} + \left(\frac{1}{L_v}\right)\frac{\partial \varrho}{\partial z} + \left(\frac{1}{L_v^\star}\right)^2 \left(\varrho_0 - \varrho\right) = 0$$

where L_1 and L_2 are horizontal length scales of the Ekman pumping and lateral turbulent diffusion, respectively, $L_v = \frac{K_v}{T_{\mathrm{Ek}}} L_1$ is a vertical Munk scale (Munk (1966)),

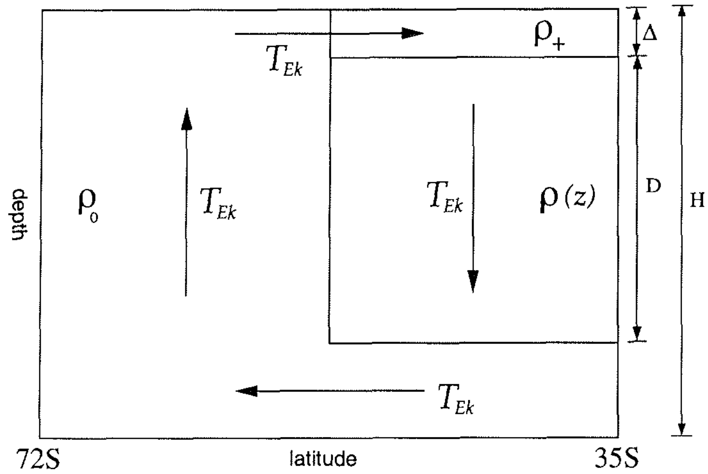

Figure 2.16: Schematic diagram of the idealized analytical model. At high southern latitudes and below the depth of the circumpolar connection (D) dense water of the density ϱ_0 is assumed. North of the circumpolar connection and advective diffusive balance for the potential density is used to obtain $\varrho(z)$ as a function of the depth z. Due to Ekman pumping north of the gap, the densities are advected vertically downwards with T_{Ek}/L_1, where L_1 is a horizontal length scale of the Ekman pumping. The surface density north of the gap is ϱ_+.

$L_v^\star = \sqrt{\frac{K_v}{K_h}} L_2$ a vertical scale of turbulent diffusion, and $\varrho(z)$ is the northern density profile. K_h and K_v are the lateral and vertical turbulent diffusivities. The horizontal diffusion is approximated by the horizontal density difference. With setting $\varrho = \varrho_+$ at the surface ($z = 0$) and $\varrho \approx \varrho_0$ in the deep ocean ($z = -D$), equation (2.15) is solved by

$$\varrho = \varrho_0 + (\varrho_+ - \varrho_0)\, e^{\frac{z}{\delta}} \tag{2.16}$$

with an inverse scale depth

$$\left(\frac{1}{\delta}\right) = \sqrt{\left(\frac{1}{L_v^\star}\right)^2 + \left(\frac{1}{2L_v}\right)^2} - \left(\frac{1}{2L_v}\right) \tag{2.17}$$

Note, since δ is small for almost all experiments, the second root of (2.17) is omitted for simplicity of discussion.

The next step is to estimate the channel-transport $\Delta\Psi$ by $\Delta\chi/f_0$. Integrating the potential energy over the depth D of the gap, a simple equation is obtained

$$\begin{aligned} \Delta\Psi &\approx \frac{1}{f_0}\left(\frac{g}{\varrho_0}\int_{-D}^{0} z\,\varrho\,\mathrm{d}z - \frac{g}{\varrho_0}\int_{-D}^{0} z\,\varrho_0\,\mathrm{d}z\right) \\ &= -\frac{g}{f_0}\frac{\varrho_0 - \varrho_+}{\varrho_0}\delta^2\left(1 - \left[1 + \frac{D}{\delta}\right] e^{-\frac{D}{\delta}}\right) \end{aligned} \tag{2.18}$$

which predicts the channel transport $\Delta\Psi$ from the wind forcing T_{Ek}, the prescribed density difference $(\varrho_0 - \varrho_+)$, and the parameters K_h, K_v, L_1 and L_2. The Ekman transport T_{Ek} and the parameters of the turbulent diffusion K_h, K_v are specified in the configurations of numerical experiments, but the choice of ϱ_0, ϱ_+, L_1, and L_2 is somewhat ambiguous. The length scale L_1 must represent the meridional extent of the downwelling (upwelling) region north of the circumpolar connection, and L_2 should approximate the horizontal length scale of the density gradient. Both may be different for the different numerical experiments. This also holds for the densities ϱ_0 and ϱ_+ of the densest and lightest water available. Within the range of reasonable parameter values, the parameters ϱ_0, ϱ_+, L_1 and L_2 were chosen to obtain a good fit of (2.18) to all numerical results (one set of parameters which is used for all experiments). The parameters used are listed in table 2.4.

The upper left panel of figure 2.17 compares the channel transport as a function of the applied wind stress, as given by (2.18), with the results obtained from the numerical experiments. The agreement of the simple model with the numerical experiment is rather good, however, concerning the quantitative agreement, some scepticism is appropriate. One noticeable qualitative difference is the slight westward transport in the numerical experiment with negative wind stress, while (2.18) implies eastward

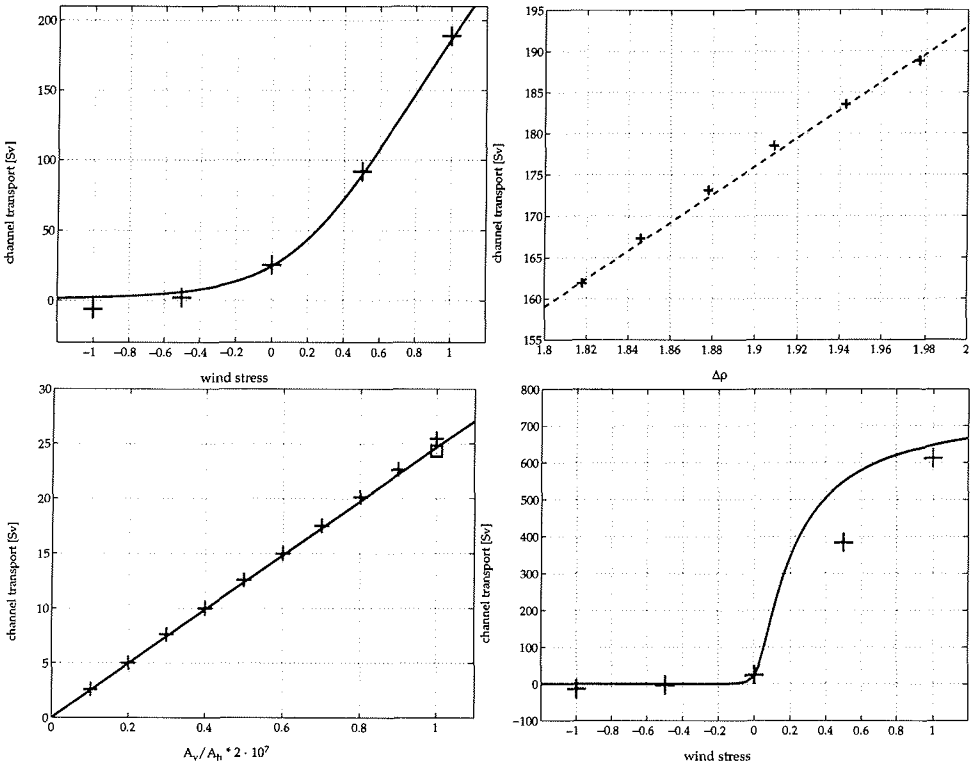

Figure 2.17: **Upper left panel:** Channel transport $\Delta\Psi$ in Sv vs. wind stress for the periodically connected rectangular basin. The crosses indicate numerical model results, the solid line the relation (2.18). **Upper right panel:** $\Delta\Psi$ vs. thermohaline surface forcing $\Delta\varrho$ in kg/m^3 for experiments with positive wind stress. The dashed line compares the numerical results with a linear relationship. **Lower left panel:** $\Delta\Psi$ vs. the ratio K_v/K_h of the vertical and lateral diffusivities in the limit of zero wind stress. The crosses represent experiments with a constant lateral diffusivity of $K_h = 2 \cdot 10^3$ m^2/s and vertical diffusivities of $K_v = (1...10) \cdot 10^{-5}$ m^2/s, the rectangle signifies an experiments with $K_v = 10^{-5}$ m^2/s and $K_h = 2 \cdot 10^2$ m^2/s, and the solid line the relation (2.18). **Lower right panel:** $\Delta\Psi$ vs. wind stress for the experiments with reduced vertical and horizontal turbulent diffusivities ($K_v = 10^{-5}$ m^2/s and $K_h = 2 \cdot 10^2$ m^2/s). All other parameters of (2.18) are taken from table 2.4.

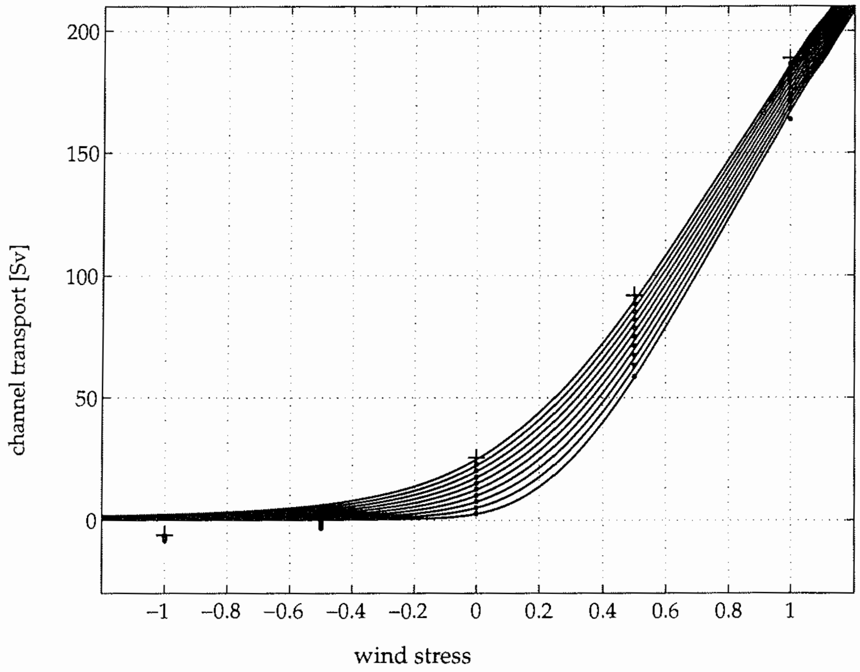

Figure 2.18: Channel transport vs. wind stress for experiments with the rectangular basin, using different vertical diffusivities K_v. The crosses indicate the numerical results for $K_v = 10 \cdot 10^{-5} \mathrm{m}^2/\mathrm{s}$, the dots the numerical results for $K_v = (1...9) \cdot 10^{-5}\ \mathrm{m}^2/\mathrm{s}$, and the solid lines relation (2.18). Beside K_v all parameters are chosen as listed in table 2.4.

$g = 9.81\ \mathrm{kgm/s^2}$
$f_0 = -1.117 \cdot 10^{-4}\ 1/\mathrm{s}$
$K_h = 2 \cdot 10^3\ \mathrm{m^2/s}$
$K_v = 10^{-4}\ \mathrm{m^2/s}$
$\varrho_0 = 1027.7\ \mathrm{kg/m^3}$
$\varrho_+ = 1025.7\ \mathrm{kg/m^3}$
$\tau^x = 0.118\ \mathrm{N/m^2}$
$D = 3000\ \mathrm{m}$
$L_1 = 1300\ \mathrm{km}$
$L_2 = 1700\ \mathrm{km}$

Table 2.4: Parameters used in (2.18).

transports for any wind stress. In the negative wind stress case of the numerical experiments, the pycnocline north of the circumpolar connection is depressed and there the meridional density gradient is reversed (see figure 2.15). Within the simple analytical model, a reversal of density gradients is impossible and thus a negative transport cannot be obtained.

The relation (2.18) implies a linear dependence of the channel transport $\Delta\Psi$ on the imposed density difference $\Delta\varrho = \varrho_0 - \varrho_+$. We conducted various experiments, changing the thermohaline forcing but keeping the other parameters constant. The upper right panel of figure 2.17 displays the results for the experiments with positive wind stress. The crosses lie almost on a straight line, but a closer look reveals a slightly concave shape.

2.3.4 The influence of diffusivity

In the limit of zero wind stress (2.18) becomes:

$$\lim_{\tau \to 0} (\Delta\Psi) \approx -\frac{g}{f_0} \frac{\varrho_0 - \varrho_+}{\varrho_0} \frac{K_v}{K_h} L_2^2 \qquad (2.19)$$

and implies a linear dependence of the channel transport on the ratio K_v/K_h of the vertical and lateral diffusivities. Various experiments with different diffusivities K_v and K_h were conducted. The results of experiments with zero wind stress are displayed in the lower left panel of figure 2.17. Consistent with (2.19) the numerical experiments show a linear relationship between $\Delta\Psi$ and K_v/K_h. The results of the numerical experiments, varying the wind stress as well as the vertical diffusivity, are shown in figure 2.18 and compared with the estimates by (2.18). The qualitative behavior of the numerical experiments is again well reproduced by (2.18). The channel transport $\Delta\Psi$ increases with an increased vertical diffusivity K_v, and the wind induced additional transport decreases with an increase in K_v. Running the model with both, the vertical and the lateral diffusivity reduced by a factor 10 (see lower right panel of figure 2.17), the channel transport shows signs of beginning to saturate with increasing wind stress. This feature is also reproduced by (2.18). This effect can be explained as follows: If the water column north of the gap is already filled (from the surface down to the depth of the gap) by light water of the potential density ϱ_+, a further increase in the wind stress cannot increase the meridional density gradient. Thus it cannot increase the channel transport either. However, in addition, it may be noted, that in these circumstances δ can no longer be considered small, and thus, without using the second root of (2.17) as well, (2.18) is a poor fit to the model results.

In their global coarse resolution model Cai & Baines (1996) investigated the effects of increasing the vertical diffusivity by a factor of 5. Without wind stress, they observed an ACC transport increased by a factor of 3.25. Equation (2.19) would suggest an increase of the ACC transport by a factor of 5, but the qualitative tendency is the same. The additional ACC transport due to the wind forcing decreased by 21.8% in the Cai & Baines (1996) experiments, which is also consistent with our findings displayed in the lower right panel of figure 2.17. The principle dependence of the ACC transport on the vertical diffusivity, as proposed by the idealized analytical model, can be further compared with the model results of Toggweiler & Samuels (1998), which are also consistent with the findings of this chapter.

2.3.5 Discussion of the meridional circulation

In this subsection some effects that were neglected in the preceding subsections are discussed, i.e. the effects of standing eddies on the so called Deacon Cell as discussed by Döös & Webb (1994), the possible coupling of the Southern Hemisphere winds with the North Atlantic Deep Water formation as proposed by Toggweiler & Samuels (1995), and the rôle of the North Atlantic Deep Water on the ACC transport as found e.g. in Goodman (1998).

By considering the changes in the density field due to changes of the wind driven Deacon Cell, and by discussing the change of the Drake Passage transport due to a changed density field, an indirect effect of the Southern Ocean winds on the Antarctic Circumpolar Current was described. As a simplification, a large scale deep downward tracer advection just north of Drake Passage was assumed to be connected with the zonally averaged overturning circulation of the Deacon Cell, and a balance of the large scale tracer advection and the turbulent tracer diffusion was stated. In the subsections 2.3.3 and 2.3.4 a satisfactory representation of the zonal transport was obtained with these simplifying assumptions.

Such a view of the Deacon Cell, as a tracer advecting meridional cell, is criticized by Döös & Webb (1994). They analyzed the Fine Resolution Antarctic Model (FRAM) and compared the meridional transport, zonally averaged along levels of constant depth, with the meridional transport, zonally averaged along surfaces of constant potential density. While the Deacon Cell was clearly reproduced with the first procedure of zonal averaging, the Deacon Cell almost completely disappeared by zonal averaging along surfaces of constant potential density. Döös & Webb (1994) concluded, that there is no diapycnic tracer transport connected with the Deacon Cell. This is contrary to the simplifying assumption used in subsection 2.3.2 and 2.3.3.

However, by comparing the zonal mean and the standing eddy components of the zonally averaged advection operator in subsection 2.3.2, a deep downwelling of tracers was found to be connected with the large scale Ekman convergence in the northern part of the Deacon Cell. Thus the simple advective-diffusive balance does apply to the coarse resolution model with the specified geometry. A Deacon Cell with a deep downwelling northern branch is also present in many other coarse resolution models, and, though it may be an unrealistic feature, it seems to be at least a feature of coarse resolution models.

Danabasoglu & McWilliams (1995) investigated the effects of the Gent & McWilliams (1990) / Gent et al. (1995) parameterization in a coarse resolution global domain model. Beside other important effects, they observed that the Deacon Cell is eliminated as a tracer transport agent, and they recommended to use the Gent & McWilliams (1990) parameterization in coarse resolution global ocean models. In the Gent & McWilliams (1990) parameterization the Eulerian mean transport velocity of the advection operator is replaced by an effective transport velocity, which is the sum of the Eulerian mean and an eddy induced transport velocity. In Danabasoglu & McWilliams (1995) the Deacon Cell is present in the Eulerian mean transport velocity, but is compensated by the additional eddy induced tracer advection, and vanishes in the effective transport velocity. The eddy induced vertical tracer transport velocity of Gent & McWilliams (1990) / Gent et al. (1995) is parameterized using the curvature of the isopycnals, and effectively restores the isopycnals towards plane and uncurved surfaces. While, within the northern branch of the Deacon Cell, the Eulerian mean transport velocity tends to displace the isopycnals downwards, the eddy induced transport velocity tends to restore the isopycnals back; and in the state investigated by Danabasoglu & McWilliams (1995) both velocities do balance each other.

Instead of using the advective-diffusive balance of subsection 2.3.3, one could use the Gent & McWilliams (1990) / Gent et al. (1995) parameterization and state a balance of the Eulerian mean and the eddy induced transport velocity. Though the physical description of the small scale details is rather different, the broad large scale consequences would be very similar. The indirect effect of the Southern Ocean winds on the Drake Passage transport through a change of the density field can be reproduced with the Gent & McWilliams (1990) / Gent et al. (1995) parameterization. The numerical experiments of Gent et al. (2001) support this view.

However, since the Gent & McWilliams (1990) parameterization only accounts for the transient / small scale eddies and not the large scale / standing eddies, the point made by Döös & Webb (1994) remains relevant. A thorough analysis of the meridional circulation in terms of Eulerian circulation, transient eddy, standing eddy, and residual circulation can be found in Olbers & Ivchenko (2001), where the formalism of the Transformed Eulerian Mean (TEM) is applied to the eddy resolving global ocean model POP (Parallel Ocean Program, Smith et al. (1992) and Maltrud et al. (1998)). The standing eddies generate an intensive cell in the Southern Ocean of POP that is concentrated in the upper 600 m. A narrow, fairly deep reaching circulation in the Drake Passage belt is induced by the transient eddies. Thus, while in the upper ocean the standing eddy contribution dominates the circulation, the deeper parts of the Deacon Cell are compensated by a circulation induced by transient eddies. Thus, in the deep ocean the Gent & McWilliams (1990) parameterization may be considered as an appropriate representation of eddy effects, and there the elimination of the Deacon cell with the Gent & McWilliams (1990) parameterization as observed by Danabasoglu & McWilliams (1995) is consistent with the findings of Olbers & Ivchenko (2001).

Toggweiler & Samuels (1995) proposed an alternative route for the return flow of the water masses driven northward by the Southern Ocean winds in the ACC belt. Instead of assuming deep downwelling just north of Drake Passage (as it is done in this chapter), Toggweiler & Samuels (1995) suggest a link of the Southern Ocean winds with the North Atlantic overturning circulation ("Drake Passage Effect"). Observing a dependence of the North Atlantic meridional overturning on the Southern Hemisphere winds in their model experiments, they suggest, that the water masses, pushed northward by the Ekman drift in the latitudes of Drake Passage, continue to flow northward and join the North Atlantic overturning circulation. The northward Ekman transport in the latitudes of Drake Passage is then compensated by a southward flow of North Atlantic Deep Water.

According to Toggweiler & Samuels (1995), a wind induced deep downwelling in the northern branch of the Deacon Cell should only occur, if the North Atlantic overturning is prohibited or limited in some way. In the idealized geometry of the periodically connected rectangular basin, the North Atlantic overturning is prohibited by an artificial solid wall at 35°S. Thus the "Drake Passage Effect" can a priori not be observed in the periodically connected rectangular basin, and an important effect may have been omitted.

In McDermott (1996), Goodman (1998), and Gnanadesikan & Hallberg (2000) a mechanism is revealed, through which the "Drake Passage Effect" could have an impact on the Antarctic Circumpolar Current. Gnanadesikan (1999) offers a simple predictive model for the pycnocline depth, where he assumes a balance of (i) vertical diffusion within the pycnocline, (ii) upwelling through the pycnocline in low latitudes, (iii) the conversion of light to dense water associated with the formation of North Atlantic Deep Water, (iv) Southern Ocean winds, and (v) Southern Ocean eddies. Concentrating on the processes (iii) and (iv) Gnanadesikan & Hallberg (2000) argue, that the Southern Ocean winds do have two effects on the density structure:

1. By increasing (decreasing) the Southern Ocean winds, more (less) deep water rises in the Southern Ocean, which leads to a deepening (shallowing) of the pycnocline.

2. In order to balance the increased (decreased) wind driven upwelling in the Southern Ocean, the overturning circulation in the North Atlantic must strengthen (weaken). Thus the northward heat transport is increased (decreased) and the North Atlantic Deep Water is warmed (cooled).

Both effects lead to an increased thermal wind shear across Drake Passage, and thus an increased ACC transport, when the Southern Ocean winds strengthen; and a decreased thermal wind shear and ACC transport, when the Southern Ocean winds weaken.

Rahmstorf & England (1997) critically examined the "Drake Passage Effect" by including a simple atmospheric feedback model to their OGCM. The atmospheric feedback tends to weaken the link between the Southern Ocean winds and the North Atlantic overturning circulation. Only one-third of the water mass driven northward by the Ekman drift in the ACC belt is returned through overturning in the North Atlantic. In the experiments of Rahmstorf & England (1997) two-third of these waters sink just north of Drake Passage. This implies, that the density field in the vicinity of Drake Passage is largely determined by local processes very similar to the processes assumed in this paper. Local processes influencing the density field north of Drake Passage are also realized in Gnanadesikan (1999) by the parameterization of the Southern Ocean eddies with Gent & McWilliams (1990).

Though a deep downwelling northern branch of the Deacon Cell might be a somewhat unrealistic view of the processes occurring in the ocean, the principal effects described by the analytical model of subsection 2.3.3 can be expected to be (to some extent) relevant in the real ocean as well.

2.4 Summary

Two main conclusions are put forward in this chapter.

1. In the case of a circumpolar channel with blocked geostrophic contours, the circumpolar transport is to leading order determined by the meridional gradient of the baroclinic potential energy. Balances (2.11) and (2.13) express this statement and these balances are proposed as useful diagnostics for the Southern Ocean. No direct effect of the wind stress can be found in (2.11), and it is concluded that the circumpolar current is not directly driven by wind stress.

2. Indirect effects of the Southern Ocean winds on the ACC transport, as suggested by Cai & Baines (1996), Gnanadesikan & Hallberg (2000), and Gent et al. (2001), are supported in this chapter. The wind stress has a pronounced influence on the circumpolar transport through its effects on the density field. A simplified analytical model is developed to investigate these effects. With this model it is possible to reproduce the qualitative dependence of the channel transport on the wind forcing, thermohaline forcing, and the parameters of turbulent diffusion, as observed in the numerical model runs.

   Additionally, by considering the effects of inverting the wind stress at the latitudes of the circumpolar connection, a clearly non linear dependence of the channel transport on the applied wind stress is revealed - while experiments with rather minor changes to the wind stress (e.g. McDermott (1996) and Gnanadesikan & Hallberg (2000)) suggest a nearly linear behavior.

Outside of frictional and inertial boundary layers, the transport across geostrophic contours is in an approximate balance with the JEBAR term. If, in addition, the shear transport is mostly zonal the deep transport across geostrophic contours must be much smaller than the total transport across geostrophic contours. For blocked geostrophic contours, this implies that the total transport can to leading order be attributed to the shear transport, which provides a first order estimate of the reaction of the ACC to changes in Southern Ocean hydrography. Through the effect of Ekman pumping on the density stratification this extends to the estimation of the reaction to changes in the wind stress field over the Southern Ocean.

Chapter 3

Sensitivity studies with coarse resolution channel models

3.1 Introduction

There are various processes in the ocean occurring on spatial scales finer than the resolution of ocean models. These are for example mixing and transport processes of temperature, salinity, and momentum due to turbulence and mesoscale eddies. While some models do resolve eddy processes no ocean model can resolve small scale turbulence. The processes which are not resolved by a model must be implemented through closure schemes. Such closure schemes usually contain a number of parameters whose values can not be completely determined from observations. Even worse, for reasons of numerical stability they sometimes must be set to values which lie clearly outside the range supported by observations.[1] For example, to avoid numerical instability the eddy or turbulent horizontal viscosity must be chosen in a way, that the resulting horizontal boundary layers can be resolved within the model. This usually implies far too high viscosities for coarse resolution ocean models. Therefore, one would like to know to what extent the model results depend on parameters whose values are either not known with sufficient accuracy or which are chosen for stability reasons.

As found in section 3.3 of this chapter, the flow within the zonally periodic channel

---

[1] And even more worse is the fact that many of the widely used closure schemes are physically inappropriate as a description of the effects of mesoscale eddies. One example is the traditional diffusion parametrization in which the eddy fluxes of a quantity are assumed to be always downgradient, parallel and proportional to the mean gradient of the quantity. Having its origin in ideas taken from molecular-scale motions the applicability to mesoscale dynamics is questionable. As mentioned in the footnote on page 17 the eddy fluxes of momentum may be directed upgradient in some areas while they are downgradient in other areas. Based on analysis of numerical model results Harrison (1978) concludes that the diffusion parameterization is not an appropriate description of mesoscale eddy fluxes; neither for heat, potential vorticity, nor for horizontal momentum.

with topography (see subsection 2.2.1 and 2.2.4, chapter 2) is appreciable sensitive to a variation of the horizontal eddy viscosity. The channel flow does not only change its strength but also its shape. In general, it is considered as problematic if the result of a numerical model does strongly depend on the exact choice of the parameter values (within the range where the parameter values are unclear). But, on the other hand, it can be very revealing to study the changes in the leading dynamical balances with a variation of different parameters. By studying which dynamical regimes are realized with which parameter settings, and by detecting the physical processes governing the different dynamical regimes realized in the model one can endeavor to gain a deeper physical understanding of the dynamical system.

Ideally, this should be done within the framework of the theory of dynamical systems; see Dijkstra (2000) for applications of this theory to physical oceanography. Within the theory of dynamical systems, the changes of the steady states of a dynamical system with a continuous variation of one or more control parameters are studied. Qualitative changes of the dynamical system are marked by bifurcation points where the steady states change their stability characteristics and/or their number. Such results are very valuable since they provide a broad overview of the characteristics of a dynamical system. Based on a suitable bifurcation analysis one can approach questions as whether the current state of the climate can be considered stable, or whether a shift to another steady state after some external distortion is possible. However, the application of the dynamical system theory to three dimensional ocean models is numerically very complicated. One of the very few codes that can handle such a system is BOOM/THCM which was developed in Utrecht by Dijkstra et al. (2001). But even with BOOM/THCM it turned out to be very difficult to calculate the steady states with channel geometry if one approaches very low values for the horizontal viscosity as well as the diffusivity (Dijkstra, pers. comm.).

The approach taken in this chapter is much less ambitious. The ocean model MOM 2 (see Pacanowski (1995)) was run with a set of parameter values forward in time to a near steady state. Then one parameter (here the horizontal viscosity) was changed, and the time integration was continued to a new near steady state. The details of the numerical experiment are given in the next section, and section 3.3 summarizes the results. In the subsequent analysis of section 3.4, 3.5, and 3.6 the rôles of bottom form drag, horizontal friction, and standing eddies are investigated to approach the physics behind the observed changes. Then, in the next chapter, a low order model is introduced which can be studied within the framework of dynamical system theory.

3.2 Experimental design

The objective of this chapter is a more complete analysis of the dynamics of the zonally periodic channel with topography (see chapter 2, subsection 2.2.1 and 2.2.4) with respect to parameter variations. The focus is on the cases with thermohaline and wind forcing, thus on the configurations C1a to C6a (see table 2.1 and 3.1). These configurations differ in the height and width of the meridional ridge. C2a was chosen as the standard case with which the other configurations are compared. For this configuration, experiments without wind forcing (with thermohaline forcing only) were included (i.e. configuration C2b). All configurations used in this chapter are of coarse resolution.

In the configurations C1a to C6a and C2b, the turbulent diffusivity was set to $10^{-4}\mathrm{m}^2/\mathrm{s}$ in the vertical as well as in the horizontal direction. Thus the horizontal diffusivity of these configurations is extremely low. Therefore, a configuration C2a hD was additionally analyzed. This configuration is identical to C2a, but the turbulent horizontal diffusivity was increased to $10^3\,\mathrm{m}^2/\mathrm{s}$.

For a better comparison with the low order model of chapter 4, two further configurations (sin1 and sin2) with a sinusoidal topography were added to the analysis. Again, they were forced by a zonal surface wind stress and by restoring the surface temperatures to prescribed values. The same profiles of the wind stress and restoring temperature as for C2a were used, but for sin2 the meridional gradient of the restoring temperature was doubled. Everything else in sin1 and sin2 is the same as in C2a.

The results for the channel geometry (see section 2.2, chapter 2) were finally compared with the periodically connected rectangular basin (rec B) of section 2.3, chapter 2. For rec B the same kind of analysis was performed as for the other configurations. Surprisingly, the flow in rec B is much less sensitive to a variation of the horizontal viscosity as the flow in the channel configurations above. A summary of the model configurations used in this chapter is given in table 3.1.

In MOM 2 the traditional frictional closure scheme was used, which assumes a downgradient horizontal flux of horizontal momentum proportional to its horizontal gradient. The governing parameter of this scheme is the horizontal eddy viscosity. To study the sensitivity to this parameter, the eddy viscosity was varied through a set of experiments as follows. First, the model was integrated with a high horizontal viscosity to a near steady state. In this step, the distorted physics technique of Bryan (1984) was applied and unequal time steps for tracer and momentum variables were chosen to accelerate the convergence to the near steady state. In a second step, the model was run for around two hundred years with equal time steps to get the result dynamically consistent. In a sequence of further steps, the viscosity was reduced and the model integrated to a new near steady state. The viscosities used in the experiments and the references to the model results are summarized in table 3.2.

Configuration	**Description**
C1a	see page 30 ff.
C2a	see page 30 ff. **(standard case)**
C3a	see page 30 ff.
C4a	see page 30 ff.
C5a	see page 30 ff.
C6a	see page 30 ff.
C2b	see page 30 ff. (no wind stress)
C2a hD	as C2a, but with turbulent horizontal diffusivity increased to $10^3\,\mathrm{m}^2/\mathrm{s}$
sin1	as C2a, but with sinusoidal topography, with zonal wavelength of 80°
sin2	as sin1, but with doubled surface temperature gradient
rec B	see page 46 ff., positive wind case

Table 3.1: Model configurations used in this chapter.

Config.	**Eddy viscosities used $[\mathrm{m}^2/\mathrm{s}]$**	**Results, see tables**	**and figures**
C1a	as for C2a	tab. 3.3;	fig. 3.1, 3.2
C2a	$1 \cdot 10^5$, $1 \cdot 10^4$, and $1 \cdot 10^3$	tab. 3.3, 3.4;	fig. 3.1, 3.3, 3.14, 3.15, 3.16, 3.17
C3a	as for C2a	tab. 3.3;	fig. 3.1, 3.4
C4a	as for C2a	tab. 3.3;	fig. 3.5
C5a	as for C2a	tab. 3.3;	fig. 3.6
C6a	as for C2a	tab. 3.3;	fig. 3.7
C2b	as for C2a	tab. 3.3;	fig. 3.1, 3.8
C2a hD	as for C2a	tab. 3.3;	fig. 3.1, 3.9
sin1	$10, 7, 5, 3, 2, 1 \cdot 10^4, 7, 5, 3, 2, 1 \cdot 10^3$	tab. 3.4;	fig. 3.1, 3.10, 3.14, 3.15, 3.16, 3.1
sin2	as for sin1	tab. 3.4;	fig. 3.1, 3.11, 3.14, 3.15, 3.16
rec B	$2 \cdot 10^5$, $2 \cdot 10^4$, and $2 \cdot 10^3$	tab. 3.3;	fig. 3.1, 3.12, 3.19

Table 3.2: Horizontal eddy viscosities used and references for the model results.

3.3 Exploration of the dynamical regimes

In table 3.3 the resulting channel transport for the configurations C1a to C6a, C2b, C2a hD, and rec B is shown. The channel transport of the standard configuration (C2a) decreases from 89 Sv to 52 Sv by reducing the eddy viscosity by an order of magnitude from $10^5\,\mathrm{m^2/s}$ to $10^4\,\mathrm{m^2/s}$, and by reducing it by an other order of magnitude the transport drops to 39 Sv. At first sight, this result may seem counterintuitive. If one thinks of friction as a momentum sink one would expect a stronger transport for a weaker frictional sink. But, in channel dynamics, friction is neither the only, nor the most important momentum sink. As mentioned in subsection 1.2.2 of chapter 1 most of the zonal momentum in the Southern Ocean is removed by bottom form drag. More details are discussed in the next section. A decrease in the channel transport with a reduction of the eddy viscosity can be also observed for most of the other configurations. This is straight forwards for the configurations C1a, C2a, and C4a. With the configurations C3a, C5a, C6a, and C2a hD one first observes an increase, and then a decrease of the channel transport. Only for the configuration with thermohaline forcing only (C2b) and the configuration with the rectangular basin (rec B) this clear decrease in the channel transport is not observed. In figure 3.1 the channel transport is plotted against the eddy viscosity for C1a, C2a, C3a, C2b, C2a hD, sin1, sin2, and rec B. In addition to the results mentioned so far an increase and decrease of the channel transport is also found for sin1 and sin2.

The barotropic streamfunction Ψ, the baroclinic potential energy χ (see section 2.2 of chapter 2), the potential temperature θ along a zonal cross section in the center of the channel, and the meridional overturning streamfunction Φ of the configurations studied are shown in the figures 3.2 to 3.12. The standard case (C2a, figure 3.3) shows in Ψ a transition from a more or less zonal flow for an eddy viscosity of $10^5\,\mathrm{m^2/s}$ to a strongly meandering flow for $10^4\,\mathrm{m^2/s}$, and then to a flow regime with a very weak channel transport and a strong double gyre circulation downstream of the meridional ridge for a viscosity of $10^3\,\mathrm{m^2/s}$. A comparison of the barotropic streamfunction Ψ with the baroclinic potential energy χ demonstrates that balance (2.11) of chapter 2 still is a useful diagnostic for the channel transport. However, it does not apply to the double gyre circulation over the flat bottom downstream of the meridional ridge. The meandering of the channel flow can also be seen from the zonal cross section of the potential temperature θ. Reducing the horizontal eddy viscosity, the isothermals strongly respond to the topography in a rather complicated manner. The meridional overturning streamfunction Φ shows a wind driven Ekman cell with a shallow return flow for a viscosity of $10^5\,\mathrm{m^2/s}$, and a return flow at the depth of the meridional ridge for reduced horizontal viscosities. With a viscosity of $10^3\,\mathrm{m^2/s}$ part of the zonally intergrated southward return flow occurs at depth close to the bottom.

The general features (i.e. the transition from a zonal to a meandering to a double gyre flow, the strong and complicated response of the thermohaline field to the topog-

eddy	channel transport of configuration							
viscosity	C1a	**C2a**	C3a	C4a	C5a	C6a	C2b	C2a hD	rec B
$2 \cdot 10^5$ m^2/s									189 Sv
$1 \cdot 10^5$ m^2/s	63 Sv	**89 Sv**	90 Sv	42 Sv	88 Sv	88 Sv	14 Sv	19 Sv	
$2 \cdot 10^4$ m^2/s									216 Sv
$1 \cdot 10^4$ m^2/s	47 Sv	**52 Sv**	179 Sv	26 Sv	96 Sv	127 Sv	34 Sv	21 Sv	
$2 \cdot 10^3$ m^2/s									214 Sv
$1 \cdot 10^3$ m^2/s	32 Sv	**39 Sv**	56 Sv	24 Sv	35 Sv	96 Sv	33 Sv	14 Sv	

Table 3.3: Channel transport for different configurations and viscosities.

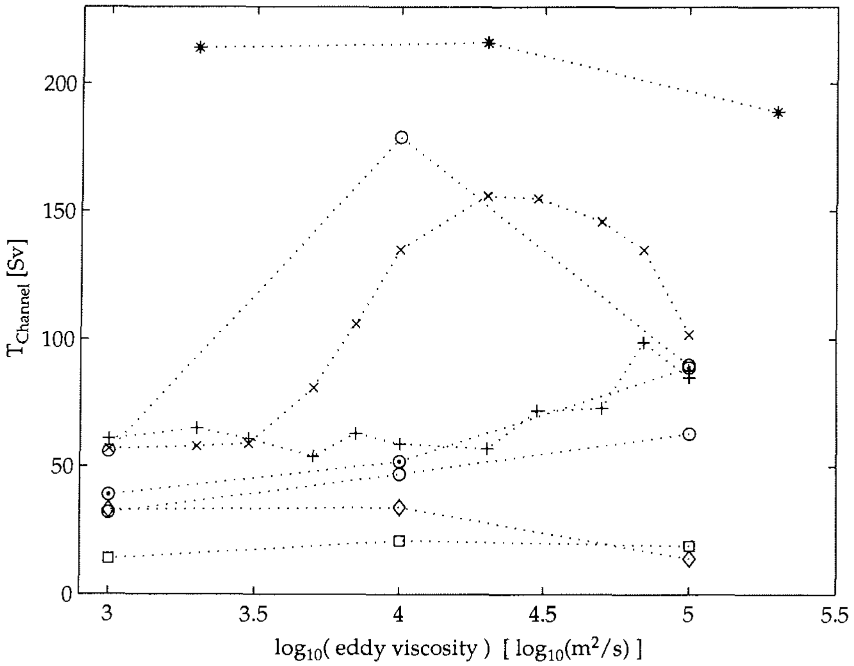

Figure 3.1: Channel Transport as a function of the horizontal eddy viscosity, taken from the numerical model results for the following configurations: [lower empty circles: C1a], [circles with dots: C2a], [upper empty circle: C3a], [diamonds: C2b], [squares: C2a hD], [pluses: sin1], [crosses: sin2], and [stars: rec B].

raphy, and the deepening of the Ekman cell) are observable in all of the configurations C1a to C6a, as well as, to a somewhat lesser degree, in C2a hD. Apart from the double gyres, the above features also show up in the configurations sin1 and sin2. In these two configurations, the bottom is nowhere flat and the double gyres are not established. For the configurations C1a to C6a and C2b the experiments were repeated with the vertical viscosity increased by one and two orders of magnitude, but in this parameter range no appreciable sensitivity to the vertical eddy viscosity was found.

If one comes to the details a lot of differences show up between the model configurations. Especially the response of the thermohaline field to the topography turns out to be very different for different configurations. The isothermal may be lifted upstream, downstream or just above the ridge. The response of the isothermal is in some cases dominated by one single broad peak and is for other cases characterized by a combination of various wavenumbers. In about half of the experiments, the slope of the isothermals responding to the ridge is clearly steeper than the slope of the ridge itself. Especially for the cases with a very flat ridge the response of the isothermals is surprisingly strong. A comparison with observations (see figure 3.13) shows that such a well pronounced response of the thermohaline field to topography indeed takes place, where, here, the isopycnals are lifted more or less downstream of the topographic features.

The configurations C2b and rec B differ in a more fundamental way. Since in C2b only a thermohaline forcing, but no wind stress is applied the wind driven Ekman cell and the double gyre circulation are not present. The meridional overturning circulation of C2b is dominated by a thermohaline driven counterclockwise circulation. For low viscosities, this circulation is confined to the depths below the meridional ridge, but for an eddy viscosity of $10^5\,\mathrm{m}^2/\mathrm{s}$ it extends to shallower depths as well. Though not always dominant, this thermohaline driven overturning circulation can also be observed in most of the other configurations.

As mentioned above, configuration rec B does not show such a strong sensitivity to the horizontal viscosity. The barotropic streamfunction Ψ is dominated by a zonal channel flow for all viscosities used. No strong meanders do develop. To the south and north of the circumpolar connection, weak counterclockwise and clockwise gyres can be found. By reducing the viscosity these gyres gain in strength. With an eddy viscosity of $2\cdot10^3\,\mathrm{m}^2/\mathrm{s}$, Ψ shows signs that the dynamical system is moving outside the numerically stable parameter range. With respect to the overturning streamfunction Φ a deep Ekman cell is present for the whole parameter range studied. With a high eddy viscosity a small portion of the Ekman flow is returned at shallower depth as well. South of the circumpolar connection, a strong thermohaline driven overturning circulation can be found, which extends northwards below the depth of the circumpolar connection. Finally, the zonal cross section of the potential temperature θ shows some response to the topography, but, here, this is much less pronounced than in the other configurations studied.

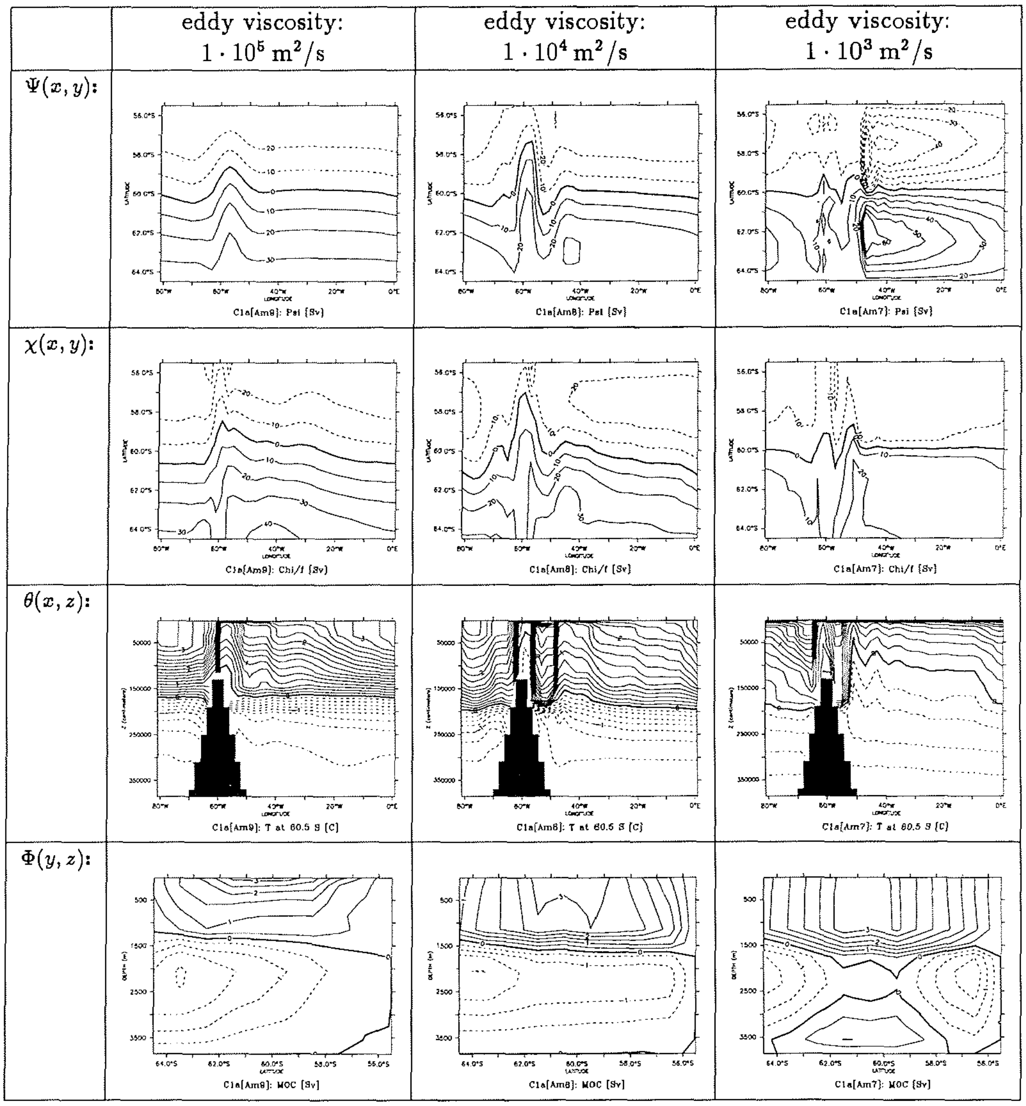

Figure 3.2: Model results of configuration C1a. The three columns show experiments with different horizontal eddy viscosities, where viscosity is decreasing from the left to the right. The top row shows the barotropic streamfunction Ψ, the second row the baroclinic potential energy χ devided by a mean Coriolis frequency f_0, the third row a zonal section of the potential temperature θ in the center of the channel, and the bottom row the meridional overturning streamfunction Φ.

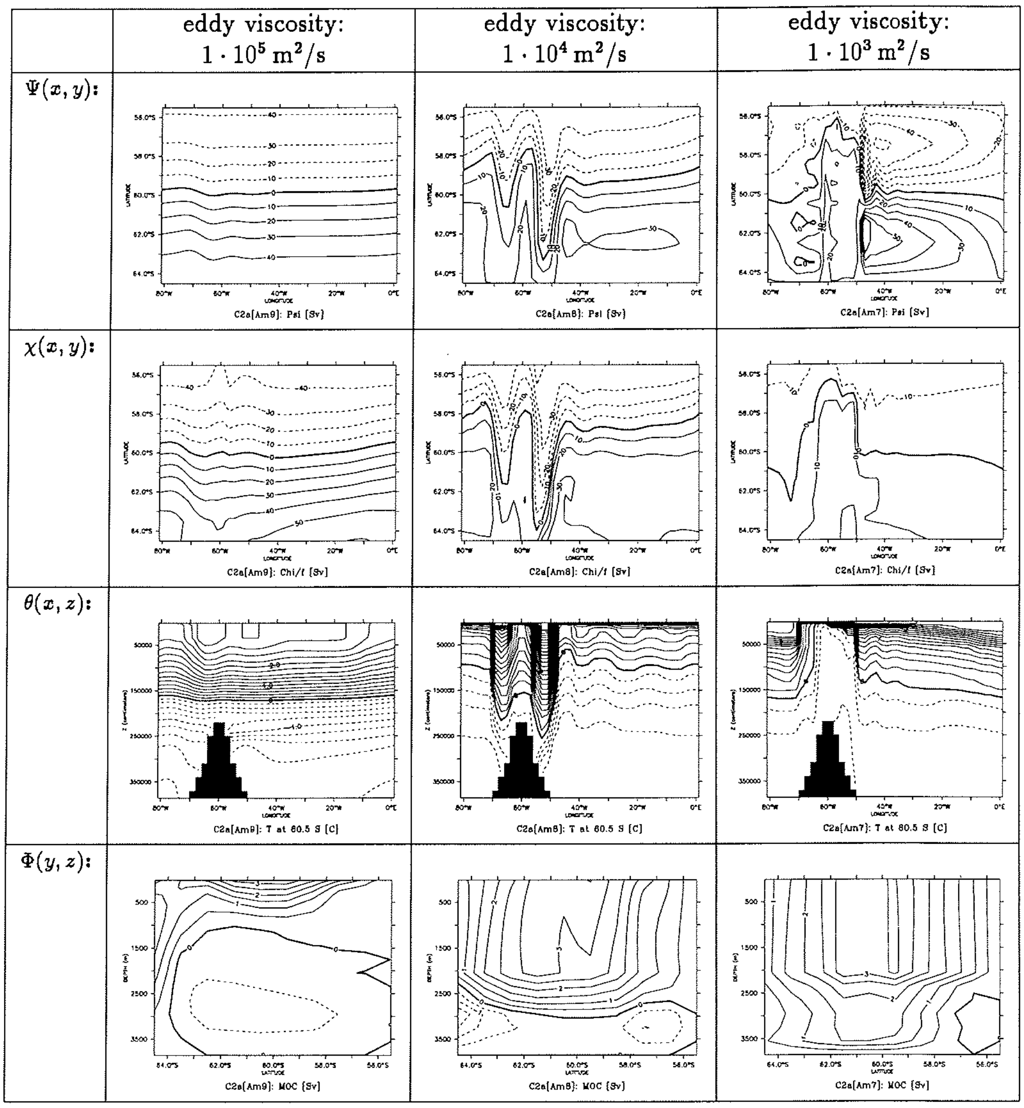

Figure 3.3: Same as figure 3.2, but for configuration C2a

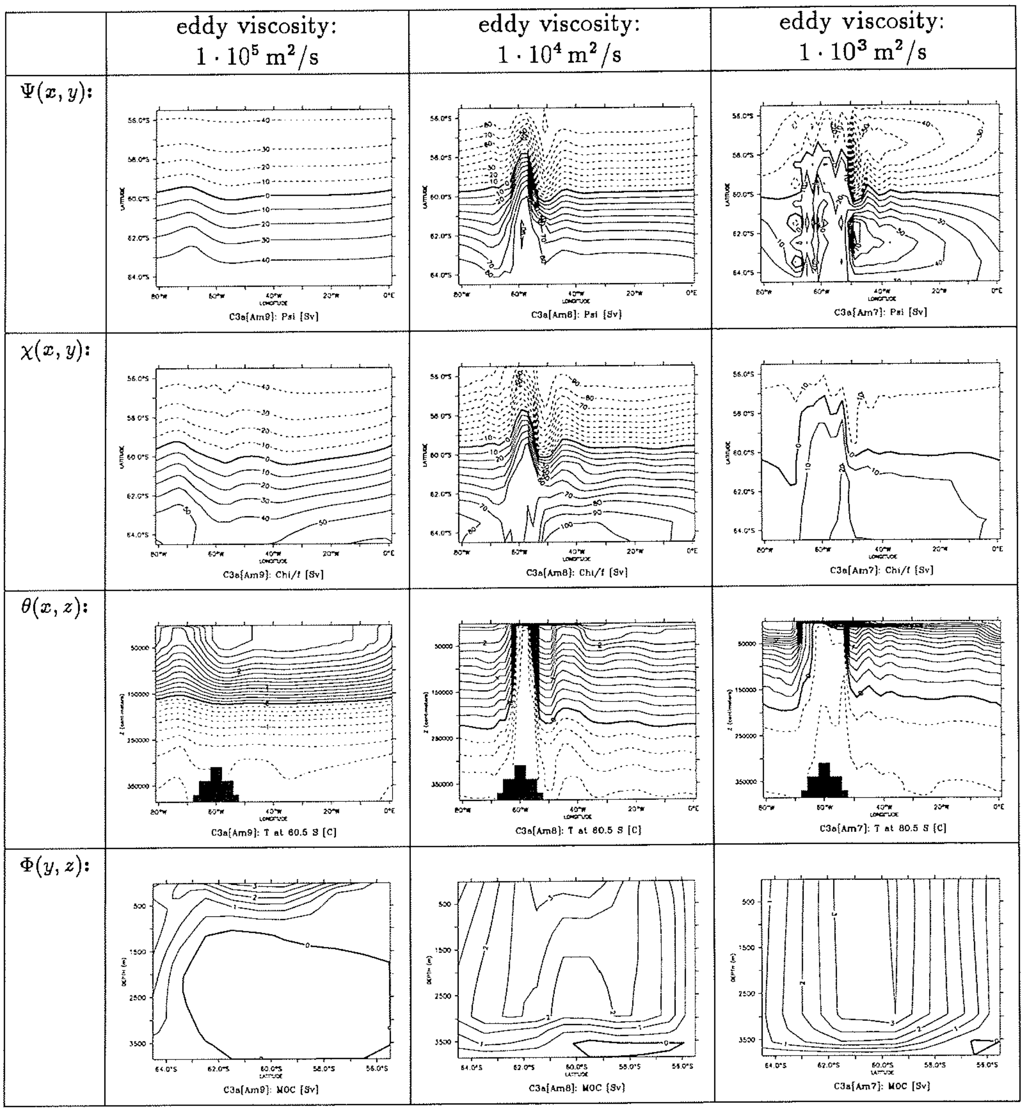

Figure 3.4: Same as figure 3.2, but for configuration C3a

	eddy viscosity: $1 \cdot 10^5\,\mathrm{m}^2/\mathrm{s}$	eddy viscosity: $1 \cdot 10^4\,\mathrm{m}^2/\mathrm{s}$	eddy viscosity: $1 \cdot 10^3\,\mathrm{m}^2/\mathrm{s}$
$\Psi(x,y)$:	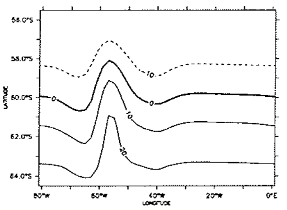 C4a[Am9]: Psi [Sv]	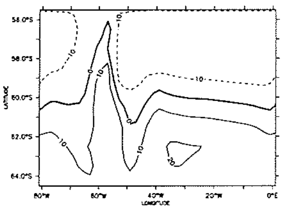 C4a[Am8]: Psi [Sv]	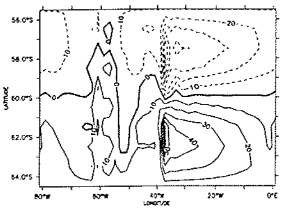 C4a[Am7]: Psi [Sv]
$\chi(x,y)$:	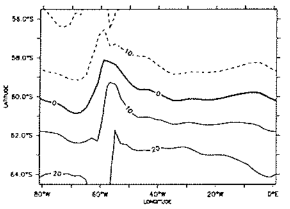 C4a[Am9]: Chi/f [Sv]	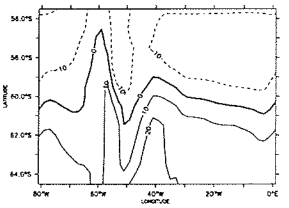 C4a[Am8]: Chi/f [Sv]	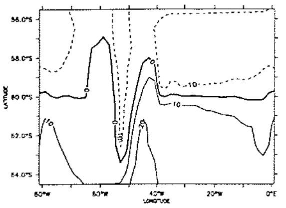 C4a[Am7]: Chi/f [Sv]
$\theta(x,z)$:	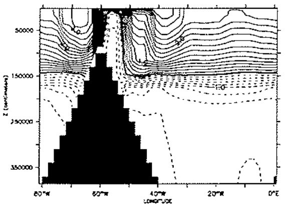 C4a[Am9]: T at 60.5 S [C]	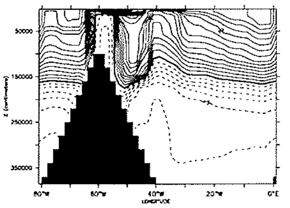 C4a[Am8]: T at 60.5 S [C]	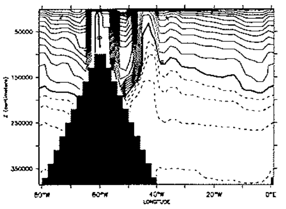 C4a[Am7]: T at 60.5 S [C]
$\Phi(y,z)$:	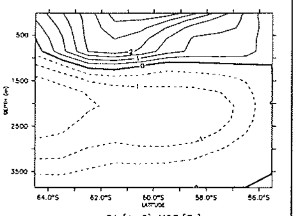 C4a[Am9]: MOC [Sv]	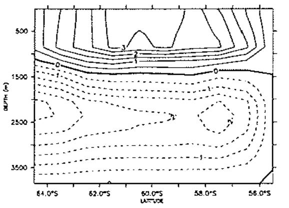 C4a[Am8]: MOC [Sv]	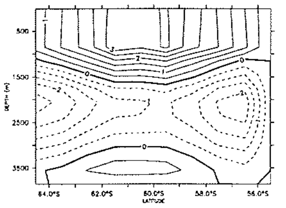 C4a[Am7]: MOC [Sv]

Figure 3.5: Same as figure 3.2, but for configuration C4a

	eddy viscosity: $1 \cdot 10^5\,\mathrm{m^2/s}$	eddy viscosity: $1 \cdot 10^4\,\mathrm{m^2/s}$	eddy viscosity: $1 \cdot 10^3\,\mathrm{m^2/s}$
$\Psi(x,y)$:	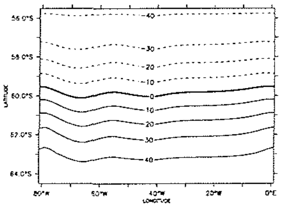 C5a[Am9]: Psi [Sv]	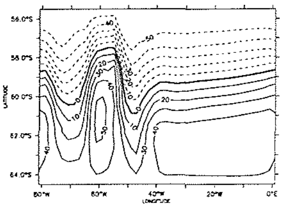 C5a[Am8]: Psi [Sv]	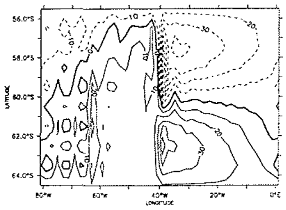 C5a[Am7]: Psi [Sv]
$\chi(x,y)$:	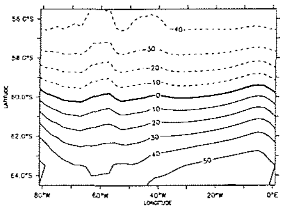 C5a[Am9]: Chi/f [Sv]	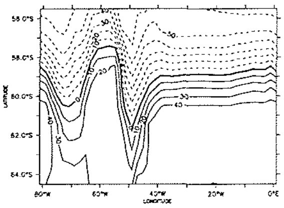 C5a[Am8]: Chi/f [Sv]	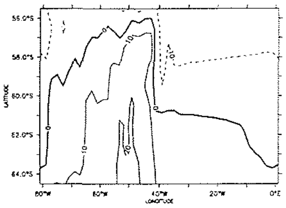 C5a[Am7]: Chi/f [Sv]
$\theta(x,z)$:	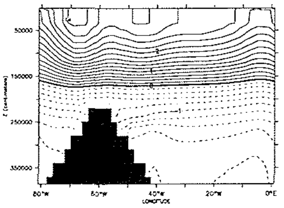 C5a[Am9]: T at 60.5 S [C]	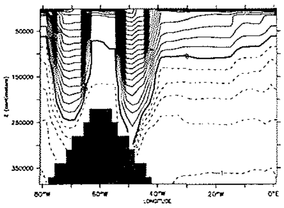 C5a[Am8]: T at 60.5 S [C]	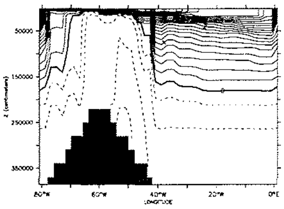 C5a[Am7]: T at 60.5 S [C]
$\Phi(y,z)$:	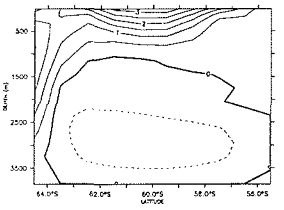 C5a[Am9]: MOC [Sv]	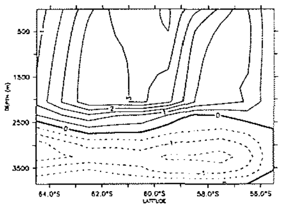 C5a[Am8]: MOC [Sv]	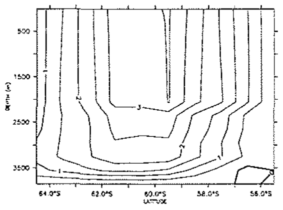 C5a[Am7]: MOC [Sv]

Figure 3.6: Same as figure 3.2, but for configuration C5a

	eddy viscosity: $1 \cdot 10^5\,\mathrm{m}^2/\mathrm{s}$	eddy viscosity: $1 \cdot 10^4\,\mathrm{m}^2/\mathrm{s}$	eddy viscosity: $1 \cdot 10^3\,\mathrm{m}^2/\mathrm{s}$
$\Psi(x,y)$:	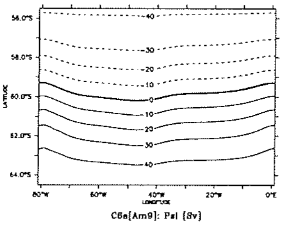	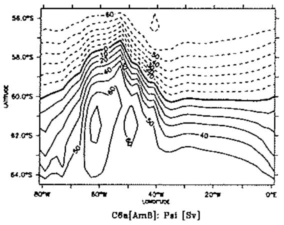	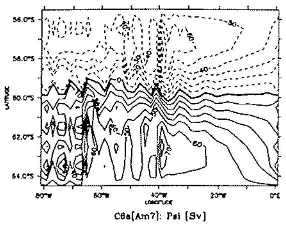
$\chi(x,y)$:	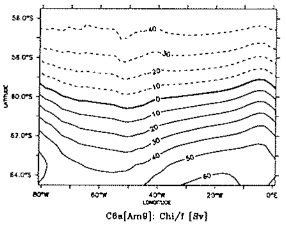	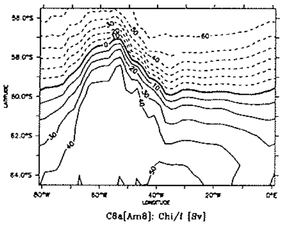	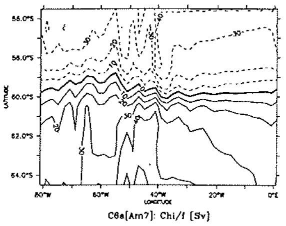
$\theta(x,z)$:	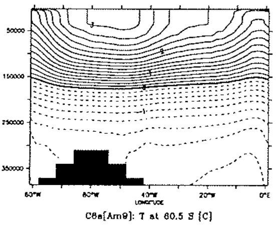	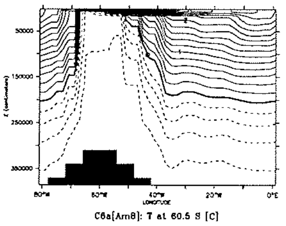	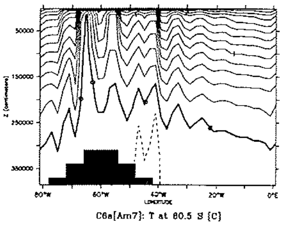
$\Phi(y,z)$:	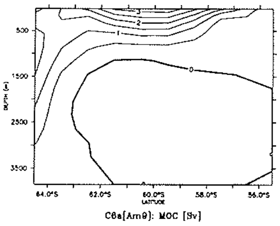	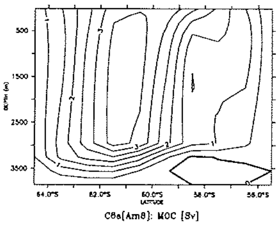	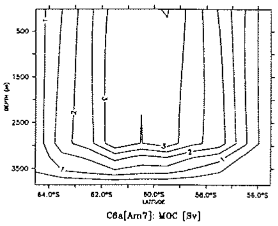

Figure 3.7: Same as figure 3.2, but for configuration C6a

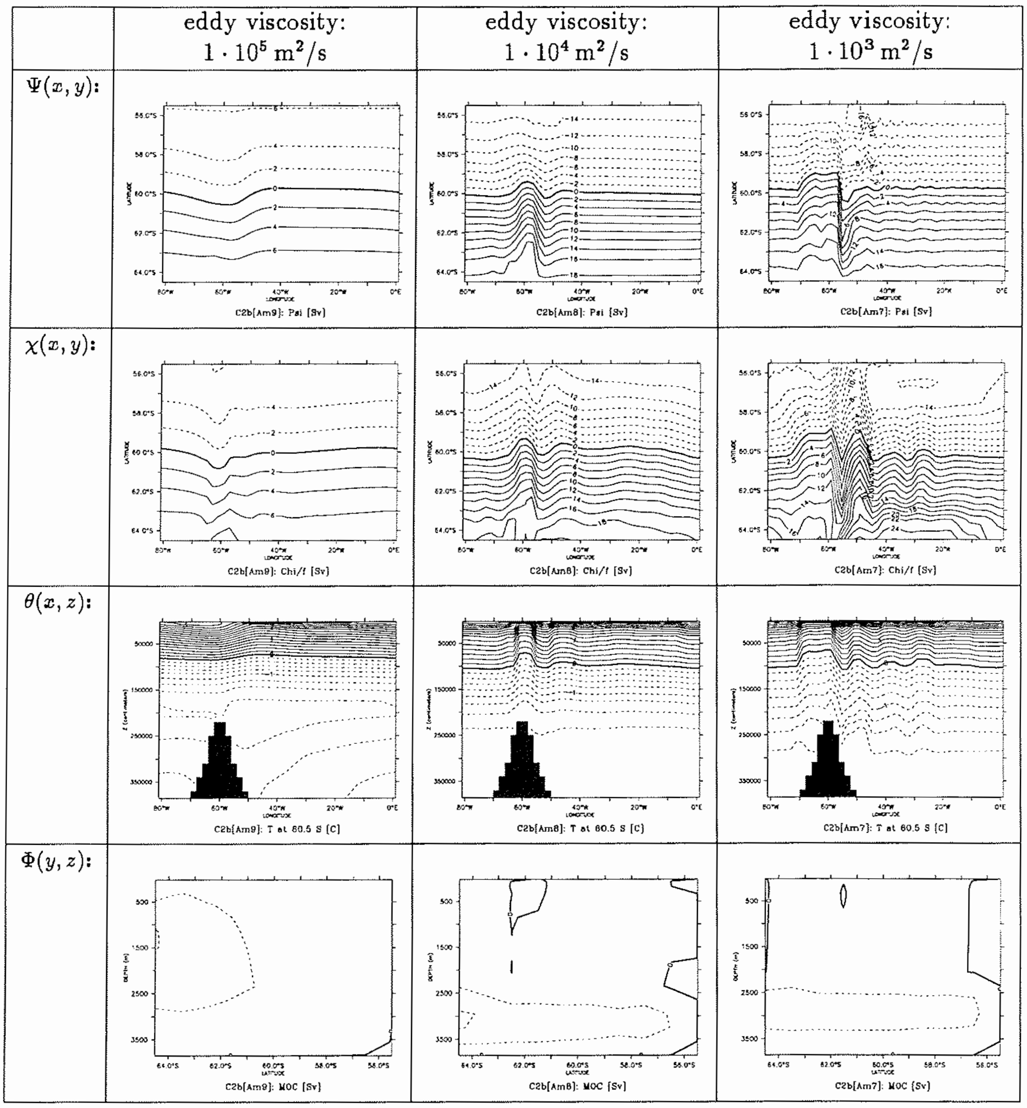

Figure 3.8: Same as figure 3.2, but for configuration C2b

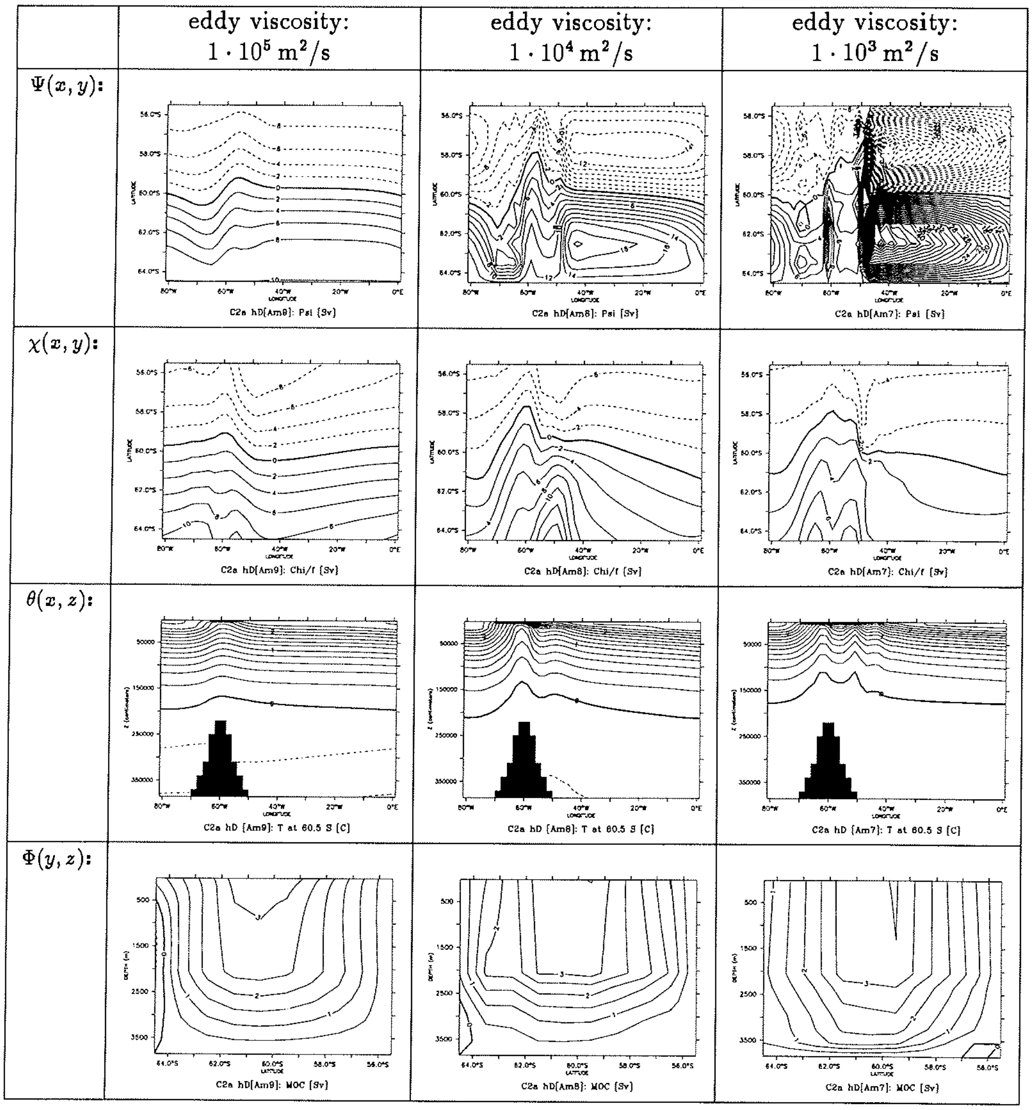

Figure 3.9: Same as figure 3.2, but for configuration C2a hD

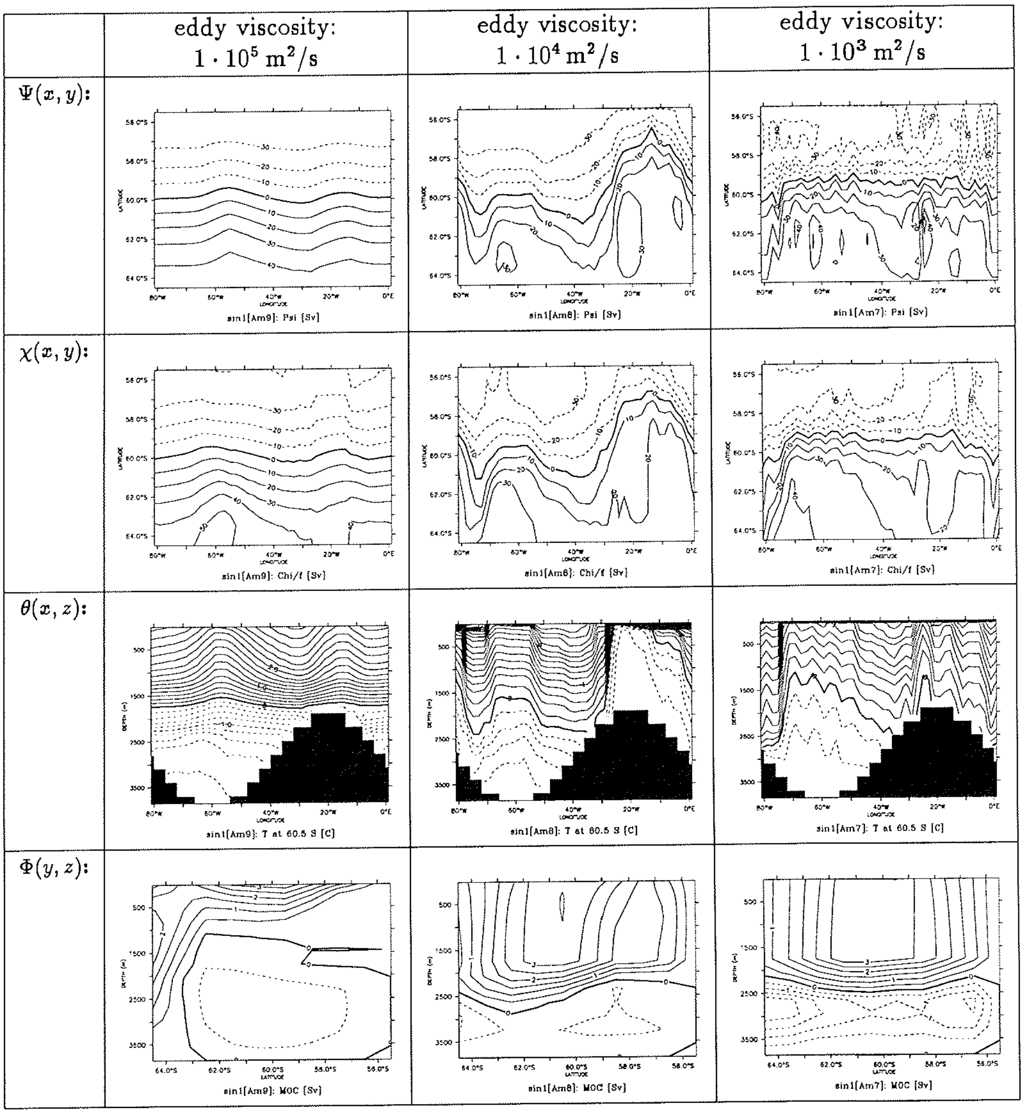

Figure 3.10: Same as figure 3.2, but for configuration sin1

	eddy viscosity: $1 \cdot 10^5\,\mathrm{m}^2/\mathrm{s}$	eddy viscosity: $1 \cdot 10^4\,\mathrm{m}^2/\mathrm{s}$	eddy viscosity: $1 \cdot 10^3\,\mathrm{m}^2/\mathrm{s}$
$\Psi(x,y)$:	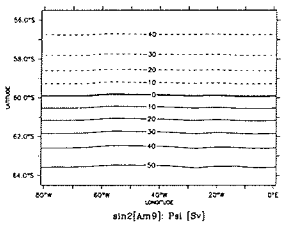	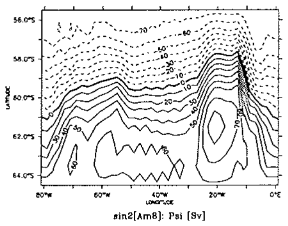	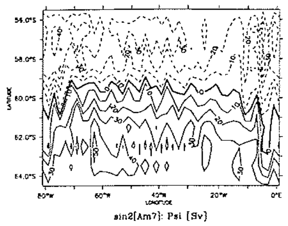
$\chi(x,y)$:	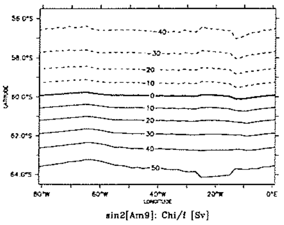	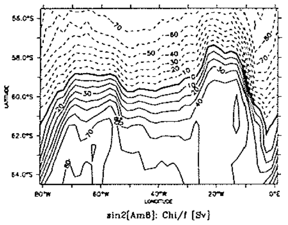	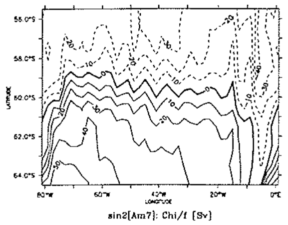
$\theta(x,z)$:	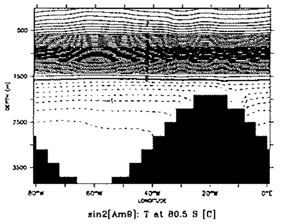	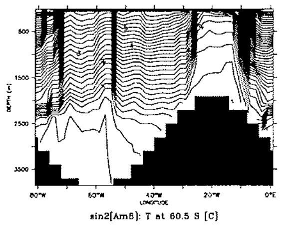	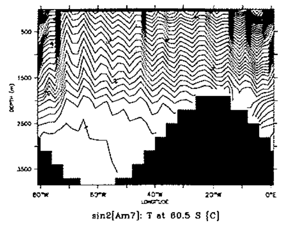
$\Phi(y,z)$:	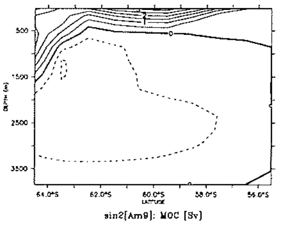	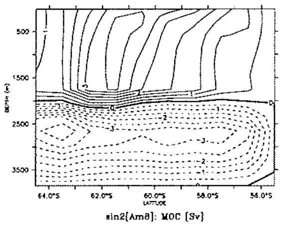	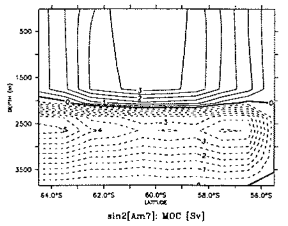

Figure 3.11: Same as figure 3.2, but for configuration sin2

	eddy viscosity: $2 \cdot 10^5\,\mathrm{m^2/s}$	eddy viscosity: $2 \cdot 10^4\,\mathrm{m^2/s}$	eddy viscosity: $2 \cdot 10^3\,\mathrm{m^2/s}$
$\Psi(x,y)$:	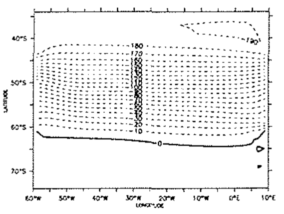 rec B [Am9]: Psi [Sv]	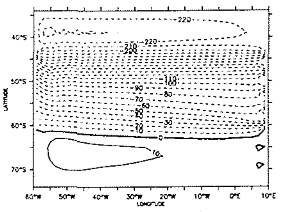 rec B [Am8]: Psi [Sv]	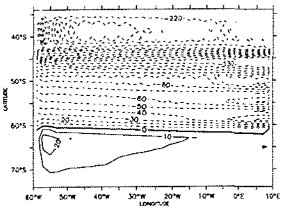 rec B [Am7]: Psi [Sv]
$\chi(x,y)$:	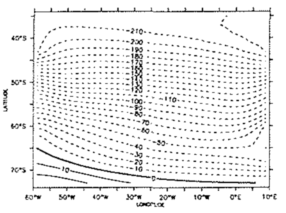 rec B [Am9]: Chi/f [Sv]	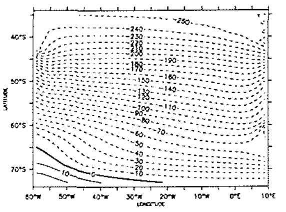 rec B [Am8]: Chi/f [Sv]	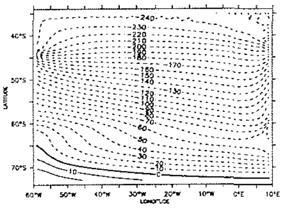 rec B [Am7]: Chi/f [Sv]
$\theta(x,z)$:	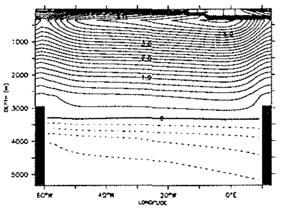 rec B [Am9]: T at 53 S [C]	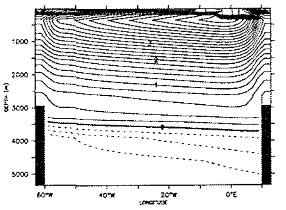 rec B [Am8]: T at 53 S [C]	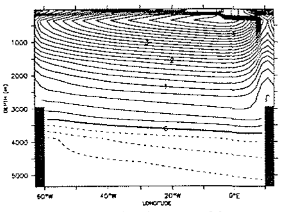 rec B [Am7]: T at 53 S [C]
$\Phi(y,z)$:	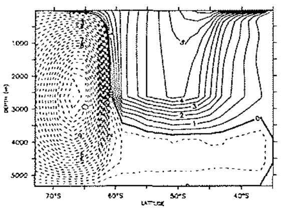 rec B [Am9]: MOC [Sv]	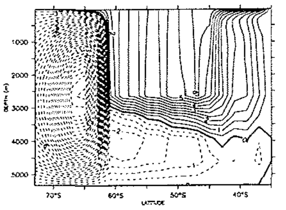 rec B [Am8]: MOC [Sv]	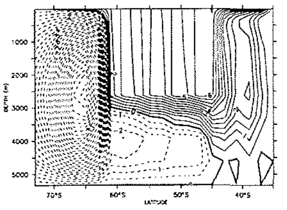 rec B [Am7]: MOC [Sv]

Figure 3.12: Same as figure 3.2, but for configuration rec B

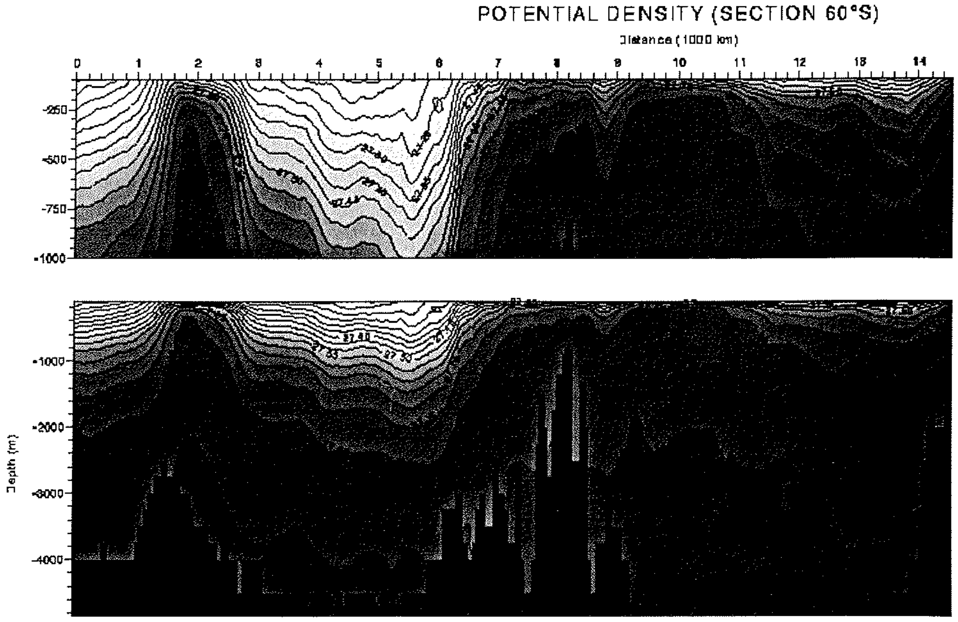

Figure 3.13: Zonal cross section of the observed potential density at 60°S, taken from the Hydrographic Atlas of the Southern Ocean, see Olbers et al. (1992a).

3.4 Balance of energy and momentum

What are the physical processes responsible for the changes in the strength and shape of the flow observed in the previous section with a reduction of the horizontal eddy viscosity? What is the difference between the zonally periodic channel with topography and the rectangular basin with a circumpolar connection, since these clear changes do not occur in the latter one? Is such a strong sensitivity of the ACC to the horizontal viscosity to be expected in global configurations of the ocean model? To obtain some ideas concerning these questions the classical analysis of the energy and momentum balances have been carried out for the configurations C2a, sin1, and sin2. The results of the analysis are summarized in table 3.4.

3.4.1 Energy

Energy is put into the system through the action of wind stress and through buoyancy forcing. For a steady state, the kinetic energy input by wind stress must be removed from the system either by friction, or by conversion into potential energy where the potential energy must be subsequently removed e.g., by diffusion. In figure 3.14 the energy taken up through conversion to potential energy is plotted against horizontal eddy viscosity. With high viscosities, only a small fraction of around 20-30% is converted into potential energy, and most of the energy is removed by friction. By reducing the viscosity the frictional energy sink becomes less efficient, and the alternative path through buoyancy forcing becomes more and more important. Finally, 70 to 85% of the energy input by wind is converted into potential energy.

3.4.2 Momentum

With respect to the momentum balance, in the steady state the eastward momentum input through the wind stress must be balanced either by friction or by bottom form drag, as summarized in subsection 1.2.2 of chapter 1. The ratio of the eastward pressure force due to bottom form drag to the momentum input by wind is plotted in figure 3.15 against the eddy viscosity. With high viscosities the bottom form drag (or more general: bottom form stress) accelerates or decelerates the eastward flow where the magnitudes are around 5 to 20% of the magnitude of the forcing by wind stress. With smaller viscosities, the bottom form stress decelerates the flow and more and more tends to balance the momentum input due to wind. On the low end of the parameter range studied, the bottom form drag even removes more than 100% of the momentum input by the wind stress (see table 3.4). The analysis of the momentum balance revealed that with very low eddy viscosities the net effect of the horizontal friction is an eastward acceleration of the flow, and the acceleration by horizontal friction plus wind stress is balanced by the bottom form drag. The streamfunction Ψ

Configuration C2a						
eddy viscosity $[m^2/s]$	channel transport [Sv]	bottom form drag			energy sink	
		barotropic [ratio]	baroclinic [ratio]	total [ratio]	buoyancy [ratio]	friction [ratio]
$1 \cdot 10^5$	89	− 0.18	0.21	0.03	0.25	0.75
$1 \cdot 10^4$	52	3.33	− 4.31	−0.98	0.49	0.51
$1 \cdot 10^3$	39	− 5.57	4.56	−1.01	0.72	0.28

Configuration sin1						
eddy viscosity $[m^2/s]$	channel transport [Sv]	bottom form drag			energy sink	
		barotropic [ratio]	baroclinic [ratio]	total [ratio]	buoyancy [ratio]	friction [ratio]
$1 \cdot 10^5$	85	− 0.71	0.65	−0.06	0.26	0.74
$7 \cdot 10^4$	99	− 1.17	0.91	−0.26	0.28	0.72
$5 \cdot 10^4$	73	− 5.40	4.83	−0.57	0.28	0.72
$3 \cdot 10^4$	72	− 4.72	4.00	−0.72	0.32	0.68
$2 \cdot 10^4$	57	−13.50	12.72	−0.78	0.37	0.63
$1 \cdot 10^4$	59	− 8.94	8.00	−0.94	0.51	0.49
$7 \cdot 10^3$	63	− 7.28	6.31	−0.97	0.57	0.43
$5 \cdot 10^3$	54	− 7.61	6.63	−0.98	0.62	0.38
$3 \cdot 10^3$	61	− 0.53	− 0.48	−1.01	0.78	0.22
$2 \cdot 10^3$	65	0.68	− 1.69	−1.01	0.82	0.18
$1 \cdot 10^3$	61	1.54	− 2.55	−1.01	0.84	0.16

Configuration sin2						
eddy viscosity $[m^2/s]$	channel transport [Sv]	bottom form drag			energy sink	
		barotropic [ratio]	baroclinic [ratio]	total [ratio]	buoyancy [ratio]	friction [ratio]
$1 \cdot 10^5$	102	− 0.07	0.26	0.19	0.22	0.78
$7 \cdot 10^4$	135	− 1.52	1.61	0.09	0.25	0.75
$5 \cdot 10^4$	146	1.00	− 1.21	−0.21	0.27	0.73
$3 \cdot 10^4$	155	4.89	− 5.46	−0.57	0.26	0.74
$2 \cdot 10^4$	156	9.73	−10.44	−0.71	0.29	0.71
$1 \cdot 10^4$	135	7.49	− 8.37	−0.88	0.43	0.57
$7 \cdot 10^3$	106	7.43	− 8.38	−0.95	0.54	0.46
$5 \cdot 10^3$	81	7.23	− 8.21	−0.98	0.63	0.37
$3 \cdot 10^3$	59	6.81	− 7.82	−1.01	0.72	0.28
$2 \cdot 10^3$	58	6.57	− 7.58	−1.01	0.78	0.22
$1 \cdot 10^3$	57	5.19	− 6.20	−1.01	0.83	0.17

Table 3.4: Channel transport, ratio of the eastward pressure force due to the barotropic, baroclinic, and total bottom form drag to the momentum input by wind (positive values represent a acceleration - negative values a deceleration of the eastward flow), and ratio of the energy taken up by buoyancy forcing and friction to the energy input by wind forcing for the model configurations C2a, sin1, and sin2 with different horizontal eddy viscosities.

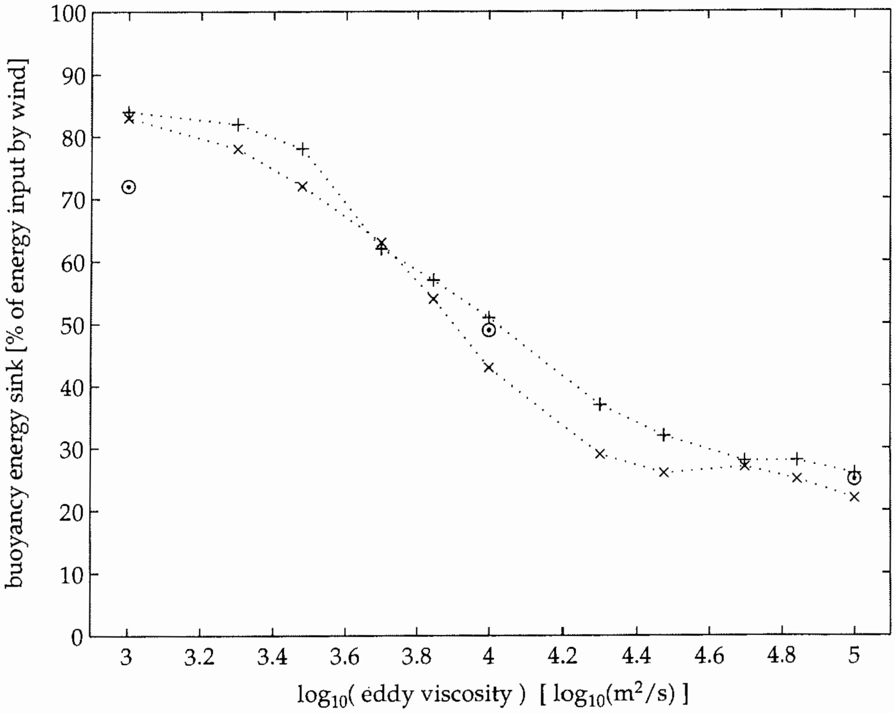

Figure 3.14: Ratio of the energy taken up by buoyancy forcing and converted into potential energy to the energy input by wind forcing as a function of the horizontal eddy viscosity for the configurations: [circles with dots: C2a], [pluses: sin1], and [crosses: sin2].

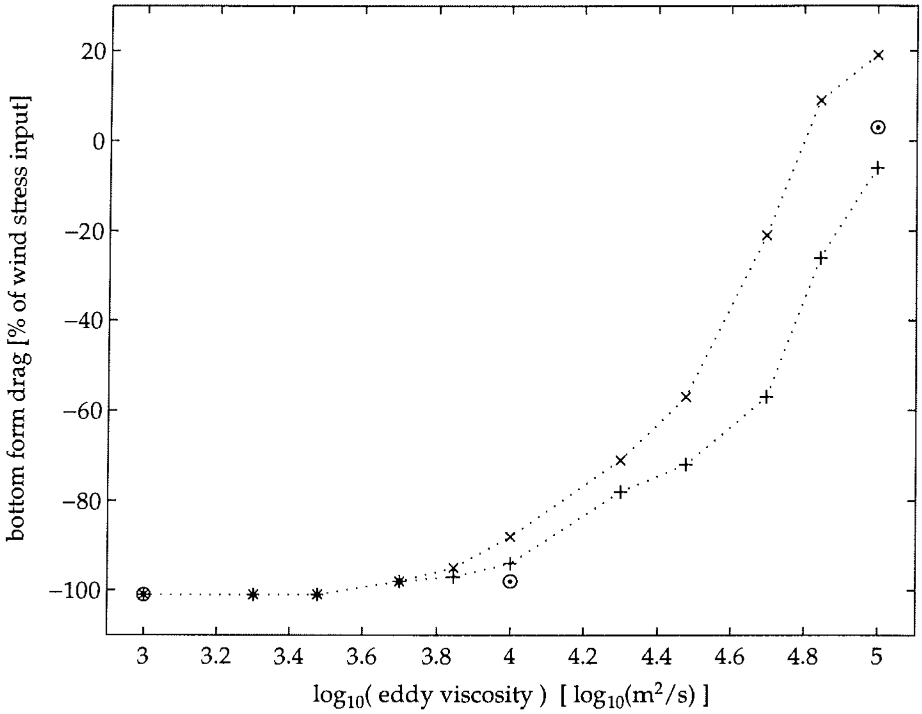

Figure 3.15: Eastward pressure force due to bottom form drag in % of the momentum input by wind as a function of the horizontal eddy viscosity for the configurations: [circles with dots: C2a], [pluses: sin1], and [crosses: sin2].

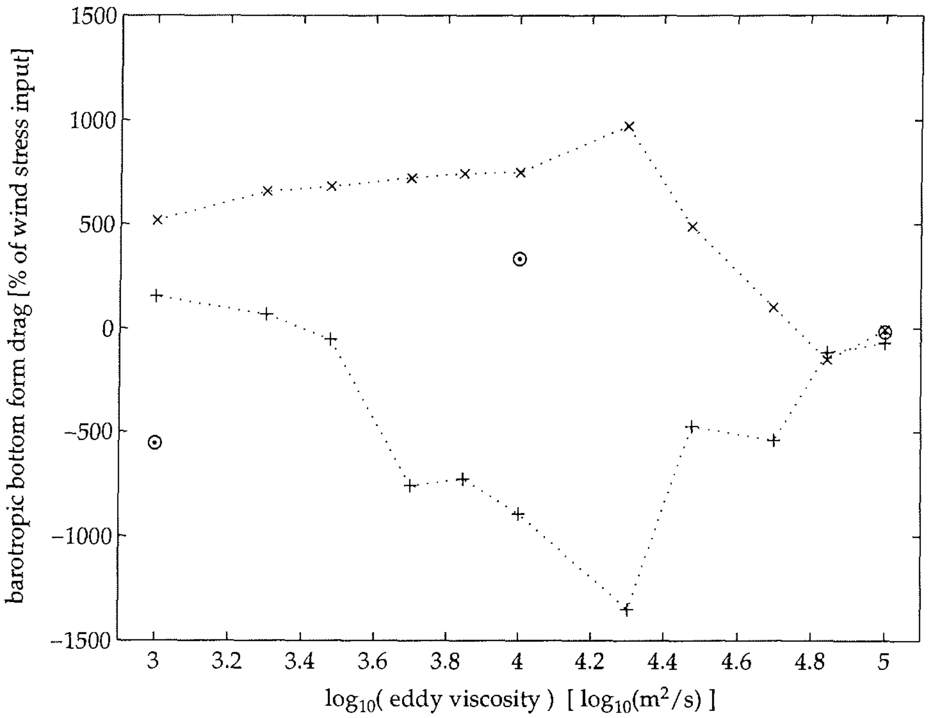

Figure 3.16: Eastward pressure force due to the barotropic component of the bottom form drag in % of the momentum input by wind as a function of the horizontal eddy viscosity for the configurations: [circles with dots: C2a], [pluses: sin1], and [crosses: sin2].

for configuration C2a with low eddy viscosity (see figure 3.3) shows a double gyre with an eastward flow in the center and a westward flow at the boundaries of the channel. Thus at the channel boundaries eastward momentum is added by lateral friction. (Similar things were observed by Treguier & McWilliams (1990) in a quasigeostrophic channel with a meridional ridge and bottom friction. In Treguier & McWilliams (1990) a westward bottom flow was present, such that the net effect of the bottom friction was an eastward acceleration of the channel flow.) A westward flow at the channel boundaries for the case of low viscosities is also present in the configurations sin1 and sin2 (see figure 3.10 and 3.11) as well as in the other configurations with wind forcing.

The bottom form drag can be decomposed into a barotropic and a baroclinic contribution (see e.g., Stevens & Ivchenko (1997)), where the barotropic part is defined as the contribution due to the surface pressure, and the baroclinic part as the contribution due to the density field. In figure 3.16 the barotropic contribution to the bottom form drag is plotted against the eddy viscosity. In most of the experiments the barotropic and baroclinic contributions to the bottom form drag are roughly one order of magnitude stronger than the bottom form drag itself (see table 3.3). The barotropic and baroclinic components almost compensate each other, where a remaining net bottom form drag is available to oppose the wind forcing. While the plots of the buoyancy energy sink and the total bottom form drag against the eddy viscosity (figures 3.14 and 3.15) are remarkable similar for different configurations, the plot of the barotropic component of the bottom form drag against the viscosity (figure 3.16) as well as the plot of the channel transport (figure 3.1) look very different for different configurations. Depending on the configuration and the eddy viscosity the barotropic component of the bottom form drag sometimes tends to accelerate and sometimes tends to decelerate the flow.

3.4.3 Comparison with the literature

Thorough analysis of the momentum and energy budgets have been carried out e.g., by McWilliams et al. (1978), Treguier & McWilliams (1990), Wolff (1990) and Wolff et al. (1991) for quasigeostrophic models with idealized channel geometry, and by Killworth & Nanneh (1994), Ivchenko et al. (1996), Stevens & Ivchenko (1997), Ivchenko et al. (1997), Best et al. (1999), and Olbers & Ivchenko (2001) for high resolution ocean models with relistic topographies. Ivchenko et al. (1997) observed for the Fine Resolution Antarctic Model (e.g., The FRAM Group (1991)) that about 75% of the kinetic energy which is input into the fluid by surface wind forcing is converted into potential energy, while Treguier (1992) found only a very small net conversion of kinetic energy into potential energy in a comparable model of the North Atlantic. Ivchenko et al. (1997) argued that these results reveal some general differences between channel type dynamics (as prevail in the Southern Ocean) and gyre type dynamics (as prevail in the North Atlantic). The conversion of kinetic into potential energy is caused by wind forced upwelling in the southern flank of the ACC, and the Southern Ocean can be considered as the main source of potential energy in the World Ocean. Ivchenko et al. (1997) suggested to use the energy analysis to discriminate between channel and gyre type dynamics, where channel dynamics is characterized by large conversion rates of kinetic into potential energy.

3.4.4 Channel and gyre type dynamics

In the light of this interpretation the flow of the configurations C2a, sin1, and sin2 would be classified as gyre type dynamics for large horizontal viscosities and as channel type dynamics for small viscosities (see figure 3.14). The examination of the momentum balance would lead to similar results. It is now generally accepted, that the input of eastward momentum to the ACC by wind stress is almost completely balanced by bottom form drag (see e.g., Ivchenko et al. (1996), Stevens & Ivchenko (1997), Best et al. (1999), and subsection 1.2.2 of chapter 1). But for the configurations C2a, sin1, and sin2 this can be only observed with small and moderate eddy viscosities (see figure 3.15). With high viscosities the wind stress is to the leading order balanced by lateral friction. Thus in these configurations the momentum balance for the experiments with high horizontal viscosities can not be characterized as being typical for ACC dynamics.

3.4.5 Coarse resolution and high viscosities

This demonstrates a problem which is well known from coarse resolution ocean models and is mentioned e.g., by Wolff et al. (1991): Ocean models with a horizontal resolution of about 5° require horizontal eddy viscosities of around $10^6\,\mathrm{m^2/s}$ in order to obtain a numerically stable solution, if the traditional frictional closure scheme is used. But with such high viscosities, the momentum input from the wind is almost completely removed by friction and no form drag is needed as an effective momentum sink. Within the experiments studied here one can observe that if the horizontal eddy viscosity is reduced the frictional sink of energy as well as of zonal momentum becomes less and less efficient. Thus other sinks are needed to balance the energy and momentum input at the surface. Therefore, the conversion of kinetic into potential energy as well as the removal of zonal momentum by bottom form drag becomes more and more important. At the same time, friction tends to damp away meanders as well as eddies, and since by reducing the viscosity this damping mechanism becomes less efficient, too, meanders and eddies can now develop.

3.4.6 Meridional overturning and zonal momentum balances

Following the discussion of Warren et al. (1996), Hughes (1997), and Olbers (1998) the close connection of the meridional circulation and the zonal momentum balance becomes evident. Here, this close connection is briefly restated. The zonal momentum balance for the steady state may be written in simplified form as:

$$-fv = -\frac{1}{\rho_0}\frac{\partial p}{\partial x} + \frac{1}{\rho_0}\frac{\partial \tau^x}{\partial z} - A_h\left(\frac{\partial^2}{\partial x^2} + \frac{\partial^2}{\partial y^2}\right)u + NL \tag{3.1}$$

where u and v are the zonal and meridional velocities of the flow, respectively, p the pressure, f the Coriolis frequency, ρ_0 a standard density, τ^x a zonal stress, A_h the horizontal eddy viscosity, and NL summarizes non linear terms. Following e.g., Olbers (1998), the water column can now be subdivided into three vertical domains.

1. The Ekman layer near the surface: To the first order the momentum balance becomes a balance of the zonal stress applied at the surface (τ_0^x) and the Coriolis term (fv):

   $$-f\left\langle \int_{-E}^{0} v \, \mathrm{d}z \right\rangle \approx \frac{1}{\rho_0}\langle \tau_0^x \rangle \tag{3.2}$$

   where the brackets $<\ >$ denote the zonal integral along latitude circles.

2. Below the Ekman layer and above the height of the topography: Away from the Ekman layer the direct influence of the surface stress disappears. In the zonal integral along an unblocked latitude, the pressure term drops out as well, and to leading order one obtains a balance of the Coriolis term and the horizontal friction:

   $$-f\langle v \rangle \approx -A_h \frac{\partial^2}{\partial y^2}\langle u \rangle \tag{3.3}$$

   In general, non linear terms are present as well. But in the coarse resolution experiments of this chapter they are not very important.

3. Depths intersected by topography: Where topography is present, a difference in the pressure of both sides of the topography can exist and a geostrophic balance in the zonal integral is possible:

   $$-f\langle v \rangle \approx -\frac{1}{\rho_0}\frac{\Delta p}{\Delta x} \tag{3.4}$$

   (For simplicity, the topography is assumed to consist only of one meridional ridge. Then $\Delta p = p_{\mathrm{west}} - p_{\mathrm{east}}$ is the difference of the pressure to the west of the ridge minus the pressure to the east of the ridge, and Δx is the zonal extension of the fluid beside the ridge. In general, balance (3.4) holds for any topography, but then Δp and Δx must be replaced by a sum over the various topographic features.)

According to this view, every term on the rhs of the zonal momentum balance (3.1) may be associated with a meridional transport.

The meridional overturning circulation observed in the numerical experiments can now be interpreted in terms of the zonal momentum balance. The shallow Ekman cell observed e.g., in configuration C2a with a horizontal eddy viscosity of $10^5\,\mathrm{m}^2/\mathrm{s}$ (see figure 3.3) points to a zonal momentum balance dominated by wind stress and friction. To obtain a balance between bottom form drag and wind stress the Ekman cell must reach down to the depth of the topography. In C2a this is the case with a viscosity of $10^4\,\mathrm{m}^2/\mathrm{s}$ or $10^3\,\mathrm{m}^2/\mathrm{s}$. In the latter case, part of the Ekman cell even goes down to the bottom, which may be associated with the double gyre circulation. The change from a zonal momentum balance dominated by friction to a balance dominated by bottom form drag can be observed in the meridional overturning circulation of all of the configurations C1a to C6a, sin1, and sin2. In C3a (figure 3.4) with a viscosity of $10^4\,\mathrm{m}^2/\mathrm{s}$ one can see one contour of the meridional overturning to close above the depth of the ridge while most of the other contours close at depth below the depth of the ridge. Thus the wind stress is mostly balanced by bottom form drag, but to a small fraction also by friction.

Without wind forcing (C2b; figure 3.8) only the thermohaline driven overturning circulation is present. Dense water is formed close to the southern boundary of the channel. Near the bottom, below the depth of the ridge, it can geostrophically spread to the north. To close the mass balance a southward return flow is needed. A geostrophic return flow is only possible below the depth of the ridge, as found for the horizontal viscosities $10^3\,\mathrm{m}^2/\mathrm{s}$ and $10^4\,\mathrm{m}^2/\mathrm{s}$. With a viscosity of $10^5\,\mathrm{m}^2/\mathrm{s}$ a frictionally balanced return flow is possible, and the thermohaline driven overturning cell extends from the bottom to depth levels close to the surface.

For the channel with high horizontal diffusivity (C2a hD; figure 3.9) and the rectangular basin with circumpolar connection (rec B; figure 3.12) the meridional overturning streamfunction Φ indicates to a first order balance between the wind stress and the bottom form drag for the whole parameter range studied. The small shallow return flow observed in Φ for small viscosities shows that part of the momentum input is also balanced by friction.

3.4.7 Periodic channel vs. circumpolar connected basin

The question now is: What makes the difference between the channel with topography and the rectangular basin with circumpolar connection? There are at least four potential candidates:

1. Diffusivity: The horizontal eddy diffusivities differed by several orders of magnitudes; it was $1 \cdot 10^{-4}\,\mathrm{m}^2/\mathrm{s}$ for C1a to C6a, C2b, sin1, and sin2, $1 \cdot 10^{3}\,\mathrm{m}^2/\mathrm{s}$ for C2a hD, and $2 \cdot 10^{3}\,\mathrm{m}^2/\mathrm{s}$ for rec B. Horizontal diffusion can at least have two effects: First, it may reduce the meridional density gradient and in accordance to (2.11) it thus would reduce the channel transport. Second, it could damp geostrophic eddies and meanders of the flow. A comparison of C2a hD (figure 3.9) with C2a (figure 3.3) shows that the channel transport is indeed substantially reduced in the configuration with high diffusion. Due to the weaker zonal flow in C2a hD less momentum is removed by friction, and a balance between the wind stress and the bottom form drag is established for all three viscosities studied. But the transition from a zonal flow to a meandering flow and then to a double gyre circulation is observable in both of the two configurations, while in the rectangular basin such kind of transition does not occur. To summarize: After increasing the horizontal diffusivity the zonal momentum balance of C2a hD looks more similar to rec B but with respect to the development of standing eddies these two configurations are still very different.

2. Thermohaline forcing: The channel configurations C1a to C6a, C2b, C2a hD, and sin1 were restored to a linear temperature profile with −2 °C at the southern channel boundary and 8 °C at the northern boundary. The salinity was kept constant at 34 psu. The rectangular basin rec B was restored to a zonally averaged climatology, where the restoring temperature varied from −2 to 18 °C and the salinity from 33.9 to 35.3 psu. Thus the imposed density contrast is much stronger in the rectangular basin. However, its meridional extent is about three times the meridional extent of the zonally periodic channel, and the imposed density gradient is not very different. Through (2.11) a stronger density contrast in the meridional direction should result in a stronger channel transport. However, the effects on the sensitivity of the flow to the horizontal eddy viscosity are less clear. To study such effects the configuration sin2 was introduced. sin2 is identical to sin1 except that the surface temperatures are now resorted to a linear profile with −2 °C in the south and 18 °C in the north. As can be seen from figure 3.1 table 3.4 the channel transport of sin2 is in general clearly stronger than that of sin1. However, this is not true for very low horizontal viscosities. The qualitative dependence of the channel transport on the viscosity is very different for the two configurations. In the case of a stronger imposed temperature gradient (sin2) the transport first starts to increase by up to $\approx 50\%$ and

then decreases with decreasing viscosity. In sin1 the channel transport decreases more or less monotonically. Concerning the balance of energy (see figure 3.14), the balance of momentum (see figure 3.15), and the development of standing eddies (see figure 3.10 and 3.11) the qualitative differences between sin1 and sin2 are not so obvious. To summarize: Increasing the imposed density gradient has substantial effects on the channel transport as well as on the sensitivity of the flow, but it is less clear whether this helps to explain the differences between the channel and the periodically connected rectangular basin.

3. Horizontal scales: From (3.1) it follows that the horizontally averaged frictional momentum sink is $\mathcal{O}\left(\left[A_h \cdot \Delta\Psi\right] / \left(\Delta y\right)^3\right)$ where A_h is the horizontal eddy viscosity, $\Delta\Psi$ the channel transport, and Δy the meridional extent of the channel or basin. Thus the zonal momentum budget can be expected to depend strongly on the horizontal scales of the channel or basin. In rec B the meridional extent is three times the extent of C2a and the frictional momentum sink of rec B is much less efficient. Thus in rec B a balance between wind stress and bottom form stress is established for all eddy viscosities studied. While in the channel configurations the balance of wind stress and bottom form drag is connected with the presence of standing eddies, this is not the case in the rectangular basin. To summarize: The difference in horizontal scale may explain the differences in the zonal momentum balance. Whether this also helps to explain the differences in the development of standing eddies remains unclear.

4. Geometry: One last obvious difference between the channel configurations (e.g., C2a) and the rectangular basin (rec B) should be mentioned: geometry. In rec B blocked latitudes are present north and south of the circumpolar connection. This allows east-west pressure differences and thus a net geostrophic meridional flow at all depth levels at these latitudes. It remains unclear what this implies for the development of standing eddies.

3.4.8 Intermediate summary

The results discussed so far may be summarized as follows:

- Channel transport: The channel transport is determined through (2.11) by the density field as put forward in chapter 2. The density field may depend in a complicated manner on the horizontal viscosity, the bottom topography, surface forcing, and other factors. This was observed for the zonal channel with topography but not for the rectangular basin with circumpolar connection. Concerning the zonal channel with topography, the drastic changes in the density field as well as in the strength and shape of the flow were associated with a qualitative change in the zonal momentum balance.

- Momentum balance: The balance between wind stress and horizontal friction shifts to a balance between wind stress and bottom form drag, by
  - reducing the horizontal eddy viscosity
  - increasing the horizontal eddy diffusivity
  - widening the channel in meridional direction[2]
- Standing eddies: While in the zonal channel with topography the momentum balance of wind stress and bottom form drag seems to be connected with standing eddies this is not the case in the rectangular basin with circumpolar connection.

3.5 The rôle of standing eddies

Eddies (standing as well as transient eddies) do have two important and intimately linked effects. First, they transfer zonal momentum downwards through the water column and then to the bottom topography (see subsection 1.2.2 of chapter 1). Second, they contribute to the meridional transport of heat, salinity, and other tracers (see e.g., De Szoeke & Levine (1981), Thompson (1993), Speer et al. (2000), Hallberg & Gnanadesikan (2001), MacCready & Rhines (2001), Tansley & Marshall (2001), Lee & Coward (2003), and Karsten & Marshall (2002)).[3] Due to the coarse resolution of the numerical models studied in this thesis, transient eddies are not sufficiently realized within the model dynamics. (However, to some extent they are represented in the closure schemes for the tracer equations.) In this section, the effects of standing eddies are discussed with respect to the coarse resolution experiments considered in this chapter.

3.5.1 Their rôle in the total balance of zonal momentum

Concerning the zonal momentum balance standing eddies may contribute to the generation of a bottom form drag but a bottom form drag may also be established without them. A bottom form drag is established by differences between the pressure east and west of a topographic obstacle. A meandering geostrophic bottom flow which is directed southwards in valleys and northwards above topographic obstacles would

---

[2] The vertical walls at the northern and southern boundary of the zonally periodic channel with topography introduce frictional boundary layer effects in a way which is unrealistic for the ACC. These unrealistic effect may be removed (or weakened) if idealized ocean basins are added to the channel so that the effective meridional extent of the channel is increased.

[3] A third important effect is the horizontal redistribution of the zonal momentum by Reynolds stress. As mentioned in the footnote on page 17 this may lead to a upgradient transport of zonal momentum and a concentration in strong jets. However, this effect is only relevant in high resolution models and may be disregarded in the discussion of the coarse resolution experiments of this chapter.

imply a bottom form drag of the right sign to balance the surface wind stress. But, assuming huge diapycnal fluxes, such a bottom form drag could also be established through deep downwelling in the north, a southward geostrophic flow below the depth of topography, and upwelling in the south - thus without standing eddies.

As discussed in 3.4.6, the pressure differences across topographic obstacles implies a net geostrophic meridional volume transport below the depth of the topography. To balance the wind stress by bottom form drag this net geostrophic transport must be equal but opposite the surface Ekman transport. From this one may expect that a meandering flow with a volume transport of the same order of magnitude as the volume transport of the Ekman flow could be sufficient. In the case of a channel with a homogeneous density field this is supported by the numerical experiments (see table 2.2 and figure 2.6 of chapter 2). But in the experiments with a baroclinic channel the volume transport of the meandering flow was about one order of magnitude stronger than that of the Ekman flow (see figures 3.2 to 3.11 of this chapter). This has its manifestation in the fact that the barotropic and baroclinic components of the bottom form drag do almost compensate each other with a resulting total bottom form drag one order of magnitude smaller than each of its components (see table 3.4, and figure 3.15 and 3.16). The flow above and relative to the bottom layer can result in a barotropic plus a baroclinic bottom form drag, compensating each other to a zero net bottom form drag. Only a small portion of the meandering flow contributes to the generation of a net bottom form drag.

A barotropic and baroclinic bottom form drag almost compensating each other to a net bottom form drag opposing the wind stress is well known e.g., from Olbers & Wübber (1991), Olbers et al. (1992b), and Stevens & Ivchenko (1997). In Stevens & Ivchenko (1997) the baroclinic component tends to accelerate the flow, and the barotropic component opposes the baroclinic component as well as the wind stress. A baroclinic bottom form stress that accelerates the eastward flow could also be inferred from hydrography (see figure 3.13) where the isopycnals are lifted above topographic obstacles but with a slight shift to the east. But in the coarse resolution experiments considered in this chapter, the isopycnals seem to respond to the topography in a more complicated way and no such simple statement concerning the phase relationship can be made (see figures 3.2 to 3.11).

3.5.2 Their rôle concerning meridional transports

With respect to the standing eddy transport, figures 3.17 to 3.19 show the zonal mean and standing eddy components of the zonally averaged meridional temperature transport relative to 0°C for C2a, sin1, and rec B. [4] The transient eddy component is more

---

[4] Here, the "temperature transport relative to 0°C" is used instead of the heat transport. Strictly speaking the last one would be the more appropriate notion. But only a small portion of the total

than three orders of magnitude smaller and is not shown. In the case of high eddy viscosities in the configuration C2a (see figure 3.17) the standing eddy component is very small and the meridional advective temperature transport is dominated by the mean component. In the northern part of the channel this transport is oriented downwards and southwards. The vertical component of the advective temperature transport is 500 times exaggerated, but one must also consider that the vertical temperature gradient is about three orders of magnitude stronger than the meridional one. Thus the effects of the vertical and the meridional transport on local temperature changes can be expected to be comparable. In the case of higher eddy viscosities both, the zonal mean and the standing eddy component are significant. The leading order effect of the zonal mean component is a downward temperature transport in the northern part of the channel which results in a deepening of the thermocline. The standing eddy component of the temperature transport by and large transports the temperature downgradient and weakens the meridional temperature gradient. Together with (2.11) of chapter 2 this implies a reduction of the channel transport due to the presence of standing eddies. Similar results can be observed in the other channel configurations with wind forcing (i.e., Cla to C6a, C2a hD, sinl, and sin2, the results for sinl are shown in figure 3.18).

The situation is considerable different in the configuration rec B (see figure 3.19). A standing eddy temperature transport with roughly the same shape and strength is present for all three eddy viscosities used. Its horizontal component is southward (downgradient) and is somewhat weaker than the horizontal component of the eddy temperature transport found in the low viscosities cases for C2a or sinl. But the vertical component of the zonal mean as well as of the standing eddy temperature transport is about two orders of magnitude stronger than in the configurations C2a and sinl. (Note that the vertical component in figure 3.19 is only 5 times exaggerated while it was 500 times exaggerated in figure 3.17 and 3.18.) Its major effect is a deepening of the thermocline in the northern part of the channel. This implies an increase of the deep meridional temperature gradient and this effect outweights the reduction of the gradient due to horizontal downgradient eddy transports. The application of the simple analytical model of subsection 2.3.3, chapter 2 to the numerical experiments with the rectangular basin is justified by this kind of considerations. While in the configurations Cla to C6a, C2a hD, sinl, and sin2 the standing eddy transport tends to reduce the meridional density gradient, the eddy induced reduction of this gradient is not a leading order effect in configuration rec B.

---

heat content that is advected with the mean flow contributes to local buoyancy changes, namely that part of the heat content which results from temperature differences within the fluid. Therefore, the temperature transport relative to an appropriate reference temperature gives a better estimate of the relevant part of the total heat transport.

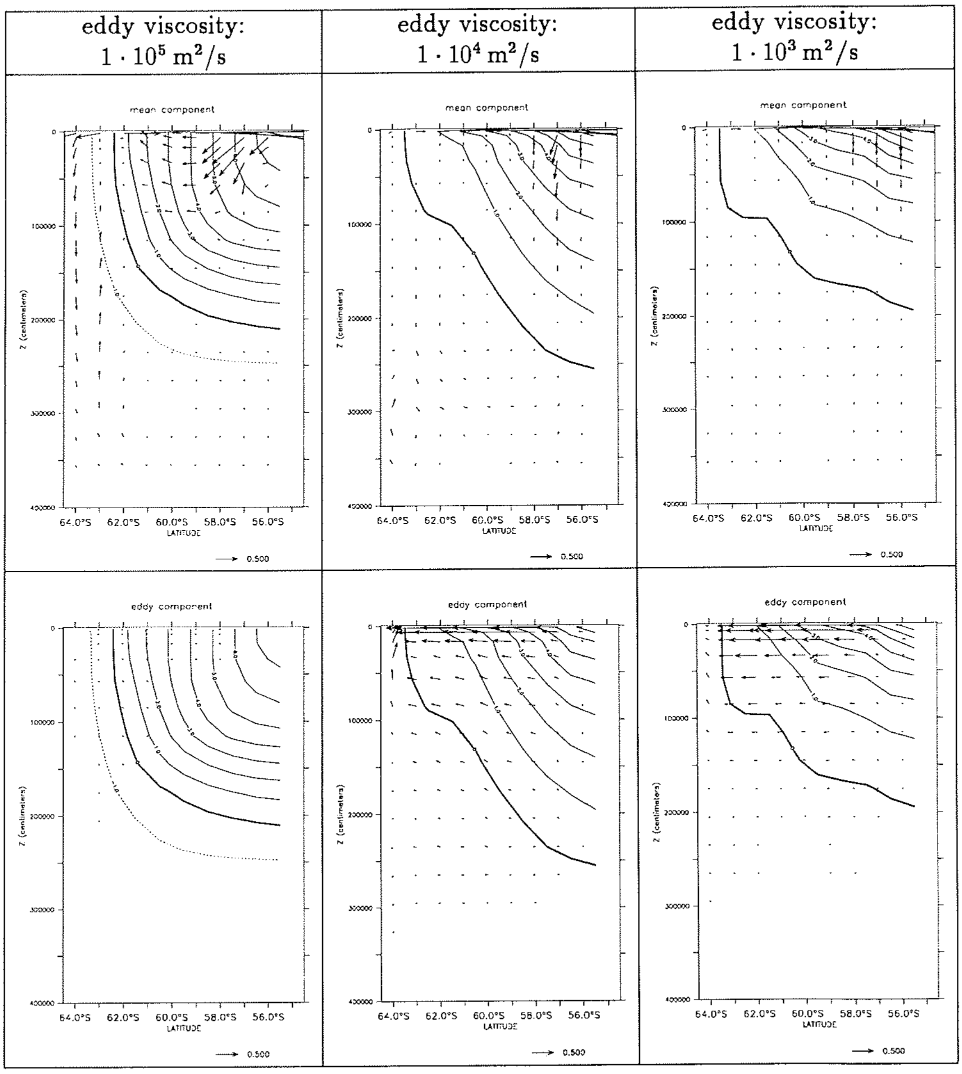

Figure 3.17: Zonal mean and standing eddy components of the meridional temperature transport $\left(\overline{\theta \cdot v}, \overline{\theta \cdot w}\right)$ relative to 0°C for the configuration C2a, where the overbar denotes zonal averages. The three columns show experiments with different horizontal eddy viscosities, where viscosity is decreasing from the left to the right. The top row shows the mean component $\left(\overline{\theta} \cdot \overline{v}, \overline{\theta} \cdot \overline{w}\right)$, and the bottom row the standing eddy component $\left(\overline{\theta' \cdot v'}, \overline{\theta' \cdot w'}\right)$, where primes denote the deviation from the zonal average. Overlaid are isolines of the zonally averaged potential temperature $\overline{\theta}$. The units are °C · cm/s and the vertical component of the vectors is 500 times exaggerated.

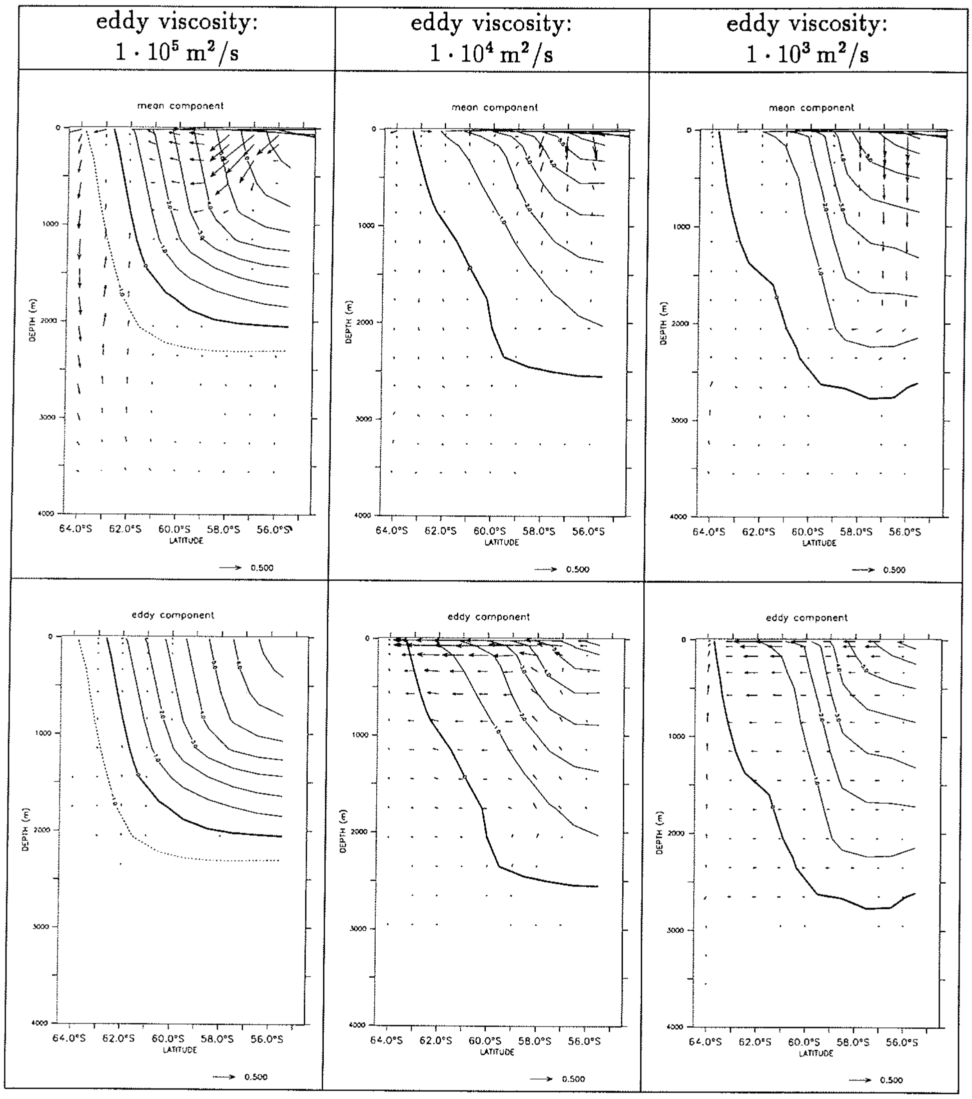

Figure 3.18: Same as figure 3.17, but for configuration sinl

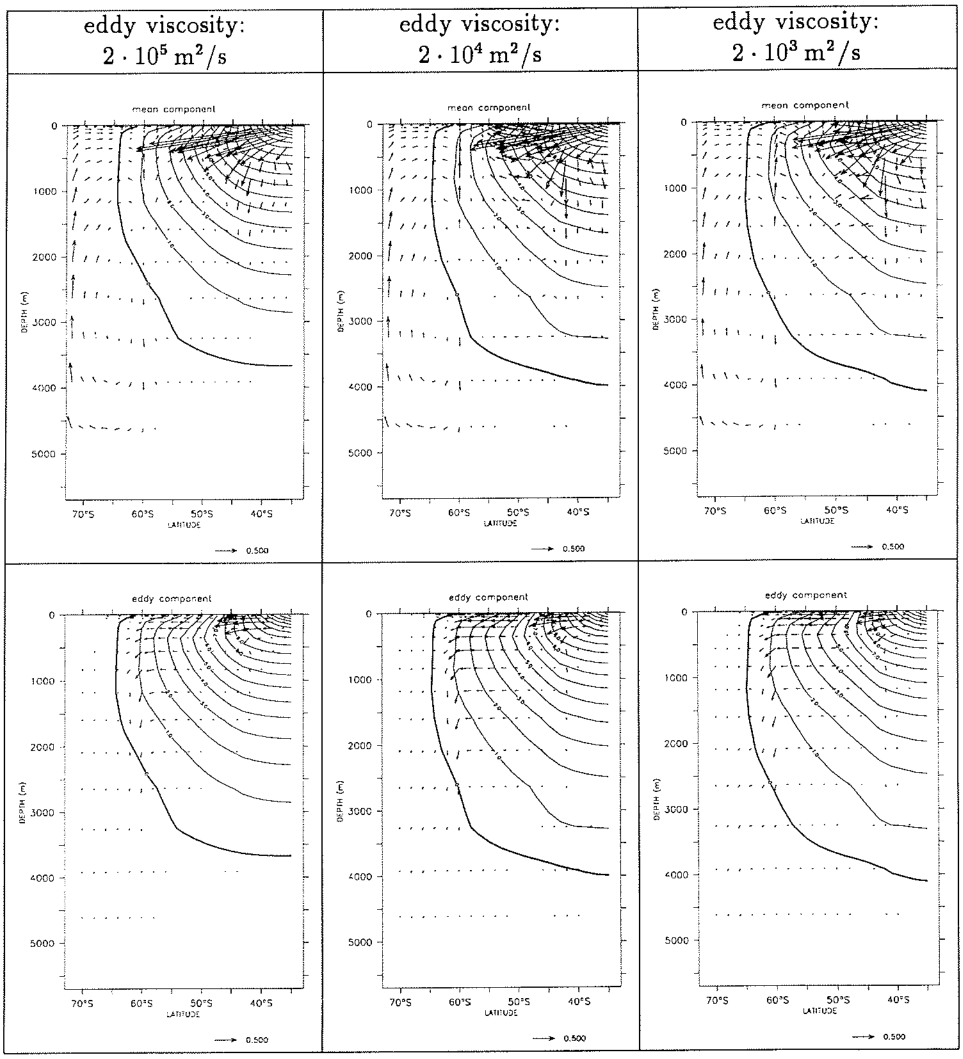

eddy viscosity: $2 \cdot 10^5\,\mathrm{m}^2/\mathrm{s}$

eddy viscosity: $2 \cdot 10^4\,\mathrm{m}^2/\mathrm{s}$

eddy viscosity: $2 \cdot 10^3\,\mathrm{m}^2/\mathrm{s}$

Figure 3.19: Same as figure 3.17, but for configuration rec B. Here, the vertical component of the vectors is only 5 times exaggerated.

3.5.3 Vertical momentum transfer

The standing eddy induced meridional buoyancy transport is connected to a vertical transfer of zonal momentum. The interfacial form stress (IFS) is a "stress" on an isopycnal layer by the pressure at its lower isopycnal i. It is given by:

$$\mathrm{IFS} = \frac{1}{\rho_0} \oint p_\mathrm{i} \frac{\partial h_\mathrm{i}'}{\partial x}\,\mathrm{d}x = -\frac{1}{\rho_0} \oint \frac{\partial p_\mathrm{i}}{\partial x} h_\mathrm{i}'\,\mathrm{d}x \approx -f \frac{\oint v_\mathrm{g}' \sigma'\,\mathrm{d}x}{\partial\overline{\sigma}/\partial z} \tag{3.5}$$

where p_i is the pressure at the isopycnal i, h_i the height of the isopcnal i, v_g the meridional geostrophic velocity, and σ the potential density. Overbars denote zonal averages and primes the deviation from the zonal average. In the last formulation of the interfacial form stress the interface height is approximated by a truncated Taylor expansion: $h_\mathrm{i}' \approx \sigma'(\partial\overline{\sigma}/\partial z)^{-1}$. If the vertical excursions of the isopycnals are small, (3.5) gives a vertical transfer of zonal momentum.

The vertical transfer of zonal momentum due to eddy activity is usually expressed by the vertical component I_z of the Eliassen-Palm vector (see e.g., Andrews & McIntyre (1976), James (1994), Stevens & Ivchenko (1997), and Olbers & Ivchenko (2001)). For large scale flows it may be written as:

$$I_z = -f\left(\Phi_\mathrm{standing} + \Phi_\mathrm{transient}\right) \tag{3.6}$$

with the standing and transient eddy streamfunctions[5]:

$$\Phi_\mathrm{standing} = \frac{\displaystyle\int_\mathrm{west}^\mathrm{east} \widehat{v}'\,\widehat{\sigma}'\,\mathrm{d}x}{\dfrac{\partial\widehat{\overline{\sigma}}}{\partial z}} \qquad\qquad \Phi_\mathrm{transient} = \frac{\displaystyle\int_\mathrm{west}^\mathrm{east} \widehat{v^\star\sigma^\star}\,\mathrm{d}x}{\dfrac{\partial\widehat{\overline{\sigma}}}{\partial z}} \tag{3.7}$$

(Here, the hats denote time averages and stars the deviations from the time average.)

---

[5] The idea that is expressed by introducing eddy streamfunctions is the following (see e.g., Andrews & McIntyre (1976), McIntosh & McDougall (1996), McDougall & McIntosh (2001), Olbers & Ivchenko (2001), and Lee & Coward (2003)). If the eddies transport buoyancy along isopycnals, thus: $\frac{\partial\widehat{\overline{\sigma}}}{\partial y}\int_\mathrm{west}^\mathrm{east}\widehat{v}'\,\widehat{\sigma}'\,\mathrm{d}x = -\frac{\partial\widehat{\overline{\sigma}}}{\partial z}\int_\mathrm{west}^\mathrm{east}\widehat{w}'\,\widehat{\sigma}'\,\mathrm{d}x$, the divergence of the zonally integrated eddy induced buoyancy fluxes can be written as:

$$\frac{\partial}{\partial y}\left(\int_\mathrm{west}^\mathrm{east}\widehat{v}'\,\widehat{\sigma}'\,\mathrm{d}x\right) + \frac{\partial}{\partial z}\left(\int_\mathrm{west}^\mathrm{east}\widehat{w}'\,\widehat{\sigma}'\,\mathrm{d}x\right) = \frac{\partial\Phi_\mathrm{standing}}{\partial y}\frac{\partial\widehat{\overline{\sigma}}}{\partial z} - \frac{\partial\Phi_\mathrm{standing}}{\partial z}\frac{\partial\widehat{\overline{\sigma}}}{\partial y}$$

(and likewise for the transient eddies). Thus the effects of the eddies on the zonal mean potential density may then be written as an advection of the zonal mean potential density with an eddy induced meridional overturning circulation defined by eddy streamfunctions.

In high resolution ocean models an eddy driven anti Deacon cell is found to compensate the Deacon cell which is present in the Eulerian overturning streamfunction Φ - see e.g., McIntosh & McDougall (1996), Olbers & Ivchenko (2001), and Lee & Coward (2003) for more details.

Figure 3.20 shows the standing eddy streamfunction Φ_{standing} of the configuration C2a with a horizontal eddy viscosity of $1 \cdot 10^3 \text{m}^2/\text{s}$. South of 60°S the stratification is very weak (compare with figure 3.17) and very high negative values are obtained for Φ_{standing}. There, the condition of small vertical excursions of the isopycnals is not met and the truncated Tayler expansion of the interface height in not a good approximation. North of 60°S Φ_{standing} shows an eddy induced meridional overturning that opposes the wind induced Eulerian overturning (compare with figure 3.3). Transient eddies were not relevant in the coarse resolution models of the present chapter and the transient eddy streamfunction is not discussed here.

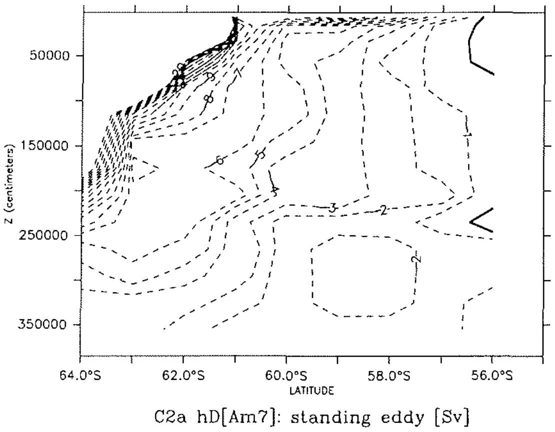

Figure 3.20: Standing eddy streamfunction Φ_{standing} of the configuration C2a with a horizontal eddy viscosity of $1 \cdot 10^3 \text{m}^2/\text{s}$. Φ_{standing} is calculated from (3.7).

With (3.6) figure 3.20 may interpreted as follows: Zonal momentum that is input at the surface by wind stress is transferred downwards by standing eddy interfacial form stress to the depth of the topography where it is removed from the system by bottom form stress. This is consistent with the ideas developed in Völker (1995, 1999), and Olbers & Völker (1996) (see subsection 1.2.2, chapter 1 of this thesis), where the standing eddies play a crucial rôle in regulating the channel transport. Through the mechanism of baroclinic topographic resonance of Rossby waves the standing eddies lock in phase to the topography in such a way that the zonal momentum is removed in the above manner. These ideas are further exploited in Chapter 5 where a modified version of the low order model of Völker (1995, 1999) and Olbers & Völker (1996) is developed.

3.5.4 Intermediate summary

Standing eddies significantly influence the zonal momentum balance as well as the meridional buoyancy transport in the zonally periodic channel with topography (i.e. configurations C1a to C6a, C2a hD, sin1, and sin2) when moderate or low eddy viscosities are used. Concerning the zonal momentum balance the standing eddies are more relevant for the vertical transfer of zonal momentum through the water column than for the removal of zonal momentum at the bottom topography. Concerning the meridional buoyancy transport standing eddies tend to compensate the wind induced meridional overturning circulation. Thereby, while the wind induced overturning circulation acts to increase the meridional density gradient and thus the channel transport, the standing eddies act to reduce the meridional density gradient and the channel transport.

In the rectangular basin with circumpolar connection (configuration rec B) the standing eddies are much less significant. The zonal wind stress is balanced by bottom form stress without a major contribution of the standing eddies. The meridional density gradient is strengthened by the wind induced overturning circulation and the channel transport is increased.

3.6 Closed gyres within channel geometry

The barotropic streamfunction Ψ for the experiments with an eddy viscosity of $10^3\,\mathrm{m}^2/\mathrm{s}$ in the configurations C1a to C6a, and C2a hD shows closed gyres just downstream of the meridional ridge (see figures 3.2 to 3.7, and 3.9). These gyres extend vertically from the surface to the bottom, and are related to the surface wind forcing (see figure 2.1) in a way that reminds at classical Munk gyres (see Pedlosky (1996), chapter 2 for a textbook). Such closed gyres can also be found in other channel models with a meridional ridge that blocks the channel (see e.g., McWilliams et al. (1978), their configuration TB and their figure 2, Wolff et al. (1991), their configuration BR and their figure 10, and MacCready & Rhines (2001), their figure 5). However, the classical Munk gyres require continental boundaries at which frictional boundary layer currents can be formed. Thus the question arises of how such gyres are balanced in the absence of continental boundaries to the west of the gyres.

Considering the streamfunction plots of the figures 3.2 to 3.7 it looks like the meridional ridge plays the rôle of continental boundaries in gyre dynamics. The zonal cross sections of the potential temperature shows that the position of the meridional ridge is clearly reflected in the vertical excursions of the isopycnals (which are in this case equivalent to the isothermals since salinity was kept constant) throughout the water column. But the question is, how are the strong meridional currents at the west of the gyres balanced if not by friction as in the classical Munk solution.

In opposition to the classical theory of ocean gyres, where the oceanic basins are assumed to have flat bottoms and vertical sidewalls, Hughes (2000) and Hughes & de Cuevas (2001) argued that in realistic model configurations with sloping continental boundaries the western boundary currents should be expected to be inviscid. Using Stokes' theorem Hughes (2000) and Hughes & de Cuevas (2001) showed that if the zonal wind stress is in the zonal integral balanced by bottom form stress then the wind stress curl is in the zonal integral (and after meridional averaging over a few degrees of latitude) balanced by the bottom pressure torque rather than by viscous torques as assumed in the classical theory. In their analysis of the results of a high resolution global ocean model Hughes and De Cuevas showed that (β times) the meridional volume transport within the western boundary currents is to the leading order balanced by bottom pressure torque at the continental shelfs. Thus the wind driven ocean gyres may be closed by inviscid boundary currents above sloping topographies instead of viscid boundary currents at vertical sidewalls. In the case of the experiments considered in this chapter this inviscid boundary currents are formed at the meridional ridge which blocks the channel.

So then, why are the closed gyres only present in the experiments with low horizontal eddy viscosities? The width of a boundary layer where horizontal friction is significant is given by the Munk scale δ_{M} which is given by (see (Pedlosky, 1996, chapter 2) for a textbook):

$$\delta_{\mathrm{M}} = \left(\frac{A_h}{\beta}\right)^{\frac{1}{3}} \tag{3.8}$$

where A_h is the horizontal eddy viscosity and β the meridional gradient of the Coriolis frequency. Evaluating β at the center of the channel one obtains a Munk scale of around 255 km, 120 km, and 55 km for horizontal eddy viscosities of $10^5\,\mathrm{m}^2/\mathrm{s}$, $10^4\,\mathrm{m}^2/\mathrm{s}$, and $10^3\,\mathrm{m}^2/\mathrm{s}$, respectively. From the figures 3.2 to 3.7 and 3.9 the distance of the center of the gyres to the vertical sidewalls north and south of the channel is around 2° in latitude or 200 km. At the vertical sidewalls no slip conditions are used and for the high end of the horizontal eddy viscosities the distance of the gyre to the side walls is comparable with the Munk scale. Thus the gyres are destroyed by friction and only after reducing the horizontal eddy viscosity the formation of closed gyres is possible.

3.7 Summary

The flow within the zonally periodic channel with topography is highly sensitive to a variation of the horizontal eddy viscosity. This applies to the strength of the channel flow, the shape of the flow, as well as the leading dynamical balances governing the flow. By reducing the eddy viscosity from 10^5 to $10^3\,\mathrm{m^2/s}$ the flow within the thermohaline and wind driven channel first changes from a more or less zonal to a meandering flow and then to a meandering flow with double gyres in the lee of the meridional ridge.[6] Although in some configurations the channel transport first starts to increase with a reduction of the eddy viscosity, the meridional density gradient as well as the channel transport is clearly weaker with an eddy viscosity of $10^3\,\mathrm{m^2/s}$ than with a viscosity of $10^5\,\mathrm{m^2/s}$. Parallel to this the energy balance changes from a balance between the energy input by wind stress and a frictional energy sink to a balance where the energy is removed from the system by conversion into potential energy, and the zonal momentum balance switches from a compensation of the zonal wind stress by friction to a compensation by bottom form stress, where the later balances of energy and momentum are usually considered as being typical for ACC dynamics. The standing eddies (i.e. the meandering of the flow plus the closed gyres) that develop when the viscosity is reduced (so that they are not damped away by friction) have two important effects: Firstly they induce a downgradient meridional buoyancy transport and thus reduce the meridional density gradient and the channel transport. Secondly, they induce an interfacial form stress with a downward transfer of zonal momentum, where the zonal momentum is then removed at the meridional ridge by bottom form stress. Together with the mechanism of baroclinic topographic resonance of Rossby waves (see Völker (1995, 1999) and Olbers & Völker (1996)) the effects of standing eddies on the zonal momentum balance are further discussed in the next chapter.

In contrast to the zonally periodic channel with topography, the rectangular basin with circumpolar connection did not seem to be very sensitive to a variation of the viscosity at all. Although some weak gyres did develop north and south of the circumpolar connection, the flow kept to be more are less zonal with any eddy viscosity used. The channel transport did not change very much and the zonal wind stress is balanced by bottom form stress right from the beginning. In the rectangular basin with a circumpolar connection the standing eddies seemed not to be very important for a balance between wind stress and bottom form drag - however with reducing the eddy viscosity some fraction of the vertical transfer of zonal momentum did take place through standing eddy interfacial form stress. The physical reasons for these differences between the zonally periodic channel and the rectangular basin are not completely clear and one can thus not draw very strong conclusions concerning the

---

[6] Such a strong north-south excursions of the flow is also known from high resolution isopycnal channel models with a meridional ridge similar to the one used here (see e.g., MacCready & Rhines (2001) and Hallberg & Gnanadesikan (2001)).

question of how sensitive the ACC of a global configuration should be expected to be. However, in the light of this chapter good candidates are the increased meridional extent of the rectangular basin and the increased horizontal diffusivity. By increasing the meridional extent by a factor of 3 the efficiency of the frictional momentum sink is reduced by about 1.5 orders of magnitude, and by increasing the horizontal diffusivity the damping of the standing eddies is increased. In the next chapter this idea will be tested in a quasi-geostrophic low-order model.

The last short remark concerns the high values of viscosity used in the experiments. The above energy and momentum analysis revealed that a horizontal eddy viscosity of $10^5\,\mathrm{m}^2/\mathrm{s}$ is far to high for the zonally periodic channel with topography. Such a high value for the viscosity led to a balance of energy and momentum which is not typical for ACC dynamics. In eddy resolving models the strategy is to use the least value of viscosity so that the model is still numerically stable. The eddy transports are then assumed to be calculated explicitly by the model. But in coarse resolution models one has to rely on parameterization schemes for mesoscale eddies. In this chapter a very crude parameterization of mesoscale eddy transports was used (see footnote on page 63). In coarse resolution models this parameterization scheme usually requires very high values of the eddy viscosity. The effects of this parameterization on the flow within channel models was studied in this chapter and the flow turned out to be very sensitive to changes of the governing parameter of this parameterization scheme. This also points to the importance of developing good parameterization schemes for mesoscale eddy effects. Here, much work is in progress, reviews are given e.g., in Wolff (1999) and McDougall & McIntosh (2001).

Chapter 4

Low-order channel dynamics

4.1 Introduction

Using a low-order model based on a two-layer quasi-geostrophic model Völker (1995), Olbers & Völker (1996), and Völker (1999) studied the rôle of standing eddies in setting up the zonal momentum balance and the mean transport in a zonally periodic channel with topography. By including a topographic obstacle into his model, Völker (1995, 1999) allowed for the effects of bottom form drag and bottom pressure torque. The geostrophic contours of this model were designed to close through the zonally-periodic continuation of the channel. Völker included bottom friction and a friction between the two layers, excluded horizontal friction, and forced the model by a zonal wind stress at the surface of the channel.

For a suitable combination of parameter values three steady states coexist within this model. Two of them are stable and one is unstable. Within one stable steady state the imposed wind forcing is mainly balanced by bottom friction and the total transport through the channel is relatively high. Within the other steady state the wind forcing is mainly balanced by bottom form drag and the total transport is substantially smaller. A steady state momentum balance between the wind stress and the bottom form drag is possible due to the mechanism of baroclinic topographic resonance of Rossby waves, where the waves become trapped by the counteraction of advection and wave propagation. The Rossby waves that are excited by the mean flow at the topography do become stationary and with a suitable phase shift between the trapped Rossby waves and the topography a bottom form drag is established that opposes and balances the wind forcing.

In the present chapter the model of Völker is slightly modified to be applicable to experiments similar to the experiments of chapter 3. It is then discussed whether this (modified) low-order model may help to understand some of the observations of chapter 3.

4.2 Formulation of the model equations

In the following four subsections the equations of the low-order model for the zonally periodic channel with blocked geostrophic contours are derived. This model is very similar to the low-order model developed in Völker (1995, 1999), and so is the derivation of the model equations. Substantial differences to Völker (1995, 1999) are mentioned explicitly.

4.2.1 A two-layer quasi-geostrophic model

The starting point is a two-layer model which allows a simple representation of a vertical stratification. The first layer extends from the surface at $z = 0$ to a variable interface at $z = Z_{\mathrm{I}}(x, y, t)$, and the second from the interface to the bottom at $z = Z_{\mathrm{B}}(x, y)$. The meridional extent of the model domain is D with vertical walls at the northern and southern boundary. The zonal length is L and the channel has periodic boundary conditions in the zonal direction. Using the Boussinesq, the hydrostatic, the β-plane, and the rigid-lid approximation, assuming a small Rossby number and assuming the vertical excursions ot the interface and bottom topography to be small, one can apply the quasi-geostrophic vorticity equation as:

$$\frac{\partial}{\partial t} q_1 + \mathcal{J}\left(\Psi_1, q_1\right) = \frac{f_0}{H_1}\left(w_{\mathrm{E}} - w^{\star}\right) + \mathrm{curl}_z \mathcal{T}_1 \tag{4.1}$$

$$\frac{\partial}{\partial t} q_2 + \mathcal{J}\left(\Psi_2, q_2\right) = \frac{f_0}{H_2} w^{\star} + \mathrm{curl}_z \mathcal{T}_2 \tag{4.2}$$

with the quasi-geostrophic potential vorticities q_1 and q_2 of the first and second layer, respectively:

$$q_1 = \nabla^2 \Psi_1 + \beta y + \frac{f_0}{H_1} Z_{\mathrm{I}} \tag{4.3}$$

$$q_2 = \nabla^2 \Psi_2 + \beta y - \frac{f_0}{H_2} Z_{\mathrm{I}} + \frac{f_0}{H_2} Z_{\mathrm{B}} \tag{4.4}$$

(For more details see e.g., Pedlosky (1996), chapter 3.) Ψ_1 and Ψ_2 are the quasi-geostrophic streamfunctions of the two layers, where the horizontal velocities $\vec{u}_1$ and $\vec{u}_2$ of the two layers are given by:

$$\vec{u}_1 = \frac{1}{\rho_0 f_0} \vec{k} \times \nabla \Psi_1 \qquad \vec{u}_2 = \frac{1}{\rho_0 f_0} \vec{k} \times \nabla \Psi_2 \tag{4.5}$$

$\vec{k}$ is a vertical unit vector, ρ_0 a reference density, and f_0 a reference Coriolis frequency. H_1 and H_2 are the mean layer ticknesses, β the meridional gradient of the Coriolis frequency, (x, y, z) the spatial coordinates, and t the coordinate for time. Since the system is taken to be hydrostatic, the interface height Z_{I} may be written as:

$$Z_{\mathrm{I}} = -\frac{f_0}{\gamma}(\Psi_1 - \Psi_2) - H_1 \tag{4.6}$$

where γ is the reduced gravity defined by:

$$\gamma = \frac{\rho_2 - \rho_1}{\rho_0} g \tag{4.7}$$

ρ_1 and ρ_2 are the densities of the first and second layer, respectively, and g is the gravitational acceleration. γ is an externally prescribed constant as usual in quasi-geostrophic models. The wind forcing is represented by an externally given Ekman pumping velocity w_{E} at the top of layer 1, with

$$w_{\mathrm{E}} = \mathrm{curl}_z \left(\frac{\vec{\tau}}{f_0 \rho_0} \right) \tag{4.8}$$

and $\vec{\tau}$ is the surface wind stress. Consistent to the numerical experiments conducted in chapter 3 with a primitive equation model, the frictional terms are written as downgradient mixing of zonal momentum with the horizontal viscosity A:

$$\mathrm{curl}_z \mathcal{T}_1 = A\, \nabla^4 \Psi_1 \qquad\qquad \mathrm{curl}_z \mathcal{T}_2 = A\, \nabla^4 \Psi_2 \tag{4.9}$$

Diabatic processes are expressed through the cross interfacial velocity $w^\star$ which is defined by:

$$\begin{aligned} w^\star &= [w_1]_{(z=Z_{\mathrm{I}})} - \left[\frac{\partial Z_{\mathrm{I}}}{\partial t} + \vec{u}_1 \cdot \nabla Z_{\mathrm{I}} \right] \qquad (4.10) \\ &= [w_2]_{(z=Z_{\mathrm{I}})} - \left[\frac{\partial Z_{\mathrm{I}}}{\partial t} + \vec{u}_2 \cdot \nabla Z_{\mathrm{I}} \right] \end{aligned}$$

In the present model, the diabatic processes are expressed as the sum of an external heating Q and a diffusion of the interface height Z_{I} with a diffusivity κ:

$$w^\star = \frac{\alpha Q}{c_p(-\partial \rho / \partial z)} - \kappa \nabla^2 Z_{\mathrm{I}} \tag{4.11}$$

where α is the coefficient of thermal expansion and c_p the specific heat of constant pressure. The diffusion of the interface height may be considered as being equivalent to the diffusion of layer thickness of the Gent & McWilliams (1990) parameterization, thus mesoscale eddy processes are to some extend represented in $w^\star$. Writing the vertical density gradient as $\partial\rho/\partial z = -2\rho_0\gamma/(g[H_1+H_2])$ and using (4.6) for the interface height Z_I results in:

$$w^\star = \frac{1}{2}\frac{g\alpha(H_1+H_2)}{\gamma c_p\rho_0}Q + \frac{\kappa f_0}{\gamma}\nabla^2(\Psi_1-\Psi_2) \tag{4.12}$$

Multiplying (4.1) by $H_1/(H_1+H_2)$, and (4.2) by $H_2/(H_1+H_2)$, subsequently adding (4.1) and (4.2), and using (4.3), (4.4), (4.6), (4.7), (4.9), and (4.12) a barotropic vorticity equation is obtained:

$$\begin{aligned}\frac{\partial}{\partial t}\nabla^2\Phi_e + \mathcal{J}\left(\Phi_e,\nabla^2\Phi_e\right) + \frac{H_1H_2}{(H_1+H_2)^2}\mathcal{J}\left(\Phi_i,\nabla^2\Phi_i\right) + \beta\frac{\partial}{\partial x}\Phi_e \\ + \frac{f_0}{H_1+H_2}\mathcal{J}\left(\Phi_e,Z_\mathrm{B}\right) - \frac{f_0H_1}{(H_1+H_2)^2}\mathcal{J}\left(\Phi_i,Z_\mathrm{B}\right) = \frac{f_0w_\mathrm{E}}{H} + A\nabla^4\Phi_e\end{aligned} \tag{4.13}$$

where Φ_e and Φ_i are the barotropic (external) and baroclinic (internal) streamfunctions defined by:

$$\Phi_e = \frac{H_1\Psi_1+H_2\Psi_2}{H_1+H_2} \qquad \Phi_i = \Psi_1-\Psi_2 \tag{4.14}$$

Similarly, by subtracting (4.2) from (4.1), and inserting the above equations a baroclinic vorticity equation may be written as:

$$\begin{aligned}\frac{\partial}{\partial t}\nabla^2\Phi_i - \frac{1}{R^2}\frac{\partial}{\partial t}\Phi_i + \mathcal{J}\left(\Phi_e,\nabla^2\Phi_i\right) + \mathcal{J}\left(\Phi_i,\nabla^2\Phi_e\right) + \frac{H_2-H_1}{H_1+H_2}\mathcal{J}\left(\Phi_i,\nabla^2\Phi_i\right) + \beta\frac{\partial}{\partial x}\Phi_i \\ - \frac{1}{R^2}\mathcal{J}\left(\Phi_e,\Phi_i\right) - \frac{f_0}{H_2}\mathcal{J}\left(\Phi_e,Z_\mathrm{B}\right) + \frac{f_0H_1}{H_2(H_1+H_2)}\mathcal{J}\left(\Phi_i,Z_\mathrm{B}\right) \\ = \frac{f_0w_\mathrm{E}}{H_1} - \frac{1}{2}\frac{g\alpha(H_1+H_2)}{f_0c_p\rho_0R^2}Q - \frac{\kappa}{R^2}\nabla^2\Phi_i + A\nabla^4\Phi_i\end{aligned} \tag{4.15}$$

where R is the first baroclinic Rossby radius defined by:

$$R^2 = \frac{\gamma H_1H_2}{f_0^2(H_1+H_2)} \tag{4.16}$$

The dynamics of the quasi-geostrophic two-layer model used to develop the low-order model is determined by the vorticity equations (4.13) and (4.15). In the following subsections, a low-order expansion of the vorticity equations is done, the thermohaline and wind forcing is specified in more detail, and suitable boundary conditions are added. There are four main differences to the model formulated by Völker (1995, 1999):

1. While Völker (1995, 1999) used the planetary-geostrophic approximation and disregarded the relative vorticity, here it is retained.
2. Völker (1995, 1999) included bottom friction as well as a term called interfacial friction. Here, horizontal friction is used instead of bottom friction.
3. In the present model, a diffusion of the interfacial height is included. In a quasi-geostrophic model this is equivalent to interfacial friction - see discussion in Rhines & Young (1982) and Olbers et al. (1985).
4. A thermal forcing Q is included in the model of this chapter.

4.2.2 Low-order development

The barotropic and baroclinic streamfunctions Φ_e and Φ_i can be written as Fourier series:

$$\Phi_e(x,y,t) = \sum_{n=1}^{\infty}\left[\sum_{m=0}^{\infty} c^c_{e,m,n}(t)\,\mathcal{F}^c_{m,n}(x,y) + \sum_{m=1}^{\infty} c^s_{e,m,n}(t)\,\mathcal{F}^s_{m,n}(x,y)\right] + c_{e,0,0}(t) \quad (4.17)$$

$$\Phi_i(x,y,t) = \sum_{n=1}^{\infty}\left[\sum_{m=0}^{\infty} c^c_{i,m,n}(t)\,\mathcal{F}^c_{m,n}(x,y) + \sum_{m=1}^{\infty} c^s_{i,m,n}(t)\,\mathcal{F}^s_{m,n}(x,y)\right] + c_{i,0,0}(t) \quad (4.18)$$

where $c^c_{e,m,n}$, $c^s_{e,m,n}$, $c^c_{i,m,n}$, and $c^s_{i,m,n}$ are Fourier coefficients, and the basic functions $\mathcal{F}^c_{m,n}$ and $\mathcal{F}^s_{m,n}$ are defined by:

$$\mathcal{F}^c_{m,n}(x,y) = \cos\left(\frac{2m\pi x}{L}\right)\cdot\sin\left(\frac{n\pi y}{D}\right) \quad (4.19)$$

$$\mathcal{F}^s_{m,n}(x,y) = \sin\left(\frac{2m\pi x}{L}\right)\cdot\sin\left(\frac{n\pi y}{D}\right) \quad (4.20)$$

$\mathcal{F}^c_{m,n}$ and $\mathcal{F}^s_{m,n}$ are orthogonal functions, and the quasi-geostrophic vorticity equations (4.13) and (4.15) may be projected on the $\mathcal{F}^c_{m,n}$ and $\mathcal{F}^s_{m,n}$. Introducing the projection operators $\langle\ldots\rangle^c_{m,n}$ and $\langle\ldots\rangle^s_{m,n}$ as:

$$\langle\mathcal{A}\rangle^c_{m,n}(t) = \frac{4}{LD}\int_{y=0}^{D}\int_{x=0}^{L}\mathcal{A}(x,y,t)\,\mathcal{F}^c_{m,n}(x,y)\,\mathrm{d}x\,\mathrm{d}y \quad \text{with} \quad m\neq 0, n\neq 0 \quad (4.21)$$

$$\langle\mathcal{A}\rangle^c_{m,n}(t) = \frac{2}{LD}\int_{y=0}^{D}\int_{x=0}^{L}\mathcal{A}(x,y,t)\,\mathcal{F}^c_{m,n}(x,y)\,\mathrm{d}x\,\mathrm{d}y \quad \text{with} \quad m = 0, n\neq 0 \quad (4.22)$$

$$\langle\mathcal{A}\rangle^s_{m,n}(t) = \frac{4}{LD}\int_{y=0}^{D}\int_{x=0}^{L}\mathcal{A}(x,y,t)\,\mathcal{F}^s_{m,n}(x,y)\,\mathrm{d}x\,\mathrm{d}y \quad \text{with} \quad m\neq 0, n\neq 0 \quad (4.23)$$

and using the full Fourier expansion (4.17), (4.18) the partial differential equations (4.13) and (4.15) are equivalent to a set of ordinary differential equations, e.g.:

$$\langle \text{lhs} \rangle^c_{m,n}(t) = \langle \text{rhs} \rangle^c_{m,n}(t) \quad \text{with} \quad m = 0,1,2,3,\ldots \quad \text{and} \quad n = 1,2,3,\ldots \tag{4.24}$$

$$\langle \text{lhs} \rangle^s_{m,n}(t) = \langle \text{rhs} \rangle^s_{m,n}(t) \quad \text{with} \quad m = 1,2,3,\ldots \quad \text{and} \quad n = 1,2,3,\ldots \tag{4.25}$$

where lhs and rhs are the left-hand-side and right-hand-side of (4.13) and (4.15).

The idea of a low-order model is to truncate the Fourier expansion after only a few Fourier modes (e.g., after the modes with $m + n \leq 2$) and to project the dynamic equations only on these few Fourier modes. Thereby, a simple model is obtained that is easily accessible to the methods of dynamical system theory. But, strictly speaking, such a low-order model is only a valid representation of the original model if the convergence after few Fourier modes is shown. Usually this is not very easy or even not possible. However, a low-order model may still be an useful heuristic tool to gain some general understanding of the dynamics of the system under consideration and to develop appropriate notions to describe the general dynamical characteristics. Low-order models were for example employed by Charney & DeVore (1979) and Charney & Straus (1980) to study effects of the resonance of Rossby waves in the atmosphere and to introduce the idea of atmospheric blocking. Völker (1995, 1999) applied the idea of the resonance of Rossby waves and the method of low-order models to the Southern Ocean dynamics (see subsection 1.2.2 of chapter 1). In this chapter a slight modification of Völkers low-order model is used to study some effects observed in chapter 3, particularly the sensitivity of the channel transport to a variation of the horizontal eddy viscosity. Using a low-order model as a heuristic tool, the results should be verified by comparison with the results of a more complete model, in the present case they are compared with the results of chapter 3.

In order to do a sensible low-order truncation it is now first discussed what physical properties are preserved by the basic functions defined by (4.19) and (4.20). At $y = 0$ and $y = D$, $\mathcal{F}^c_{m,n}(x,y)$ and $\mathcal{F}^s_{m,n}(x,y)$ are identical to zero, so that the condition of no mass flux through the vertical wall at the southern and northern boundaries of the channel is guaranteed. In addition, $\nabla^2\mathcal{F}^c_{m,n}$ and $\nabla^2\mathcal{F}^s_{m,n}$ vanish at $y = 0$ and $y = D$. Thus no horizontal momentum flux across the southern or northern boundaries result from terms in Φ_e and Φ_i proportional to $\mathcal{F}^c_{m,n}$ and $\mathcal{F}^s_{m,n}$. Since $\left[\mathcal{F}^c_{m,n}\right]_{(y=D)} - \left[\mathcal{F}^c_{m,n}\right]_{(y=0)} = \left[\mathcal{F}^s_{m,n}\right]_{(y=D)} - \left[\mathcal{F}^s_{m,n}\right]_{(y=0)} = 0$ no channel transport can be represented with the basic functions $\mathcal{F}^c_{m,n}$ and $\mathcal{F}^s_{m,n}$. Thus, for the expansion of Φ_e and Φ_i to represent a flow with a net channel transport a further term must be added to the expansion. In the present model, this additional term is taken to be proportional to:

$$\mathcal{F}^{\star}(x,y) = \cos\left(\frac{\pi y}{D}\right) \tag{4.26}$$

Terms proportional to $\mathcal{F}^\star(x,y)$ still satisfy the condition of no mass flux through the southern and northern boundary of the channel, but these terms represent a not vanishing channel transport and do result in a frictional horizontal momentum flux across these boundaries. One purpose of the present low-order model is to study the sensitivity of the flow to a variation of the efficiency of the horizontal frictional momentum sink. Therefore, the representation of frictional momentum fluxes across the horizontal boundaries is important. Völker (1995, 1999) used instead of $\mathcal{F}^\star(x,y)$ a linear function of y. Since he included bottom friction and excluded horizontal friction this is a suitable choice for Völkers model. But, this choice would result in zero frictional momentum flux across horizontal boundaries and is thus not appropriate for the present model.

Völker regarded the inclusion of horizontal friction into a low-order model as problematic, since one generally would expect the development of frictional boundary layers which can not be resolved within a low-order model. However, in the numerical experiments of chapter 2 and 3, no strong frictional boundary layers showed up. Thus, in the present low-order model the boundary layers are not regarded as being very problematic and horizontal friction is included within the model. Still, this can not be justified a priori.

Following Völker (1995, 1999) the most simple model that retains a feedback of the topography on the mean channel flow does only include the Fourier modes with $m+n=2$ and $m \geq 0$, $n > 0$. Truncating in (4.17) and (4.18) all terms with $m+n \neq 2$, including the terms $T_e(t)\,\mathcal{F}^\star(x,y)$ and $T_i(t)\,\mathcal{F}^\star(x,y)$ in the expansion of the barotropic and baroclinic streamfunction, respectively, and substituting $H_e(t) = c^{\mathrm{c}}_{\mathrm{e},0,2}(t) - 8/(3\pi)T_e(t)$, $H_i(t) = c^{\mathrm{c}}_{\mathrm{i},0,2}(t) - 8/(3\pi)T_i(t)$, $C_e(t) = c_{\mathrm{e},0,0}(t)$, $C_i(t) = c_{\mathrm{i},0,0}(t)$, $F_{e,c}(t) = c^{\mathrm{c}}_{\mathrm{e},1,1}(t)$, $F_{e,s}(t) = c^{s}_{\mathrm{e},1,1}(t)$, $F_{i,c}(t) = c^{\mathrm{c}}_{\mathrm{i},1,1}(t)$, and $F_{i,s}(t) = c^{s}_{\mathrm{i},1,1}(t)$ the low-order expansions of Φ_e and Φ_i become:

$$\begin{aligned}\Phi_e^{\mathrm{trunc}}(x,y,t) = {} & T_e(t)\cos\left(\frac{\pi y}{D}\right) + H_e(t)\sin\left(\frac{2\pi y}{D}\right) + C_e(t) \\ & + F_{e,c}(t)\cos\left(\frac{2\pi x}{L}\right)\sin\left(\frac{\pi y}{D}\right) + F_{e,s}(t)\sin\left(\frac{2\pi x}{L}\right)\sin\left(\frac{\pi y}{D}\right)\end{aligned} \tag{4.27}$$

$$\begin{aligned}\Phi_i^{\mathrm{trunc}}(x,y,t) = {} & T_i(t)\cos\left(\frac{\pi y}{D}\right) + H_i(t)\sin\left(\frac{2\pi y}{D}\right) + C_i(t) \\ & + F_{i,c}(t)\cos\left(\frac{2\pi x}{L}\right)\sin\left(\frac{\pi y}{D}\right) + F_{i,s}(t)\sin\left(\frac{2\pi x}{L}\right)\sin\left(\frac{\pi y}{D}\right)\end{aligned} \tag{4.28}$$

Next, the topography is specified as:

$$Z_{\mathrm{B}}(x,y) = B \sin\left(\frac{2\pi x}{L}\right) \tag{4.29}$$

Again, the choice is different to the one of Völker (1995, 1999). In a homogeneous channel with blocked geostrophic contours strong boundary layers are known to develop - see e.g., Krupitsky & Cane (1994) and Wang & Huang (1995). To avoid possible problems with boundary layers Völker decided not to use blocked geostrophic contours and chose the topography to be proportional to $\mathcal{F}^{s}_{1,1}(x,y)$. This choice has the advantage that the bottom pressure torque, i.e. the terms in (4.13) and (4.15) linear in $\mathcal{J}\left(\Phi_e, Z_{\mathrm{B}}\right)$ and $\mathcal{J}\left(\Phi_i, Z_{\mathrm{B}}\right)$, do only project on $\mathcal{F}^{s}_{m\pm1,n\pm1}$ for terms in Φ_e or Φ_i proportional to $\mathcal{F}^{s}_{m,n}$, on $\mathcal{F}^{c}_{m\pm1,n\pm1}$ for terms proportional to $\mathcal{F}^{c}_{m,n}$, and on $\mathcal{F}^{c}_{1,1}$ for terms linear in y.

With the choice of (4.29) the bottom pressure torque projects on any $\mathcal{F}^{c}_{m,n'}$ with uneven n' for the terms in Φ_e or Φ_i that are linear in y. Thus, if a non vanishing channel transport is represented by terms linear in y the low-order truncation is problematic even to the lowest order that can represent a net channel transport. In the present low-order model, a not vanishing channel transport is realized by terms proportional to $\mathcal{F}^{\star}$ defined by (4.26). For these terms the bottom pressure torque does only project on $\mathcal{F}^{c}_{1,1}$ and for these terms the present choice of topography does not cause any problems to the low-order truncation. Concerning the terms proportional to $\mathcal{F}^{s}_{m,n}$ or $\mathcal{F}^{c}_{m,n}$ the bottom pressure torque projects on all $\mathcal{F}^{s}_{m,n'}$ or $\mathcal{F}^{c}_{m,n'}$ with even/uneven n' for uneven/even n. Thus with respect to the bottom presure torque that results from the standing eddy components $\mathcal{F}^{s}_{m,n}$, $\mathcal{F}^{c}_{m,n}$ and the topography defined by (4.29) the low-order truncation still is problematic.

The problems mentioned here do result from the possibility of boundary layers in a channel with blocked geostrophic contours. The numerical experiments of chapter 2 and 3 do not point to strong effects of boundary layers if stratification is included, and in this chapter it is assumed that a low-order model may possibly capture some dynamic features of a baroclinic channel with blocked geostrophic contours as long as the standing eddy components do not grow to strong.

The wind stress of the present model is chosen to be the same as in Völker (1995, 1999):

$$\tau^{x} = -\frac{f_0 \rho_0 D}{2\pi}\, w_0 \sin^2\left(\frac{\pi y}{D}\right) \qquad \tau^{y} = 0 \tag{4.30}$$

which implies an Ekman pumping

$$w_{\mathrm{E}}(x,y) = w_0 \cos\left(\frac{\pi y}{D}\right) \sin\left(\frac{\pi y}{D}\right) \tag{4.31}$$

that projects only on $\mathcal{F}^c_{0,2}$. Parallel to this the external heat forcing is chosen to be:

$$Q(x,y) = -Q_0 \cos\left(\frac{\pi y}{D}\right) \sin\left(\frac{\pi y}{D}\right) \tag{4.32}$$

After projecting (4.13) and (4.15) on $\mathcal{F}^c_{0,2}$, $\mathcal{F}^c_{1,1}$, and $\mathcal{F}^s_{1,1}$ and after expanding Φ_e and Φ_i as (4.27) and (4.28) one obtains a system of six ordinary differential equations in t with ten unknown variables $T_e(t)$, $T_i(t)$, $H_e(t)$, $H_i(t)$, $C_e(t)$, $C_i(t)$, $F_{e,c}(t)$, $F_{e,s}(t)$, $F_{i,c}(t)$, and $F_{i,s}(t)$. To complete the dynamical system, four boundary conditions must be supplemented.

4.2.3 Boundary conditions

The barotropic streamfunction Φ_e is only defined up to an arbitrary constant. Thus $C_e(t)$ may be freely chosen, i.e. in the present model as:

$$C_e(t) = 0 \tag{4.33}$$

The auxiliary conditions of McWilliams (1977) are used to specify the remaining three boundary conditions. The first of these is derived from the 3-D continuity equation:

$$\frac{\partial u}{\partial x} + \frac{\partial v}{\partial y} + \frac{\partial w}{\partial z} = 0 \tag{4.34}$$

with the velocity field (u, v, w) and the spatial coordinates (x, y, z). Integrating (4.34) over the whole horizontal domain and vertically from the bottom to the interface yields:

$$\int_{y=0}^{D} \int_{x=0}^{L} w_{(z=Z_I)} \, \mathrm{d}x \, \mathrm{d}y = 0 \tag{4.35}$$

where $w_{z=Z_I}$ is the vertical velocity at the interface. (Here, the assumption of no volume transport through the horizontal boundaries and the bottom was used.) With (4.10) and (4.12) this implies:

$$\int_{y=0}^{D} \int_{x=0}^{L} \left[\frac{\partial}{\partial t} \Phi_i(x,y,t) - \kappa \nabla^2 \Phi_i(x,y,t) - \frac{1}{2} \frac{g\alpha H}{f_0 c_p \rho_0} Q(x,y) \right] \mathrm{d}x \, \mathrm{d}y = 0 \tag{4.36}$$

and after inserting (4.28) and (4.32) one obtains:

$$\frac{\partial}{\partial t} C_i(t) = 0 \tag{4.37}$$

Finally, integrating (4.37) from $C_i(t=0)=0$ gives:

$$C_i(t) = 0 \tag{4.38}$$

The second and third auxiliary condition of McWilliams (1977) follow from the island integral of the horizontal momentum equation, keeping only terms up to first order in the Rossby number. Within the present configuration, these integrals may be written as:

$$\int_{x=0}^{L} \left[\frac{\partial}{\partial y} \left(\frac{\partial}{\partial t} \Phi_e(x,y,t) - A\, \nabla^2 \Phi_e(x,y,t) \right) - \frac{\tau^x}{\rho_0\, H} \right]_{y=0} \mathrm{d}x = 0 \tag{4.39}$$

$$\int_{x=0}^{L} \left[\frac{\partial}{\partial y} \left(\frac{\partial}{\partial t} \Phi_i(x,y,t) - A\, \nabla^2 \Phi_i(x,y,t) \right) - \frac{\tau^x}{\rho_0\, H_1} \right]_{y=0} \mathrm{d}x = 0 \tag{4.40}$$

Inserting (4.27) and (4.28) yields:

$$\frac{\partial}{\partial t} H_e(t) = -A \frac{4\pi^2}{D^2}\, H_e(t) \tag{4.41}$$

$$\frac{\partial}{\partial t} H_i(t) = -A \frac{4\pi^2}{D^2}\, H_i(t) \tag{4.42}$$

And integrating from $H_e(t=0)=0$, $H_i(t=0)=0$ results in:

$$H_e(t) = H_i(t) = 0 \tag{4.43}$$

So, the dynamical system is now completely specified.

4.2.4 The low-order model

Taking the zonal extend L and meridional width D of the channel from figure 2.1 with $L \approx 4000\,\mathrm{km}$ and $D \approx 1000\,\mathrm{km}$ and setting the first baroclinic Rossby radius to $R \approx 20\,\mathrm{km}$ the horizontal scales satisfy the relation:

$$L^2 >> D^2 >> R^2 \tag{4.44}$$

To keep the model simple, in the following, in any sum of L^2, D^2, and R^2 only the largest term is retained. The set of differential equations then becomes:

$$\left(\frac{\partial}{\partial t}T_e\right) = -\left(\frac{3}{16}\frac{D^2 f_0}{\pi H}\right) w_0 - \left(\frac{D f_0}{LH}\right)\left(F_{e,c} - \frac{H_1}{H}F_{i,c}\right) B - \left(\frac{\pi^2 A}{D^2}\right) T_e \tag{4.45}$$

$$\left(\frac{\partial}{\partial t}T_i\right) = -\left(\frac{3}{16}\frac{\pi R^2 f_0}{H_1}\right) w_0 - \left(\frac{3}{32}\frac{\pi H \alpha g}{f_0 c_p \rho_0}\right) Q_0 + \left(\frac{3}{8}\frac{\pi^3}{LD}\right)\left(F_{e,c}\cdot F_{i,s} - F_{e,s}\cdot F_{i,c}\right) \tag{4.46}$$

$$+\left(\frac{\pi^2 R^2 f_0}{LDH_2}\right)\left(F_{e,c} - \frac{H_1}{H}F_{i,c}\right) B - \left(\frac{\pi^2\kappa}{D^2} + \frac{\pi^4 R^2 A}{D^4}\right) T_i$$

$$\left(\frac{\partial}{\partial t}F_{e,c}\right) = \left(2\frac{D^2}{\pi L}\beta - \frac{64}{3}\frac{\pi D}{L^3}T_e\right) F_{e,s} - \left(\frac{64}{3}\frac{\pi H_1 H_2 D}{H^2 L^3}T_i\right) F_{i,s} \tag{4.47}$$

$$+\left(2\frac{D f_0}{LH}\right)\left(T_e - \frac{H_1}{H}T_i\right) B - \left(\frac{\pi^2 A}{D^2}\right) F_{e,c}$$

$$\left(\frac{\partial}{\partial t}F_{i,c}\right) = \left(2\frac{\pi R^2}{L}\beta - \frac{16}{3}\frac{\pi}{LD}T_e\right) F_{i,s} + \left(\frac{16}{3}\frac{\pi}{LD}\right) T_i F_{e,s} \tag{4.48}$$

$$-\left(2\frac{\pi^2 R^2 f_0}{LDH_2}\right)\left(T_e - \frac{H_1}{H}T_i\right) B - \left(\frac{\pi^2\kappa}{D^2} + \frac{\pi^4 R^2 A}{D^4}\right) F_{i,c}$$

$$\left(\frac{\partial}{\partial t}F_{e,s}\right) = -\left(2\frac{D^2}{\pi L}\beta - \frac{64}{3}\frac{\pi D}{L^3}T_e\right) F_{e,c} + \left(\frac{64}{3}\frac{\pi H_1 H_2 D}{H^2 L^3}T_i\right) F_{i,c} \tag{4.49}$$

$$-\left(\frac{\pi^2 A}{D^2}\right) F_{e,s}$$

$$\left(\frac{\partial}{\partial t}F_{i,s}\right) = -\left(2\frac{\pi R^2}{L}\beta - \frac{16}{3}\frac{\pi}{LD}T_e\right) F_{i,c} - \left(\frac{16}{3}\frac{\pi}{LD}\right) T_i F_{e,c} \tag{4.50}$$

$$-\left(\frac{\pi^2\kappa}{D^2} + \frac{\pi^4 R^2 A}{D^4}\right) F_{i,s}$$

where H is the is the mean depth of the channel with:

$$H = H_1 + H_2 \tag{4.51}$$

The set of equations (4.45) to (4.50) may also be written in dimension-free form. Defining a horizontal length scale $\widehat{L}_0 = D/\pi$, a vertical length scale $\widehat{H}_0 = H/\pi$, and a time scale $\widehat{t}_0 = 1/\|f_0\|$ the transformation

$$\frac{1}{\widehat{t}_0} t \to \tau \qquad \frac{1}{\widehat{L}_0}(x, y) \to (\widetilde{x}, \widetilde{y}) \qquad \frac{1}{\widehat{H}_0} z \to \widetilde{z} \tag{4.52}$$

yields:

$$\widetilde{T}_e = \frac{\pi^2 T_e}{\|f_0\|\, D^2}; \qquad \widetilde{F}_{e,c} = \frac{\pi^2 F_{e,c}}{\|f_0\|\, D^2}; \qquad \widetilde{F}_{e,s} = \frac{\pi^2 F_{e,s}}{\|f_0\|\, D^2} \tag{4.53}$$

$$\widetilde{T}_i = \frac{\pi^2 T_i}{\|f_0\|\, D^2}; \qquad \widetilde{F}_{i,c} = \frac{\pi^2 F_{i,c}}{\|f_0\|\, D^2}; \qquad \widetilde{F}_{i,s} = \frac{\pi^2 F_{i,s}}{\|f_0\|\, D^2} \tag{4.54}$$

and:

$$\tau = \|f_0\|\, t \tag{4.55}$$

Defining a dimension-free Rossby radius $\widetilde{R}$, the aspect ratios $\widetilde{D}$, $\widetilde{B}$, and h, a dimension free planetary vorticity gradient $\widetilde{\beta}$, a horizontal Ekman number E_H as well as a generalized Ekman number for the diffusion E_κ, dimension-free forcing terms $\widetilde{w}_0$ and $\widetilde{Q}_0$, and a dimension-free gravitational acceleration $\widetilde{g}$ as:

$$\widetilde{R} = \frac{\pi R}{D}; \qquad \widetilde{D} = \frac{D}{\pi L}; \qquad \widetilde{B} = \frac{\pi B}{H}; \qquad h = \frac{H_1}{H}; \qquad \widetilde{\beta} = \frac{D \beta}{\|f_0\|} \tag{4.56}$$

$$E_H = \frac{\pi^2 A}{\|f_0\|\, D^2}; \quad E_\kappa = \frac{\pi^2 \kappa}{\|f_0\|\, D^2}; \quad \widetilde{w}_0 = \frac{\pi w_0}{\|f_0\|\, H}; \quad \widetilde{Q}_0 = \frac{\alpha Q_0}{\|f_0\|\, c_p \rho_0}; \quad \widetilde{g} = \frac{H_2 g}{f_0^2 D^2} \tag{4.57}$$

the dimension-free form of the set of differential equations becomes:

$$\frac{\partial}{\partial \tau}\widetilde{T}_e = \frac{3}{16}\,\widetilde{w}_0 + \widetilde{D}\,\widetilde{B}\,\left(\widetilde{F}_{e,c} - h\,\widetilde{F}_{i,c}\right) - E_H\,\widetilde{T}_e \tag{4.58}$$

$$\begin{aligned}\frac{\partial}{\partial \tau}\widetilde{T}_i = {} & \frac{3}{16}\,\frac{\widetilde{R}^2}{h}\,\widetilde{w}_0 + \frac{3\,\pi^3}{32}\,\widetilde{g}\,\widetilde{Q}_0 + \frac{3\,\pi^2}{8}\,\widetilde{D}\,\left(\widetilde{F}_{e,c}\cdot\widetilde{F}_{i,s} - \widetilde{F}_{e,s}\cdot\widetilde{F}_{i,c}\right) \\ & - \widetilde{R}^2\,\widetilde{D}\,\widetilde{B}\,\left(\widetilde{F}_{e,c} - h\,\widetilde{F}_{i,c}\right) - \left(E_\kappa + \widetilde{R}^2\,E_H\right)\,\widetilde{T}_i\end{aligned} \tag{4.59}$$

$$\begin{aligned}\frac{\partial}{\partial \tau}\widetilde{F}_{e,c} = {} & \left(2\,\widetilde{D}\,\widetilde{\beta} - \frac{64\,\pi}{2}\,\widetilde{D}^3\,\widetilde{T}_e\right)\,\widetilde{F}_{e,s} - \frac{64\,\pi}{2}\,h\,(1-h)\,\widetilde{D}^3\,\widetilde{T}_i\,\widetilde{F}_{i,s} \\ & - 2\,\widetilde{D}\,\widetilde{B}\,\left(\widetilde{T}_e - h\,\widetilde{T}_i\right) - E_H\,\widetilde{F}_{e,c}\end{aligned} \tag{4.60}$$

$$\begin{aligned}\frac{\partial}{\partial \tau}\widetilde{F}_{i,c} = {} & \left(2\,\widetilde{R}^2\,\widetilde{D}\,\widetilde{\beta} - \frac{16}{3}\,\widetilde{D}\,\widetilde{T}_e\right)\,\widetilde{F}_{i,s} + \frac{16}{3}\,\widetilde{D}\,\widetilde{T}_i\,\widetilde{F}_{e,s} \\ & + 2\,\frac{1}{1-h}\,\widetilde{R}^2\,\widetilde{D}\,\widetilde{B}\,\left(\widetilde{T}_e - h\,\widetilde{T}_i\right) - \left(E_\kappa + \widetilde{R}^2\,E_H\right)\,\widetilde{F}_{i,c}\end{aligned} \tag{4.61}$$

$$\begin{aligned}\frac{\partial}{\partial \tau}\widetilde{F}_{e,s} = {} & -\left(2\,\widetilde{D}\,\widetilde{\beta} - \frac{64\,\pi^2}{3}\,\widetilde{D}^3\,\widetilde{T}_e\right)\,\widetilde{F}_{e,c} + \frac{64\,\pi^2}{3}\,h\,(1-h)\,\widetilde{D}^3\,\widetilde{T}_i\,\widetilde{F}_{i,c} \\ & - E_H\,\widetilde{F}_{e,s}\end{aligned} \tag{4.62}$$

$$\begin{aligned}\frac{\partial}{\partial \tau}\widetilde{F}_{i,s} = {} & -\left(2\,\widetilde{R}^2\,\widetilde{D}\,\widetilde{\beta} - \frac{16}{3}\,\widetilde{D}\,\widetilde{T}_e\right)\,\widetilde{F}_{i,c} - \frac{16}{3}\,\widetilde{D}\,\widetilde{T}_i\,\widetilde{F}_{e,c} \\ & - \left(E_\kappa + \widetilde{R}^2\,E_H\right)\,\widetilde{F}_{i,s}\end{aligned} \tag{4.63}$$

The above set of equations may be interpreted as follows: (4.58) determines the time change of the total depth integrated channel transport $2 \cdot T_e \cdot H$. The terms on the rhs express the forcing by Ekman pumping (first term), the bottom pressure torque (second term) expressed in terms of standing eddy bottom flow times topography height, and a vorticity sink due to horizontal eddy viscosity (last term). The time change of the channel flow relative to the bottom layer $2 \cdot T_i \cdot H_1$ is determined by (4.59), where the terms on the rhs are the forcing by Ekman pumping (first term) and heat input (second term), a non-linear term expressing the advection of interface height anomalies (third term), the bottom pressure torque (forth term), and a vorticity sink due to diffusion of the interface height and horizontal friction (last term). (4.60) to (4.63) determine the time changes of the standing eddy components of the depth integrated flow and the flow relative to the bottom layer. On the rhs of these equations are terms representing the advection of total potential vorticity in terms of planetary vorticity, relative vorticity, or interface height, the bottom pressure torque expressed in terms of the mean bottom flow times topography height, and vorticity sinks due to diffusion of the interface height and horizontal friction. In the steady state the forcing by Ekman pumping and heat input in (4.58) and (4.59) is either balanced by a potential vorticity sink due to friction and interface height diffusion, or by the bottom pressure torque.

A balance between the zonally integrated vorticity input by Ekman pumping and the removal of vorticity by the zonally integrated bottom pressure torque is equivalent to a balance between the zonally integrated input of zonal momentum by wind stress and a momentum sink due to the zonally integrated bottom form stress (Hughes, 2000). Thus in the rest of this chapter, the zonal momentum balance is sometimes used instead of the vorticity balance.

A balance between Ekman pumping and bottom pressure torque requires a standing eddy bottom flow. This can be achieved through the bottom pressure torque terms in (4.60) and (4.61). The mean bottom flow excites a standing eddy bottom flow through the bottom pressure torque. The standing eddy bottom flow in turn decelerates the mean flow. With the advection of relative and planetary vorticity a transfer between the standing eddy components $F_{e,c}$ and $F_{e,s}$ as well as between $F_{i,c}$ and $F_{i,s}$ is possible, which can modify the balances.

The system of equations (4.58) to (4.63) is similar to the one obtained in Völker (1995, 1999). Especially the decision of using blocked geostrophic contours did not result in qualitatively different terms in the set of equations. In order to really discriminate between blocked and unblocked geostrophic contours, higher order Fourier modes would have to be included. Thus, the most important differences to the Völkers model are the inclusion of horizontal friction instead of vertical friction, the inclusion of relative vorticity advection, and the inclusion of a heat source. The interfacial friction used in Völker (1995, 1999) and the isopycnal height diffusion used here turned out to be equivalent in the low-order representation.

4.3 Model results and bifurcation analysis

The number of the degrees of freedom of the low-order model is small enough to make it accessible to the analysis methods of the dynamical system theory. In this section the software package CONTENT (see Kuznetsov (1998)) is used to study the dynamical properties of the model.

CONTENT is able to find the steady states (fixed points) of a low dimensional system of autonomous ordinary differential equations and can follow the changes of a steady state (fixed point) with a continuous variations of a control parameter. (For more details and numerical techniques see Kuznetsov (1998) and also Dijkstra (2000).) Various useful informations can be obtained from CONTENT (or the theory of dynamical systems in general).

For example, the stability of steady states can be analysed: A system of autonomous ordinary differential equations can be linearized around any fixed point and the response of the system to a small perturbation from a fixed point can then be expressed as an eigenvalue problem:

$$\mathcal{J}\vec{y}_n = \sigma_n \vec{y}_n \tag{4.64}$$

where $\mathcal{J}$ is the Jacobian matrix (see e.g., Dijkstra (2000), pages 62 f. and 67 ff.), $\vec{y}_n$ the n-th eigenvector of perturbations, and σ_n the n-th eigenvalue. If the real parts of all eigenvalues are negative, the fixed point is called linearly stable and the system converges back towards the fixed point after an infinitely small perturbation. If at least one eigenvalue is positive the fixed point is called unstable and an infinitely small perturbation may grow and the system may diverge away from that fixed point.

Further useful informations can be gained from the analysis of bifurcation points. At bifurcation points at least one eigenvalue of the Jacobian matrix crosses the imaginary axis as parameters are changed and the dynamical system ungoes qualitative changes. Two types of bifurcation points will be mentioned throughout the following discussion: Limit points and Hopf bifurcations. At a limit point the number of fixed points changes with a parameter change. One stable and one unstable branch of fixed points merges at the limit point and beyond the limit point the number of fixed points is reduced by two. At a Hopf bifurcation the number of fixed points does not change, but a fixed point changes its stability characteristics and an additional, periodic solution of the eigenvalue problem (4.64) exists at the Hopf bifurcation.

In the following subsections the dynamics of the low-order model was analysed by starting with a suitable set of parameter values, and using CONTENT to find a steady state of the low-order model and to follow the changes of the steady state with a variation of a parameter under consideration. The focus is on the changes in the steady state with a variation of the horizontal eddy viscosity, but the sensitivity to forcing variations and other parameters is studied as well. The most general results of this section are compared with the numerical 3-D experiments of chapter 3.

H_1	$=$	1000	m	D	$=$	1000	km	f_0	$=$	$-1 \cdot 10^{-4}$	s^{-1}
H_2	$=$	3000	m	L	$=$	4000	km	β	$=$	$1 \cdot 10^{-11}$	$\mathrm{m}^{-1}\mathrm{s}^{-1}$
B	$=$	2000	m	R	$=$	20	km	κ	$=$	1	$\mathrm{m}^2\mathrm{s}^{-1}$
w_0	$=$	$6.13 \cdot 10^{-6}$	$\mathrm{m\,s}^{-1}$	Q_0	$=$	0	$\mathrm{W\,m}^{-3}$	A	$\leq$	$1 \cdot 10^5$	$\mathrm{m}^2\mathrm{s}^{-1}$
α/c_p	$=$	$3 \cdot 10^{-8}$	$\mathrm{kg\,J}^{-1}\mathrm{m}^{-3}$	ρ_0	$=$	1024	$\mathrm{kg\,m}^{-3}$	g	$=$	9.81	$\mathrm{m\,s}^{-2}$

Table 4.1: Parameter values for the low-order model (4.45) to (4.50). The corresponding parameters of the dimension-free form of the model are given in table 4.2. Here, w_0 is chosen such that the maximum of the eastward wind stress in the center of the channel is $0.1\,\mathrm{N\,m}^{-2}$ according to (4.30).

$\widetilde{R}$	$=$	$6.28 \cdot 10^{-2}$	$\widetilde{D}$	$=$	$7.96 \cdot 10^{-2}$	$\widetilde{B}$	$=$	$1.57 \cdot 10^{\ 0}$	h	$=$	$0.25 \cdot 10^{\ 0}$
$\widetilde{\beta}$	$=$	$1.00 \cdot 10^{-1}$	E_H	$\leq$	$9.86 \cdot 10^{-3}$	E_κ	$=$	$9.86 \cdot 10^{-8}$	$\widetilde{w}_0$	$=$	$4.81 \cdot 10^{-5}$
$\widetilde{Q}_0$	$=$	$0.00 \cdot 10^{\ 0}$	$\widetilde{g}$	$=$	$2.94 \cdot 10^{\ 0}$						

Table 4.2: Dimensionless parameter values for the low-order model (4.58) to (4.63).

4.3.1 Sensitivity to horizontal friction

Figure 4.1 shows the steady state values of the low-order model (4.45) to (4.50) against the horizontal eddy viscosity A, where the other parameters are taken from table 4.1. The solid lines indicates stable steady states and the dotted lines unstable ones. The upper left panel shows the total depth integrated channel transport. With a horizontal viscosity A of $1 \cdot 10^5\,\mathrm{m}^2\mathrm{s}^{-1}$ the magnitude of this transport is 74 Sv. If A is then reduced, the channel transport increases as $T_e \propto A^{-1}$. From (4.45) it is evident, that this increase in the transport is consistent to a balance between wind forcing and horizontal friction. At $A = 4.17 \cdot 10^4\,\mathrm{m}^2\mathrm{s}^{-1}$ the curve $T_e \propto A^{-1}$ arrives at a limit point and the channel transport reaches 176 Sv. Beyond this point a further decrease of A does not result in an increase of the transport. The branch $T_e \propto A^{-1}$ does only exist for $A \geq 4.17 \cdot 10^4\,\mathrm{m}^2\mathrm{s}^{-1}$, thus for a Ekman number $E_H \geq 4.11 \cdot 10^{-3}$. A second stable branch exists between the Hopf bifurcation at $A = 3.71 \cdot 10^3\,\mathrm{m}^2\mathrm{s}^{-1}$ ($E_H = 3.66 \cdot 10^{-4}$) with a transport of 22 Sv, and second limit point at $A = 5.89 \cdot 10^4\,\mathrm{m}^2\mathrm{s}^{-1}$ ($E_H = 5.81 \cdot 10^{-3}$) with a transport of 91 Sv. The two limit points are connected by a third, unstable branch. However, being unstable, this last branch is usually not realized in forward integrations nor in the physical system. To the left of the Hopf bifurcation ($A < 3.71 \cdot 10^3\,\mathrm{m}^2\mathrm{s}^{-1}$) a further branch with unstable steady states completes the bifurcation diagram.

So, if the horizontal viscosity A is reduced from $A = 1 \cdot 10^5\,\mathrm{m}^2\mathrm{s}^{-1}$ to values smaller than $A = 4.17 \cdot 10^4\,\mathrm{m}^2\mathrm{s}^{-1}$ the system must jump from the frictionally balanced branch

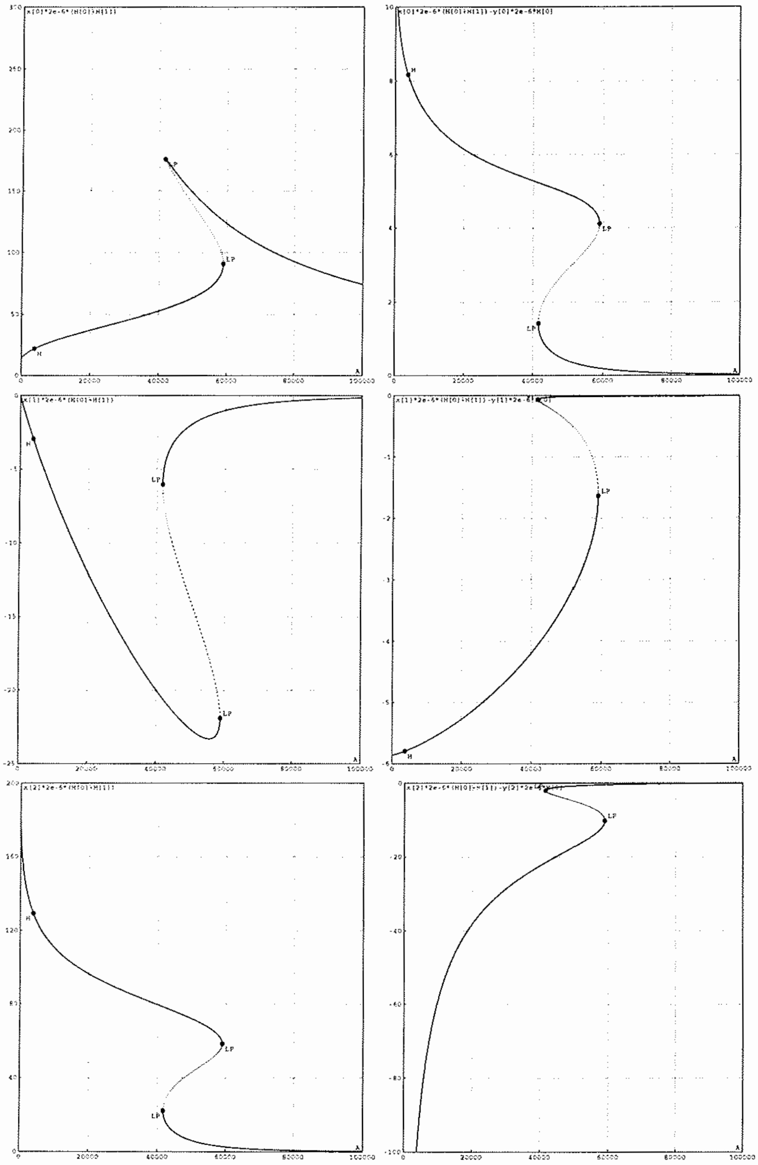

Figure 4.1: Plot of the steady state values (in Sv) of the low-order model (4.45) to (4.50) against the horizontal eddy viscosity A (in m^2/s) with parameters taken from table 4.1. Upper left: Total depth integrated channel transport $2 \cdot T_e \cdot H$; Upper right: Channel transport of the bottom flow $2 \cdot (T_e \cdot H - T_i \cdot H_1)$; Middle left: Standing eddy component of the depth integrated flow $2 \cdot F_{e,c} \cdot H$; Middle right: Standing eddy component of the bottom flow $2 \cdot (F_{e,c} \cdot H - F_{i,c} \cdot H_1)$; Lower left: $2 \cdot F_{e,s} \cdot H$; Lower right: $2 \cdot (F_{e,s} \cdot H - F_{i,s} \cdot H_1)$. Solid lines indicate stable steady states, dotted lines unstable steady states. Points labeled with "LP" mark limit points and points labeled with "H" Hopf bifurcations. (Note: Here, the steady states to the left of the Hopf bifurcation are unstable. But because of the high number of points the line appears to be solid. The same applies to figures 4.3 to 4.9.)

with $T_e \propto A^{-1}$ to the second stable branch with substantially lower transport values. At $A = 1 \cdot 10^4 \mathrm{m^2 s^{-1}}$ ($E_H = 9.86 \cdot 10^{-4}$) the channel transport is reduced to 29 Sv. From (4.45) it can be seen that if the frictional sink is not efficient enough to balance the wind forcing, bottom pressure torque must come into play for a steady state to be realized. The middle right panel of figure 4.1 shows the projection of the bottom flow on the $\mathcal{F}^c_{1,1}$ mode. This mode is relevant for establishing a bottom pressure torque that opposes the vorticity input by Ekman pumping in (4.45). On the first stable, frictionally balanced, branch with $A \geq 4.17 \cdot 10^4 \mathrm{m^2 s^{-1}}$ the projection of the bottom flow on the $\mathcal{F}^c_{1,1}$ mode is almost zero and so is the bottom pressure torque in (4.45). But, on the second stable branch the bottom flow (projected on $\mathcal{F}^c_{1,1}$) has a value of -1.64 Sv at the limit point at $A = 5.89 \cdot 10^4 \mathrm{m^2 s^{-1}}$, increases its negative value with a decreased horizontal viscosity A, and reaches a value of -5.80 Sv at the Hopf bifurcation at $A = 3.71 \cdot 10^3 \mathrm{m^2 s^{-1}}$. (4.45) implies that the vorticity input by Ekman pumping is completely balanced by bottom pressure torque if the projection of the bottom flow on the $\mathcal{F}^c_{1,1}$ mode is $2 \cdot (F_{e,c} \cdot H - F_{i,c} \cdot H_1) = -(3HDLw_0)/(\pi B) = -5.86\,\mathrm{Sv}$. Thus, at the limit point 28% of the vorticity input by the wind forcing is balanced by the bottom pressure torque. At the Hopf bifurcation 99% is balanced by the bottom pressure torque. The system shifted from a frictionally balanced state to a steady state which is balanced through the presence of bottom pressure.

The $\mathcal{F}^c_{1,1}$ mode is coupled to the $\mathcal{F}^s_{1,1}$ mode through advection with the mean flow and through the propagation of Rossby waves; see (4.47) to (4.50). These modes are damped by the action of horizontal friction and interface height diffusion. To set these modes in motion a mean bottom flow $F_{e,c} - H_1/H\, F_{i,c}$ is required. Through the bottom pressure torque term in (4.47) and (4.50) vorticity is then transferred to the $\mathcal{F}^c_{1,1}$ mode. In the upper right panel of figure 4.1 the mean bottom flow is shown. For the frictionally balanced branch, this flow is weak and not much vorticity is transferred to the $\mathcal{F}^c_{1,1}$ mode. On the second stable branch the mean bottom flow is stronger and the $\mathcal{F}^c_{1,1}$ mode is excited. The lower two panels of the figure show, that the $\mathcal{F}^s_{1,1}$ mode gets excited, too, and even achieves transport values much greater than that of the $\mathcal{F}^c_{1,1}$ mode. With decreasing A the $\mathcal{F}^s_{1,1}$ mode becomes stronger and stronger and makes the low-order truncation more and more questionable, since one would then expect the higher Fourier modes with $n + m > 2$ to be excited, too.

Considering the configurations sin1 and sin2 of chapter 3 as more or less comparable to the present low-order model one may now refer to table 3.4 of chapter 3. For both configurations one observes a channel transport that first increases and then substantially decreases with a reduction of the horizontal eddy viscosity. Also evident in table 3.4 is a transition from a zonal momentum balance between horizontal friction and wind stress to a balance between bottom form drag and wind stress. Qualitatively, these features are well reproduced by the low-order model. Also the transport values of the low-order model seem to be reasonable.

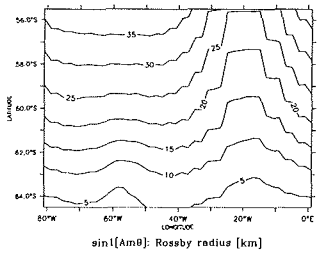

Figure 4.2: Rossby radius $R(x, y)$ for configuration sin1 of chapter 3 with a horizontal eddy viscosity of $10^5\,\mathrm{m^2s^{-1}}$.

eddy viscosity	sin1	sin2	C2a
$10^5\,\mathrm{m^2s^{-1}}$	20.3 km	33.6 km	23.8 km
$10^4\,\mathrm{m^2s^{-1}}$	17.9 km	32.1 km	21.9 km
$10^3\,\mathrm{m^2s^{-1}}$	17.4 km	29.3 km	20.9 km

Table 4.3: Horizontally averaged Rossby radius $\bar{R}$ for the configurations sin1, sin2, and C2a of chapter 3 with different horizontal eddy viscosities.

4.3.2 The determinants and effects of the Rossby radius

A central parameter of the low-order model is the first baroclinic Rossby radius R. With (4.16) it could be seen as a measure of the vertical stratification of the channel. In quasi-geostrophic models the background stratification is considered as being horizontally constant and constant in time. Small deviations from the background stratification are implemented through small vertical excursions of the interface heights. As quasi-geostrophic models can not explicitly resolve the processes that set up the background stratification, they handle it as externally given.

In contrast to the quasi-geostrophic low-order model, the 3-D model used in the chapters 2 and 3 does produce its own vertical stratification. From the results of this model the first baroclinic Rossby radius R can be approximately calculated from:

$$R \approx \frac{1}{f} \int_{-H}^{0} \sqrt{\frac{g}{\rho_0} \left(-\frac{\partial \rho}{\partial z} \right)} \, \mathrm{d}z \tag{4.65}$$

Figure 4.2 shows the horizontal distribution of R for the configurations sin1 of chapter 3 with a horizontal eddy viscosity $A = 10^5\,\mathrm{m^2s^{-1}}$, and table 4.3 gives the horizontally averaged values of the Rossby radius for the configurations sin1, sin2, and C2a of chapter 3 with the horizontal eddy viscosities $A = 10^5$, 10^4, and $10^3\,\mathrm{m^2s^{-1}}$.

From figure 4.2 a clear meridional gradient of the Rossby radius R can be seen. Table 4.3 shows for all three configurations a decreasing R with a decreasing A. Thus the Rossby radius is not constant as assumed in the low-order model and it does depend on the other parameters as well.

The formation of the vertical stratification by buoyancy forcing, the wind induced Eulerian overturning circulation, and eddy processes as well as the effect of a changed stratification on the transport of a circumpolar channel is discussed e.g., in section 2.3 of chapter 2, in Marshall et al. (2002), Karsten et al. (2002), and Karsten & Marshall

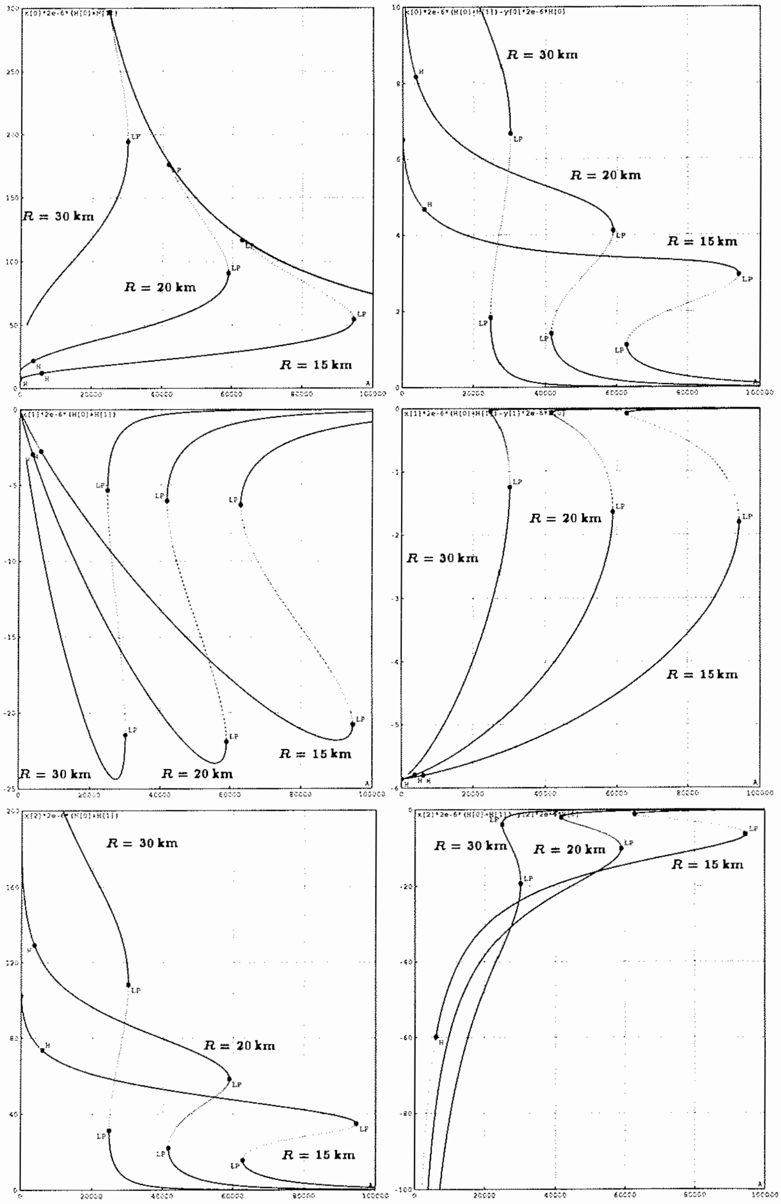

Figure 4.3: Same as figure 4.1, but for different Rossby radii $R = 15$, 20, and 30 km.

(2002). There, the channel transport is determined by the meridional gradient of an e-folding depth which expresses the vertical stratification. To a very crude degree such processes are represented in the low-order model through processes determining the meridional gradient of the interface height, which is by (4.6) connected with the baroclinic channel transport. However, since the mean background stratification is taken to be constant in the low-order model important feedbacks may have been disregarded.

To test the sensitivity of the low-order model to a variation of R, the bifurcation diagrams are drawn in figure 4.3 for $R = 15$, 20, and 30 km. The most general structure of the bifurcation diagram does not change very much, but with a smaller Rossby radius R the limit points lie further towards high values of the horizontal eddy viscosity A. Thus, with a smaller Rossby radius the shift of the system from a frictionally balanced steady state to a steady state which is balanced through the bottom pressure occurs for higher values of the horizontal eddy viscosity A. The transport values for the frictionally balanced steady state at a given A do not change with a variation of R, but on the second stable branch, the channel transport decreases with a decrease of the Rossby radius R.

4.3.3 Forcing variations

Figure 4.4 shows the steady state values of the low-order model against the wind forcing. Starting with zero wind stress and increasing the eastward wind stress the vertically integrated mean channel transport increases linearly with the wind stress until a limit point is reached (see upper left panel). This branch is stable and frictionally balanced. The projection of the bottom flow on the $\mathcal{F}^c_{1,1}$ mode (middle right panel) then gives small values and thus the bottom pressure torque in (4.45) is small. If the wind stress is increased beyond this limit point the system must jump to a second stable branch with much smaller values for the channel transport. (Again the two stable branches are connected by an unstable branch between two limit points.) On this branch an increase of the wind stress does not lead to an increase of the channel transport but to an increase of the $\mathcal{F}^c_{1,1}$ mode of the bottom flow and thus of the bottom form drag that opposes the wind stress.

A channel transport which is not increasing with an increase of the eastward wind stress is contrary to the results of section 2.3 of chapter 2. There, the wind induced Eulerian overturning circulation modifies the vertical stratification in the northern part of the channel, such that the meridional density gradient and the channel transport is increased. As mentioned in the previous subsection, these processes are only poorly represented in the low-order model and the dependence of the channel transport on the wind forcing is thus not fully captured in the low-order model.

With a westward wind stress the steady state values of the vertically integrated mean channel transport increase linearly with the wind stress within the whole range

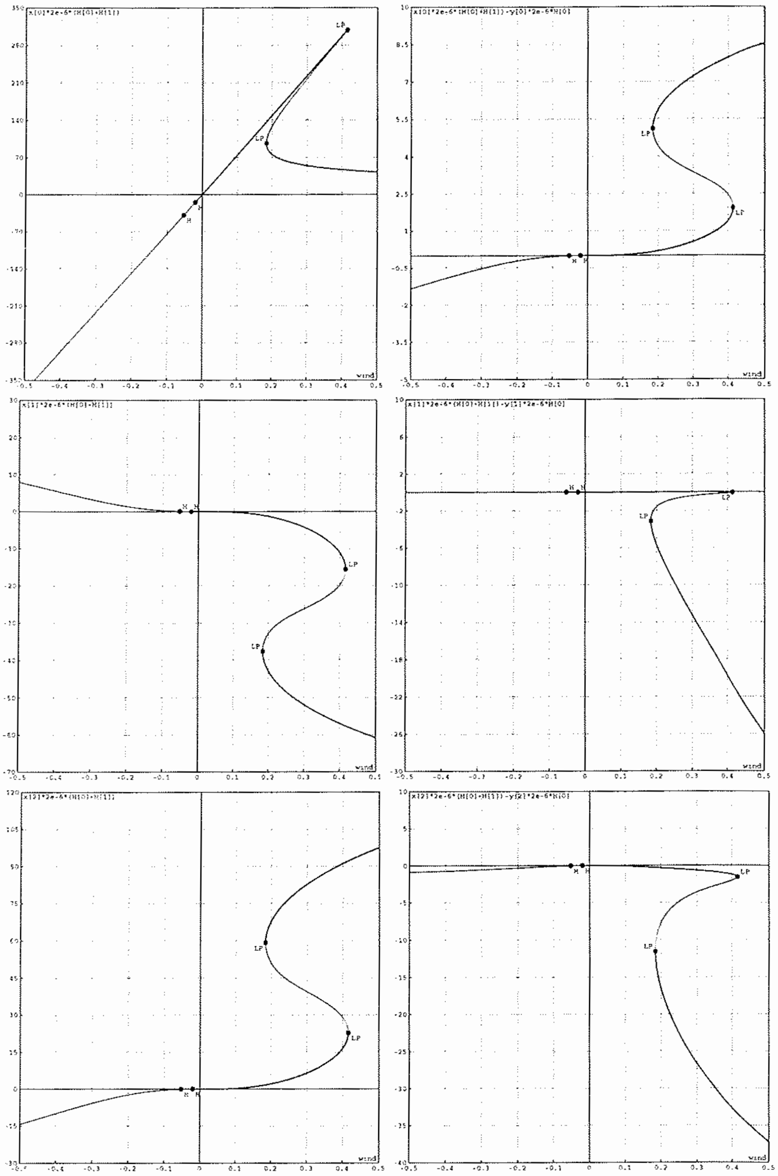

Figure 4.4: Plot of the steady state values (in Sv) of the low-order model against the maximum of the eastward wind stress (in $\mathrm{N\,m^{-2}}$) in accordance with (4.30). The horizontal eddy viscosity is set to $A = 10^5\,\mathrm{m^2 s^{-1}}$, and all other parameters are taken from table 4.1. The six panels that show different transport values are organized in the same way as in figure 4.1.

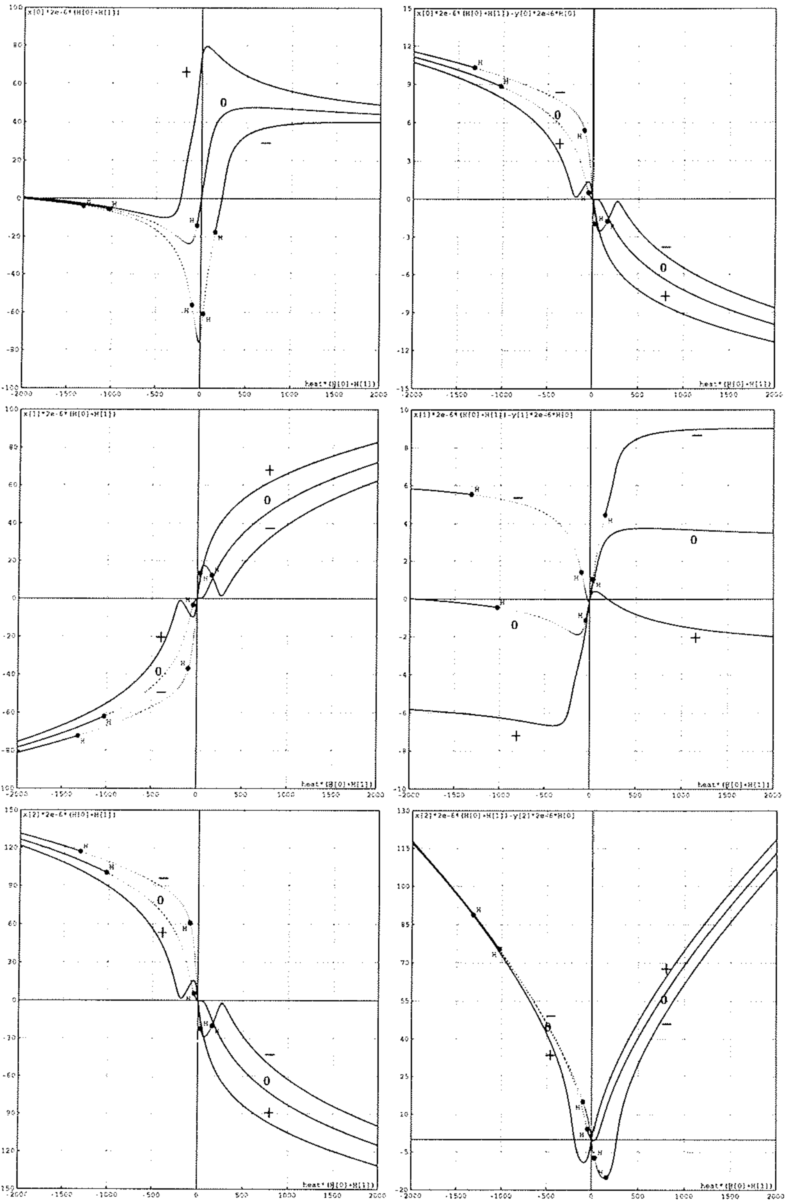

Figure 4.5: Plot of the steady state values (in Sv) of the low-order model against the surface heat flux (in W m^{-2}) with positive wind forcing as in figure 4.1 (curves labeled with "+"), no wind stress ("0"), and inversed wind stress ("-"). The horizontal eddy viscosity is set to $A = 10^5\,\mathrm{m^2s^{-1}}$, and all other parameters are taken from table 4.1. The six panels that show different transport values are organized in the same way as in figure 4.1.

considered. However, beyond the first Hopf bifurcation all of these steady states are unstable. If a westward wind stress is applied and thus a westward mean channel flow is induced, the advection with the mean flow and the propagation of long Rossby waves are both directed towards the west and the mechanism of topographic resonance can not work in the same way as sketched in the introduction of this chapter. This may be a possible explanation why a shift to a balance between the wind forcing and the bottom form drag is not observed for a westward wind stress.

In figure 4.5 the steady state values of the low-order model are plotted against the surface heat forcing ($Q \cdot H$). The bifurcation diagrams are drawn for positive wind forcing of the same kind as use in figure 4.1 (curves labeled with "+"), for the same wind forcing but directed towards the west ("-"), and for the case of no wind forcing ("0").

If one first considers the case of no wind forcing and increases the heat flux Q (starting from $Q = 0.0\,\mathrm{W\,m^{-2}}$) one observes an increasing eastward channel transport that reaches a maximum of around 50 Sv at a Q of around $500\,\mathrm{W\,m^{-2}}$ and then starts to decrease slightly. From the middle right panel of figure 4.5 it can be seen that the bottom pressure torque now acts to accelerate the eastward flow. For a steady state this must be balanced in (4.45) by horizontal friction. It is not straight forward to give an explanation for the decreasing channel transport for high values of Q. However, for a Q far beyond $100\,\mathrm{W\,m^{-2}}$ one moves outside the range which can be supported by observations. With negative values for Q one first observes an increasing westward mean transport with a maximum of around 25 Sv at a Q of around $100\,\mathrm{W\,m^{-2}}$ and then a clearly decreasing westward transport. Beyond $Q = -500\,\mathrm{W\,m^{-2}}$ the mean channel transport even gains positive values for an eastward transport. Again, it is difficult to give a physical explanation for this.

Considering the case of both, thermohaline as well as wind forcing the upper left panel for figure 4.5 shows a clear asymmetry in the magnitudes of the eastward and westward transport for positive and negative wind forcing, as soon as a finite heat forcing is added. The stronger the heat forcing the less significant the effects of the wind forcing on the channel transport. These two general statements are consistent to the conclusions drawn in chapter 2 - however, any more detailed or quantitative comparisons reveals substantial differences. Especially the feedbacks of the imposed forcing on the vertical stratification are important for a good representation of the dependence of the channel transport on the imposed forcing.

4.3.4 Sensitivity to other parameters

Figure 4.6 shows the steady state values of the low-order model against the horizontal eddy viscosity A, where different interface height diffusivities $\kappa = 1$, 10, 100, and $1000\,\mathrm{m^2s^{-2}}$ were used. The structure of a stable frictionally balanced branch, a limit point, an unstable branch, a second limit point, and a second stable branch is only

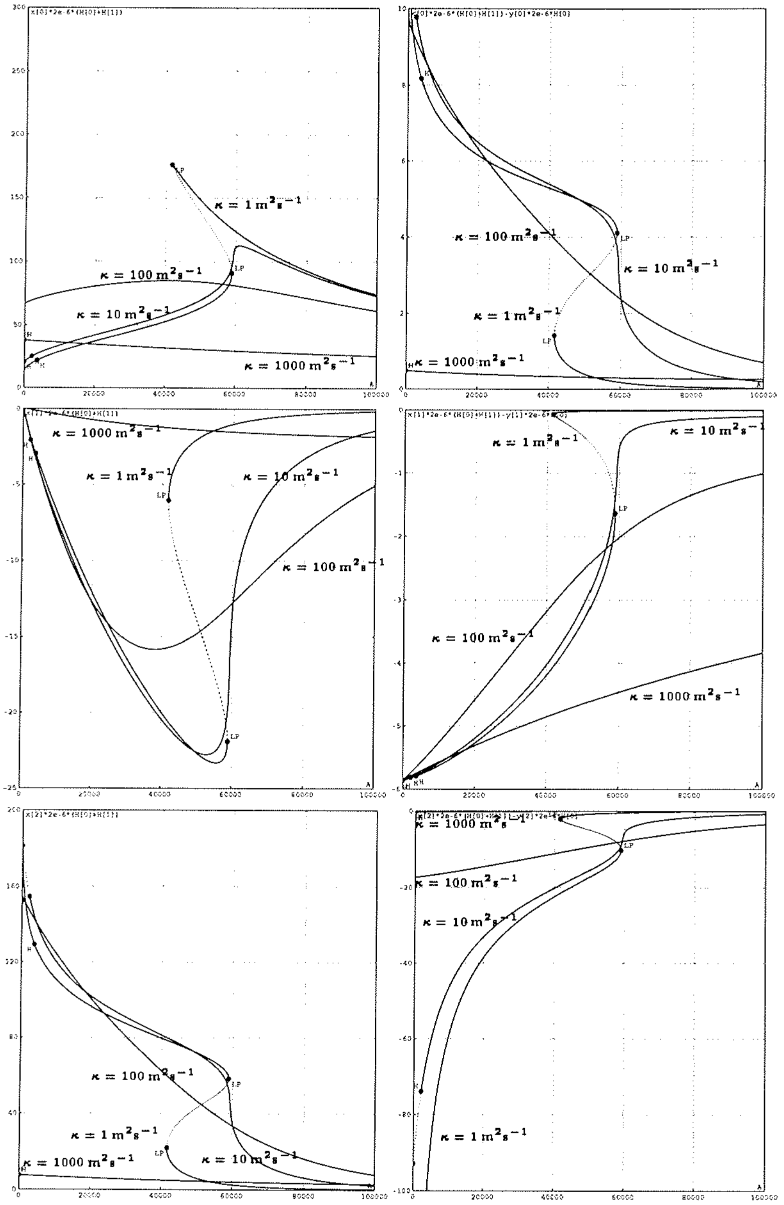

Figure 4.6: Same as figure 4.1, but for different interface height diffusivities $\kappa = 1$, 10, 100, and $1000\,\mathrm{m^2s^{-1}}$.

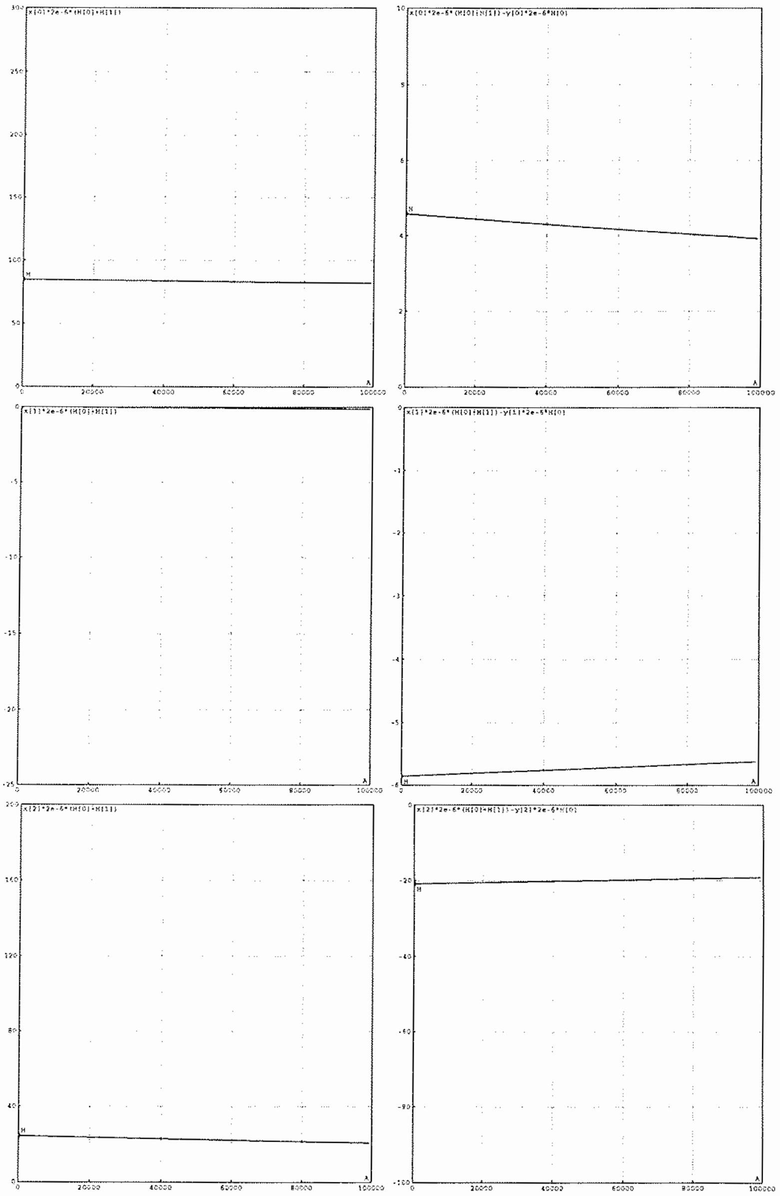

Figure 4.7: Same as figure 4.1, but with the interface height diffusivity increased to $\kappa = 1000\mathrm{m}^2\mathrm{s}^{-1}$ and the meridional channel extent to $D = 3000\,\mathrm{km}$.

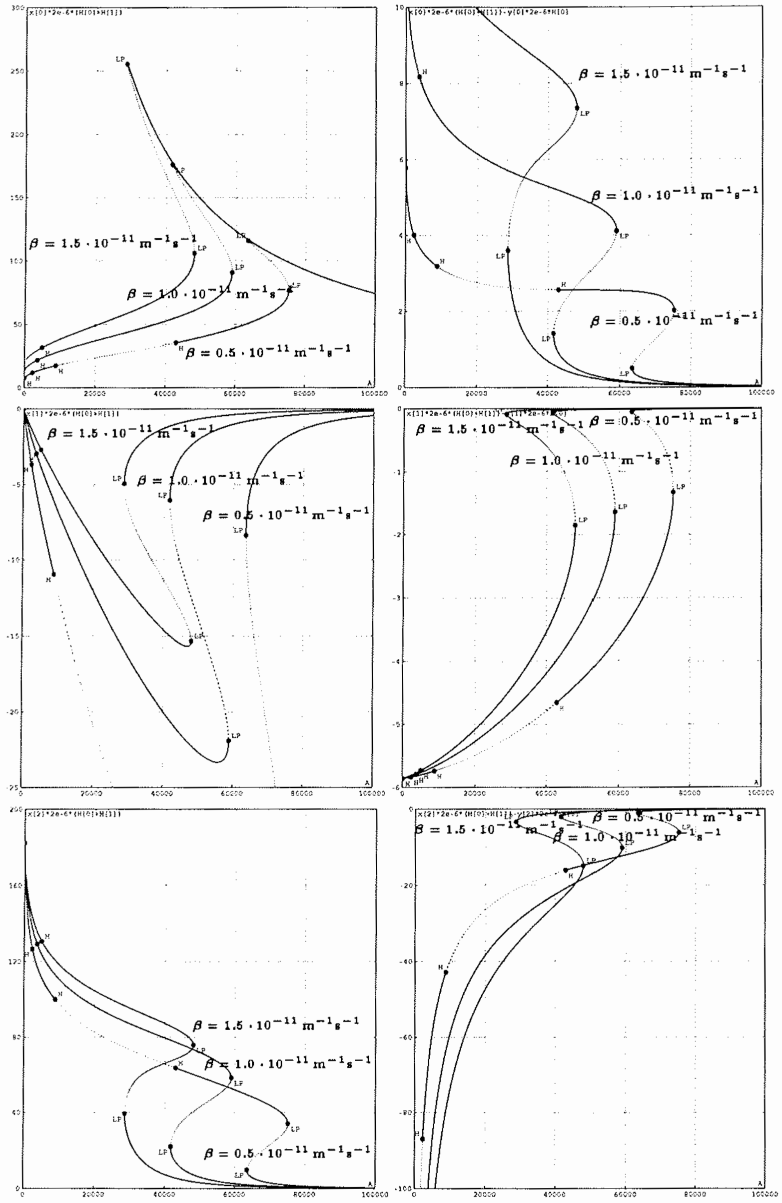

Figure 4.8: Same as figure 4.1, but for different meridional gradients of the planetary vorticity $\beta = 0.5$, 1.0, and $1.5 \cdot 10^{-11}\,\mathrm{m}^{-1}\mathrm{s}^{-1}$.

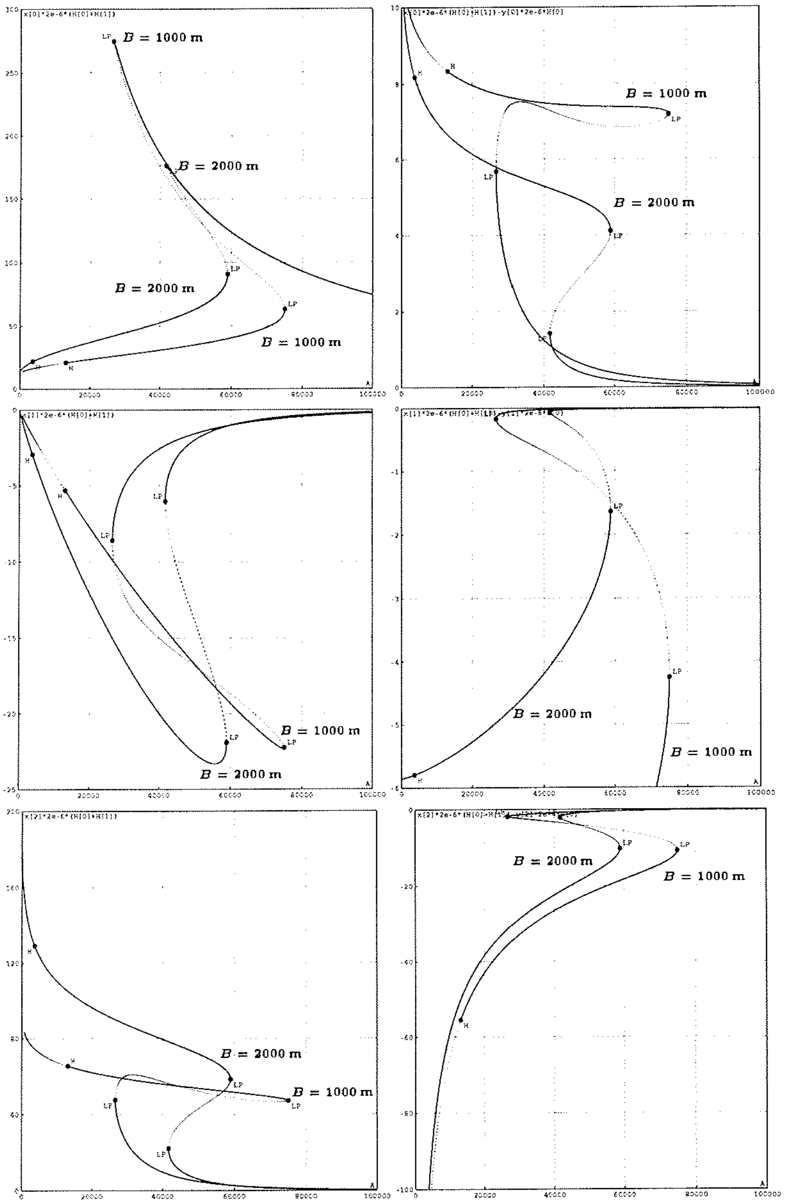

Figure 4.9: Same as figure 4.1, but for two different heights of the topographic obstacle, with $B = 1000\,\mathrm{m}$ and $B = 2000\,\mathrm{m}$.

present for $\kappa = 1\,\mathrm{m^2s^{-1}}$. With $\kappa = 10\,\mathrm{m^2s^{-1}}$ the system still clearly moves from a frictionally balanced steady state to a bottom pressure torque balanced steady state when A is decreased, but this occurs much more smoothly and without coming into a regime of multiple steady states. If κ is further increase to $100\,\mathrm{m^2s^{-1}}$ this tendency continues, and with $\kappa = 1000\,\mathrm{m^2s^{-1}}$ the system does not seem to be very sensitive to a change of A. For $\kappa = 1000\,\mathrm{m^2s^{-1}}$ the system seems to be balanced by bottom pressure torque for the whole range of $0 \leq A \leq 10^5\,\mathrm{m^2s^{-1}}$ and all components (standing eddy as well as mean components) are clearly damped by the action of interface height diffusion.

In chapter 3 it was speculated that the differences in the sensitivity of the flow of the configurations C2a and rec B to variations of the horizontal eddy viscosity may be partly due to the different meridional extent of the two channel configurations plus the difference in the values of the horizontal eddy diffusivity. By increasing the meridional width the frictional momentum sink through the horizontal walls to the north and south of the channel becomes less efficient, and by increasing the horizontal diffusivity the standing eddies may be damped away more strongly. In figure 4.7 this idea is tested with the low-order model. There, the meridional channel width was increased to $D = 3000\,\mathrm{km}$ and the interface height diffusivity to $\kappa = 1000\,\mathrm{m^2s^{-1}}$. In figure 4.7 the system seems to be rather insensitive to a variation of A. The system is in an approximate balance between the vorticity input by Ekman pumping and a vorticity sink by bottom pressure torque for the whole range of $0 \leq A \leq 10^5\,\mathrm{m^2s^{-1}}$, and the standing eddies are substantially reduced in comparison to figure 4.1. Comparing the bottom pressure torque term and the horizontal friction term in the barotropic vorticity balance of the mean flow (4.45) shows that by multiplying the magnitude of D by three, the bottom pressure torque term gains in comparison to the horizontal friction term by a factor of $3^3 = 27$. The system is then much less sensitive to the horizontal eddy viscosity A. This is consistent to the ideas of chapter 3.

The sensitivity of the steady state values of the low-order model to a variation of the meridional gradient of the planetary vorticity β can be seen from figure 4.8. The most general shape of the bifurcation diagram does not change very much. With an increased β the frictionally balanced branch extends further towards low values of the horizontal eddy viscosity A. The mean depth integrated channel transport on the branch with a balance by bottom pressure increases as well as the eddy modes $\mathcal{F}^c_{1,1}$ and $\mathcal{F}^s_{1,1}$ of the depth integrated transport.

Finally, figure 4.9 shows the steady state values against A for two different topography heights B. If B is decreased from 2000 m to 1000 m the range of A where three steady states coexist increases. The system can stay longer on the frictionally balanced branch if the horizontal eddy viscosity is reduced (starting with $A = 10^5\,\mathrm{m^2s^{-1}}$) and it can also stay longer on the bottom pressure torque balanced branch if A is increased (starting from low values). As B is reduced by a factor of one half the projection of the bottom flow on the $\mathcal{F}^c_{1,1}$ mode that is necessary to balance the wind forcing by bottom pressure torque is doubled. Consistent to this the $\mathcal{F}^{c}_{1,1}$ mode of the bottom flow increases in strength on the bottom pressure torque balanced branch.

4.4 Summary

In this chapter a low-order model is used as a heuristic tool to gain some general understanding of the dynamics of the channel. It is able to reproduce a channel transport that is first increasing and then decreasing with a decrease ot the horizontal eddy viscosity. A shift from a balance between wind forcing and friction to a balance between wind forcing and bottom pressure torque / bottom form drag was shown. The dynamical mechanism that is proposed on the basis of the low-order model is the following:

- The mean flow is accelerated by the action of wind stress. Due to the presence of the topographic obstacle the mean flow excites Rossby waves that eventually become trapped as standing eddies. These standing eddies produce a bottom form drag that opposes the wind forcing.
- Horizontal friction damps the standing eddy components of the flow. For high enough values of the horizontal eddy viscosity the damping mechanism becomes efficient enough that the standing eddies become too weak to produce a bottom form drag that could balance the wind stress. In this case the mean flow is further accelerated until the wind forcing is balanced by horizontal friction.

It is not clear whether the multiplicity of steady states that is observed with the low-order model does also exist for the 3-D primitive equation model of the previous chapters. There, the transition from a frictionally balance steady state to a steady state balanced through bottom pressure may well happen much more smoothly than the low-order model suggests and the 3-D model must not necessarily pass a regime with multiple steady states. With the low-order model such a smooth transition without multiplicity of steady states is achieved if the interface height diffusivity (thus the parameterized mixing of mesoscale eddies) is increased.

One major weakness of the quasi-geostrophic low-order model is the inability to produce its own background stratification in response to the impose wind and buoyancy forcing. This leads to a rather inaccurate representation of the dependence of the channel transport on the imposed forcing. Another weakness is that the low-order model can not resolve any kind of boundary layer structure. Thus it may not be used to explain the transition to the double gyre circulation observed in chapter 3 for the lowest values of the horizontal eddy viscosity studied.

Chapter 5

Summary and conclusion

In this thesis the leading order dynamical balances of zonally periodic channels with vertical stratification, coarse horizontal resolution, and blocked geostrophic contours have been studied. These are:

- Local vorticity balance of the depth averaged flow: One consequence of the vorticity equation of the depth averaged flow is that the transport across a meridional ridge blocking the geostrophic contours of a stratified, zonally periodic channel is to leading order determined by a balance between barotropic advection of planetary vorticity and the joint effect of baroclinicity and relief (JEBAR) at that meridional ridge.

- Local balance of the meridional momentum: It was argued that under certain conditions (one of them is that the channel transport is more or less zonal) the above implies a leading order meridional momentum balance between the meridional gradient of the baroclinic potential energy and the zonal, depth integrated transport (times the Coriolis frequency). This was expressed by (2.11) which is the central result of section 2.2 whose validity is discussed throughout the subsequent subsections.

- Zonally integrated balance of the tracer fluxes and transports: With (2.11) the processes that determine the hydrography become important in determining the channel transport, too. The most important of these are a) the surface buoyancy flux which results in a vertical stratification and meridional density gradients, b) convergence of Ekman transport that brings the density signal to larger depths, and c) the meso-scale eddies that transport buoyancy downgradient. Using a very simple representation of the meso-scale eddy fluxes (i.e. horizontal eddy diffusion) an idealized analytical model of the channel transport was developed.

- Zonally integrated balance of the zonal momentum: In contrast to the local meridional momentum balance which is approximately geostrophic for all numerical experiments considered in this thesis, the zonally integrated zonal momentum balance turned out to be sensitive to the horizontal eddy viscosity within the parameter range studied. Depending on the model configuration and the value of eddy viscosity the zonally integrated zonal wind stress was balanced by horizontal friction or by bottom form drag, where the later is currently generally acknowledged to be the term balancing the wind stress in the ACC - see e.g., Stevens & Ivchenko (1997). However, a frictional balance of zonal momentum is known to be typical for coarse resolution models of the ACC - see e.g., the discussion in Wolff et al. (1991).

- Volume integrated kinetic energy balance: As the input of zonal momentum by wind stress may be balanced by friction or by bottom form drag, the volume integrated input of kinetic energy by wind forcing may be taken up by friction or by the production of potential energy. Depending on the model configuration and the eddy viscosity both balances were observed in chapter 3. A balance between wind forcing and buoyancy forcing is currently considered as being typical for the Southern Ocean - see Ivchenko et al. (1997).

- Zonally integrated vorticity balance of the depth integrated flow: Following Hughes (2000) a zonally integrated balance of the zonal wind stress and bottom form drag implies a zonally integrated balance of the vorticity input by Ekman pumping and a vorticity sink by bottom pressure torque. On the other hand, if the wind stress is to leading order balanced by friction, the vorticity input is to leading order balanced by friction, too.

The sensitivity of the flow and the dynamical balances to a variation of the horizontal eddy viscosity was investigated for the zonally periodic channel with topography and the periodically connected rectangular basin.

Considering the first configuration with a horizontal viscosity of $10^5\,\mathrm{m}^2\mathrm{s}^{-1}$, the channel flow is more or less zonal and the zonal wind stress is mainly balanced by friction. Decreasing the horizontal viscosity by one or two orders of magnitudes, the zonal momentum balance shifts to a leading order balance between wind stress and bottom form drag. At the same time strong meanders developed and the total channel transport is substantially reduced. The meanders induce a downgradient meridional buoyancy transport and thus tend to reduce the meridional density gradient as well as the zonal transport.

With respect to the second configuration (i.e. the rectangular basin) the flow is not very sensitive to a variation of the horizontal viscosity (within the parameter range studied). The flow was more or less zonal and the zonal momentum balance was to leading order geostrophic for all horizontal viscosities used. Since the meridional extent of the rectangular basin is about three times the meridional extent of the zonally periodic channel the efficiency of the frictional sink is smaller by more than one order of magnitude and is thus much less relevant in the rectangular basin configuration.

With the low-oder model it is possible to study the above shift from a frictionally balanced flow to a geostrophically balanced flow in a very simple form. With low horizontal viscosities, standing eddies are induced by the mean flow crossing the topography. Theses standing eddies establish a bottom pressure torque that opposes the imposed wind forcing. With high horizontal viscosities, the standing eddies are damped and the flow is accelerated until the wind forcing is balanced by friction.

This study of the dynamics of a coarse resolution channel model of the Southern Ocean leads to following recommendations for climate models:

- The horizontal viscosity must be low enough to reproduce the correct dynamics where the zonally integrated zonal wind stress at the latitudes of the Drake Passage are balanced to leading order by the bottom form stress and not by friction. This is not always the case in coarse resolution models.

- The most important feature that should be realized by the bottom topography is the existence of blocked geostrophic contours (i.e. f/H-contours) the ACC has to cross. The dynamics are substantially altered by the presence of blocked geostrophic contours.

- If blocked geostrophic contours are present the ACC transport is to leading order determined by the density field. Thus, all processes that may change the density field are important for setting up the ACC. If the model produces the right water masses and the right density field the model should produce more or less the right ACC, too. Here, two critical points of global ocean models are the formation of AABW and the parameterization of meso-scale eddies. Furthermore the ACC is not only influenced by water masses formed within the Southern Ocean but also by water masses formed elsewhere and being advected into the Southern Ocean like the NADW (see e.g., Goodman (1998) and Brix & Gerdes (2002)).

Acknowledgements

The Alfred Wegener Institute for Polar and Marine Research (AWI) in Bremerhaven provided the organizational framework for my Ph.D. work. I benefited a lot from many helpful discussions with my supervisors and colleagues at the institute, from the good computing facilities and the good support by the computing center, as well as from various opportunities to travel to conferences, summer schools and workshops.

I thank Prof. Dr. Dirk J. Olbers for being a critical supervisor, for sharing his expertise in Southern Ocean dynamics, and for his good support during my Ph.D. work at AWI. I thank Prof. Dr. Jörg-Olaf Wolff for accepting to be the second referee, as well as Prof. Dr. Peter Lemke, Prof. Dr. Jörn Bleck-Neuhaus, Dr. André Paul, and Jenny Brauch for being available for my disputation.

Special thanks are due to my supervisor Dr. Rüdiger Gerdes who supported me during the whole period at AWI by frequent helpful discussions, by contributing his experience in ocean modeling, and by having good advise concerning any questions related to my Ph.D. work at any time I asked for it.

I had the luck to have with Dr. Vladimir Ivchenko a further expert of Southern Ocean dynamics sitting just next to me in the office. His critical discussions, his suggestions of useful analysis methods, and his comments on previous versions of the text were of great help in improving the thesis.

I thank the Group Rüdiger Gerdes and friends - MAD (these are Jenny Brauch, Dr. Holger Brix, Christian Dieterich, Dr. Rüdiger Gerdes, Dr. Jörg Hurka, Dr. Michael Karcher, Dr. Frank Kauker, Jan Lieser, Dr. Katrin Meissner, Cornelia Koeberle, and Matthias Prange) for a friendly working atmosphere and for their help on all kinds of problems.

I thank Prof. Dr. Henk Dijkstra for his invitation to a stimulating week of work at the Instituut voor Marien en Atmosferisch Onderzoek Utrecht (IMAU) and his friendly support on bifurcation analysis. I thank Dr. Christoph Völker for kindly providing his Maple-scripts for his low-order model and Sven Harig for solving accommodation problems during the final period of my work.

Bibliography

Anderson, D.L.T., and A.E. Gill, 1975: Spin-up of a stratified ocean, with application to upwelling. *Deep-Sea Res.*, **22**, 583-596.

Anderson, R.F., Z. Chase, M.Q. Fleischer, and J. Sachs, 2002: The Southern Ocean's biological pump during the last glacial maximum. *Deep Sea Res. II*, **49**, 1909-1938.

Andrews, D.G., and M.E. McIntyre, 1976: Planetary waves in horizontal and vertical shear: The generalized Eliassen-Palm relation and the zonal mean acceleration. *J. Atmos. Sci.*, **33**, 2031-2048.

Baker, D.J., 1982: A note on Sverdrup balance in the Southern Ocean. *J. Marine Res.*, **40** (Suppl.), 21-26.

Barthelet, P., S. Bony, P. Braconnot, A. Braun, D. Cariolle, E. Cohen-Solal, J.-L. Dufresne, P. Delecluse, M. Déqué, L. Fairhead, M.-A. Filiberti, M. Forichon, J.Y. Grandpeox, E. Guilyardi, M.-N. Houssais, M. Imbard, H. LeTreut, C. Lévy, Z.-X. Li, G. Madec, P. Marquet, O. Marti, S. Planton, L. Terray, O. Thual, and S. Valecke, 1998a: Simulations couplées globales de changements climatiques associés à une augmentation de la terre et des planètes. 326, 677-684 (in French with English summary).

Barthelet, P., L. Terray, and S. Valcke, 1998b: Transient CO_2 experiment using the ARPEGE/OPAICE nonflux corrected coupled model. *Geophys. Res. Lett.*, **25**, 2277-2280.

Best, S.E., V.O. Ivchenko, K.J. Richards, R.D. Smith, and R.C. Malone, 1999: Eddies in numerical models of the Antarctic Circumpolar Current and their influence on the mean flow, *J. Phys. Oceanogr.*, **29**, 328-350.

Boebel, O., C. Schmid, G. Podestá, and W. Zenk, 1999: Intermediate water in the Brazil-Malvinas confluence zone: A Lagrangian view. *J. Geophys. Res.*, **104**, 21,062-21,082.

Boer, G.J., G. Flato, M.C. Reader, and D. Ramsden, 2000: A transient climate change simulation with greenhouse gas and aerosol forcing: experimental design and comparison with the instrumental record for the 20th century. *Clim. Dyn.*, **16**, 405-426.

Borowski, D., 1999: Windantrieb und thermohaliner Antrieb des Antarktischen Zirkumpolarstroms - Eine idealisierte numerische Studie. *Diplomarbeit*, University of Bremen, Germany, 81 pp.

Borowski, D., R. Gerdes, and D. Olbers, 2002: Thermohaline and wind forcing of a circumpolar channel with blocked geostrophic contours. *J. Phys. Oceanogr.*, **32**, 2520-2540.

Boville, B.A., and P.R. Gent, 1998: The NCAR Climate System Model, Version one. *J. Climate*, **11**, 1115-1130.

Boville, B.A., J.T. Kiehl, P.J. Rasch, and F.O. Bryan, 2001: Improvements to the NCAR CSM-1 for transient climate simulations. *J. Climate*, **14**, 164-179.

Braconnet, P., O. Marti, S. Joussaume, and Y. Leclainche, 2000: Ocean feedback in response to 6 kyr BP insolation. *J. Climate*, **13**, 1537-1553.

Brix, H., 2001: North Atlantic Deep Water and Antarctic Bottom Water: Their interaction and influence on modes of the global ocean circulation. *Ph.D. dissertation*, University of Bremen, Germany, 138 pp.

Brix, H., and R. Gerdes, 2002: NADW and AABW: Their interaction and influence on the variability of the global ocean circulation. *J. Geophys. Res.*, **108 (C2)**, 3022, doi:10.1029/2002JC001335.

Broecker, W.S., D.M. Peteet, and D. Rind, 1985: Does the ocean-atmosphere system have more than one stable mode of operation? *Nature*, **315**, 21-26.

Broecker, W.S., 1991: The great conveyor. *Oceanogr.*, **4**, 79-89.

Broecker, W.S., 1997: Thermohaline circulation, the Achilles heel of our climate system: Will man-made CO_2 upset the current balance? *Science*, **278**, 1582-1588.

Broecker, W.S., 1998: Paleocean circulation during the last deglaciation: A bipolar seesaw? **Paleoceanogr.**, **13**, 119-121.

Bryan, F., 1986: High-latitude salinity effects and interhemispheric thermohaline circulations. *Nature*, **323**, 301-304.

Bryan, K., and L.J. Lewis, 1979: A water mass model of the world ocean. *J. Geophys. Res.*, **84**, 2503-2517.

Bryan, K., 1984: Accelerating the convergence to equilibrium of ocean-climate models. *J. Phys. Oceanogr.*, **14**, 666-673.

Cai, W., and P.G. Baines, 1996: Interactions between thermohaline- and wind-driven circulations and their relevance to the dynamics of the Antarctic Circumpolar Current in a coarse-resolution global ocean general circulation model. *J. Geophys. Res.*, **101**, 14,073-14,093.

Cane, M.A., V.M. Kamenkovich, A. Krupitsky, 1998: On the utility and disutility of JEBAR, *J. Phys. Oceanogr.*, **28**, 519-526.

Charney, J.G., and J.G. DeVore, 1979: Multiple flow equilibria in the atmosphere and blocking. *J. Atmos. Sci.*, **36**, 1205-1216.

Charney, J.G., D.M. Straus, 1980: Form drag instability, multiple equilibra, and propagating planetary waves in baroclinic, orographically forced, planetary wave systems. *J. Atmos. Sci.*, **37**, 1157-1176.

Cubasch, U., K. Hasselmann, H. Höck, E. Maier-Reimer, U. Mikllolajewicz, B.D. Santer, and R. Sausen, 1992: Time-dependent greenhouse warming computations with a coupled ocean-atmosphere model. *Clim. Dyn.*, **8**, 55-69.

Cubasch, U., R. Voss, G.C. Hegerl, J. Waszkewitz, and T.J. Crowley, 1997: Simulation of the influence of solar radiation variations on the global climate with an ocean-atmosphere general circulation model. *Clim. Dyn.*, **13**, 757-767.

Danabasoglu, G., and J.C. McWilliams, 1995: Sensitivity of the global ocean circulation to parameterizations of mesoscale tracer transport. *J. Climate*, **8**, 2967-2987.

De Ruijter, W.P.M., A. Biastoch, S.S. Drijfhout, J.R.E. Lutjeharms, R.P. Matano, T. Pichevin, P.J. Leeuwen, and W. Weijer, 1999: Indian-Atlantic inter-ocean exchange: Dynamics, estimation and impact. *J. Geophys. Res.*, **104**, 20,885-20,910.

De Szoeke, R.A., and M.D. Levine, 1981: The advective flux of heat by mean geostrophic motions in the Southern Ocean. *Deep Sea Res.*, **28A**, 1057-1085.

Dijkstra, H.A., 2000: Nonlinear physical oceanography, a Dynamical Systems approach to the large scale ocean circulation and El Nino. Kluwer Academic Publishers, 456 pp.

Dijkstra, H.A., H. Oksuzoglu, F.W. Wubs, and E.F.F. Botta, 2001: A fully implicit model of the three-dimensional thermohaline ocean circulation. *J. Comput. Phys.*, **173**, 685-715.

Dixon, K.W., T.L. Delworth, M.J. Spelman, and R.J. Stouffer, 1999: The influence of transient surface fluxes on North Atlantic overturning in a coupled GCM climate change experiment. *Geophys. Res. Lett.*, **26**, No. 17, 2749-2752.

Döös, K., and D.J. Webb, 1994: The Deacon Cell and the other meridional cells of the Southern Ocean. *J. Phys. Oceanogr.*, **24**, 429-442.

Emori, S., T. Nozawa, A. Abe-Ouchi, A. Numaguti, M. Kimoto, and T. Nakajima, 1999: Coupled ocean-atmosphere model experiments of future climate change with an explicit representation of sulfate aerosol scattering, *J. Met. Soc. Japan*, **77**, 1299-1307.

Fieg, K., and R. Gerdes, 2001: Sensitivity of the thermohaline circulation to modern and glacial surface boundary conditions. *J. Geophys. Res.*, **106**, C4, 6853-6867.

Flato, G., G.J. Boer, W.G. Lee, N.A. McFarlane, D. Ramsden, M.C. Reader, and A.J. Weaver, 2000: The Canadian Centre for Climate Modelling and Analysis Global Coupled Model and its climate. *Clim. Dyn.*, **16**, 451-468.

Fine-Resolution Antarctic Model (FRAM) Group, 1991: An eddy-resolving model of the Southern Ocean. *Eos Trans AGU*, **72(169)**, 174-175.

Fritzsch, B., R. Gerdes, W. Hiller, M. Latif, S. Legutke, E. Maier-Reimer, D. Olbers, and F. Roeske, The German OMIP Group, 2000: Vergleich der thermohalinen Zirkulation in zwei globalen ozeanischen Zirkulationsmodellen. The Ocean Model Intercomparison Project. Abschlußbericht BMBF Projekt 01 LA 9862/8. *Berichte aus dem Fachbereich Physik*, Stiftung Alfred-Wegener Institut für Polar- und Meeresforschung, Bremerhaven, Germany, 135 pp.

Ganopolski, A., and S. Rahmstorf, 2001: Rapid changes of glacial climate simulated in a coupled climate model. *Nature*, **409**, 153-158.

Gent, P.R., and J.C. McWillams, 1990: Isopycnal mixing in ocean circulation models. *J. Phys. Oceanogr.*, **20**, 150-155.

Gent, P.R., J. Willebrand, T.J. McDougall, and J.C. McWillams, 1995: Parameterizing eddy-induced tracer transports in ocean circulation models. *J. Phys. Oceanogr.*, **25**, 463-474.

Gent, P.R., W.G. Large, and F.O. Bryan, 2001: What sets the mean transport through Drake Passage? *J. Geophys. Res.*, **106 C2**, 2693-2712.

Gerdes, R., C. Köberle, and J. Willebrand, 1991: The influence of numerical advection schemes on the results of ocean general circulation models. *Clim. Dyn.*, **5**, 211-226.

Gill, A.E., 1968: A linear model of the Antarctic Circumpolar Current, *J. Fluid Mech.*, **32**, 465-488.

Gill, A.E., and K. Bryan, 1971: Effects of geometry on the circulation of a three-dimensional southern-hemisphere ocean model. *Deep-Sea Res.*, **18**, 685-721.

Gille, S.T., 1997: The Southern Ocean momentum balance: Evidence for topographic effects from numerical model output and altimeter data. *J. Phys. Oceanogr.*, **27**, 2219-2232.

Gille, S.T., 1999: Evaluating Southern Ocean response to wind forcing. *Phys. Chem. Earth (A)*, **24**, No. 4, 423-428.

Gille, S.T., D.P. Stevens, R.T. Tokmakian, and K.J. Heywood, 2001: Antarctic Circumpolar Current response to zonally averaged winds. *J. Geophys. Res.*, **106**, C2, 2743-2759.

Gnanadesikan, A., 1999: A simple predictive model for the structure of the oceanic pycnocline. *Science*, **283**, 2077-2079.

Gnanadesikan, A., and R.W. Hallberg, 2000: On the relationship of the Circumpolar Current to southern hemisphere winds in coarse-resolution ocean models. *J. Phys. Oceanogr.*, **30**, 2013-2034.

Godfrey, J.S., 1989: A Sverdrup model of the depth-integrated flow for the world, allowing for island circulations. *Geophys. Astrophys. Fluid Dyn.*, **45**, 89-112.

Goodman, P.J., 1998: The role of North Atlantic Deep Water formation in an OGCM's ventilation and thermohaline circulation. *J. Phys. Oceanogr.*, **28**, 1759-1785.

Gordon, A.L., 1985: Indian-Atlantic transfer of thermocline water at the Agulhas Retroflection. *Science*, **227**, 1030-1033.

Gordon, A.L., 1986: Interocean exchange of thermocline water. *J. Geophys. Res.*, **91**, 5037-5046.

Gordon, A.L., R.F. Weiss, W.M. Smethie Jr., and M.J. Warner, 1992: Thermocline and intermediate water communication between the South Atlantic and Indian Oceans. *J. Geophys. Res.*, **97**, 7223-7240.

Gordon, A.L., 1996: Communication between oceans, *Nature*, **382**, 399-400.

Gordon, C., C. Cooper, C.A. Senior, H.T. Banks, J.M. Gregory, T.C. Johns, J.F.B. Mitchell, and R.A. Woods, 2000: The simulation of SST, sea ice extents and ocean heat transports in a version of the Hadley Centre coupled model without flux adjustments. *Clim. Dyn.*, **16**, 147-168.

Gordon, H.B., and S.P. O'Farrell, 1997: Transient climate change in the CSIRO coupled model with dynamic sea ice. *Mon. Wea. Rev.*, **125**, 875-907.

Green, J.S.A., 1970: Transfer properties of the large-scale eddies and the general circulation of the atmosphere. *Q. J. R. Meteorol. Soc.*, **96**, 157-185.

Guilyardi, E. and G. Madec, 1997: Performance of the OPA/ARPEFE-T-21 global ocean-atmosphere coupled model. *Clim. Dyn.*, **13**, 149-165.

Hallberg, R., and A. Gnanadesikan, 2001: An exploration of the role of transient eddies in determining the transport of a zonally reentrant current. *J. Phys. Oceanogr.*, **31**, 3312-3330.

Harrision, D.E., 1978: On the diffusion parameterization of mesoscale eddy effects from a numerical ocean experiment. *J. Phys. Oceanogr.*, **8**, 913-918.

Hellerman, S., and M. Rosenstein, 1983: Normal monthly stress over the world ocean with error estimates. *J. Phys. Oceanogr.*, **13**, 1093-1104.

Hidaka, K., anf M. Tsuchiya, 1953: On the Antarctic Circumpolar Current. *J. Marine Res.*, **12**, 214-222.

Hogan, T.F., and T. Li, 1997: Long-term simulations with a coupled global atmosphere-ocean prediction system. *NRL Review*, 183-185.

Hughes, C.W., and P.D. Killworth, 1995: Effects of bottom topography in the large-scale circulation of the Southern Ocean. *J. Phys. Oceanogr.*, **25**, 2485-2497.

Hughes, C.W., 1996: The Antarctic Circumpolar Current as a waveguide for Rossby waves. *J. Phys. Oceanogr.*, **26**, 1375-1387.

Hughes, C.W., 1997: Comments on "On the obscurantist physics of "form drag" in theorizing about the Circumpolar Current", *J. Phys. Oceanogr.*, **27**, 209-210.

Hughes, C.W., M.S. Jones, and S. Carnochan, 1998: Use of transient features to identify eastward currents in the Southern Ocean. *J. Geophys. Res.*, **103**, 2929-2944.

Hughes, C.W., 2000: A theoretical reason to expect inviscid western boundary currents in realistic oceans. *Ocean Modelling*, **2**, 73-83.

Hughes, C.W., and E.R. Ash, 2001: Eddy forcing of the mean flow in the Southern Ocean. *J. Geophys. Res.*, **106**, C2, 2713-2722.

Hughes, C.W., and B.A. de Cuevas, 2001: Why western boundary currents in realistic oceans are inviscid: A link between form stress and bottom pressure torques. *J. Phys. Oceanogr.*, **31**, 2871-2885.

Hughes, C.W., 2002: Sverdrup-like theories of the Antarctic Circumpolar Current. *J. Marine Res.*, **60**, 1-17.

Hughes, T.M.C., and A.J. Weaver, 1994: Multiple equilibria of an asymmetric two-basin ocean model. *J. Phys. Oceanogr.*, **24**, 619-637.

Ivchenko, V.O., 1984: On the parameterization of the eddy fluxes of quasi-geostrophic potential vorticity in zonal currents. *Dokl. Acad. Sci. SSSR*, **277 (4)**, 972-976.

Ivchenko, V.O., K.J. Richards, and D.P. Stevens, 1996: The dynamics of the Antarctic Circumpolar Current. *J. Phys. Oceanogr.*, **26**, 753-774.

Ivchenko, V.O., A.M. Treguier, and S.E. Best, 1997: A kinetic energy budget and internal instabilities in the Fine Resolution Antarctic Model. *J. Phys. Oceanogr.*, **27**, 5-22.

Ivchenko, V.O., A.E. Krupitsky, V.M. Kamenkovich, and N.C. Wells, 1999: Modeling the Antarctic Circumpolar Current: A comparison of FRAM and equivalent barotropic model results. *J. Marine Res.*, **57**, 29-45.

James, I.N., 1994: Introduction to circulating atmospheres. Cambridge University Press., 422 pp.

Johns, T.C., 1996: A description of the Second Hadley Centre Coupled Model (HadCM2). *Climate Research Technical Note 71*, Hadley Centre, United Kingdom Meteorological Office, Bracknell Bershire RG12 2SY, United Kindom, 19 pp.

Johns, T.C., R.E. Carnell, J.F. Crossley, J.M. Gregory, J.F.B. Mitchell, C.A. Senior, S.F.B. Tett, and R.A. Wood, 1997: The second Hadley Centre coupled atmosphere-ocean GCM: model description, spinup and validation. *Clim. Dyn.*, **13**, 103-134.

Johnson, G.C., and H.L. Bryden, 1989: On the size of the Antarctic Circumpolar Current. *Deep-Sea Res.*, **36**, 39-53.

Johnson, T.J., R.H. Stewart, C.K. Shum, and B.D. Tapley, 1992: Distribution of Reynolds stress carried by mesoscale variability in the Antarctic Circumpolar Current. *Geophys. Res. Lett.*, **19**, 1201-1204.

Joos, F. G.-K. Plattner, T.F. Stocker, O. Marchal, and A. Schmittner, 1999: Global warming and marine carbon cycle feedbacks on future atmospheric CO_2. *Science*, **284**, 464-467.

Kamenkovich, V.M., 1961: The integration of the marine current theory equations in multiply connected regions. *Doklady Akademii Nauk SSSR*, **138**, 629-631 (Translated from Russian).

Karsten, R.H., H. Jones, and J. Marshall, 2002: The role of eddy transfer in setting the stratification and transport of a Circumpolar Current. *J. Phys. Oceanogr.*, **32**, 39-54.

Karsten, R.H, and J. Marshall, 2002: Constructing the residual circulation of the ACC from observations. J. Phys. Oceanogr., **32**, 3315-3327.

Killworth, P.D., 1992: An equivalent-barotropic mode in the Fine Resolution Antarctic Model. *J. Phys. Oceanogr.*, **22**, 1379-1387.

Killworth, P.D., and M.M. Nanneh, 1994: Isopycnal momentum budget of the Antarctic Circumpolar Current in the Fine Resolution Antarctic Model. *J. Phys. Oceanogr.*, **24**, 1201-1223.

Killworth, P.D., D.B. Chelton, and R.A. de Szoeke, 1997: The speed of observed and theoretical long extratropical planetary waves. *J. Phys. Oceanogr.*, **27**, 1946-1966.

Killworth, P.D., and C.W. Hughes, 2002: The Antarctic Circumpolar Current as a free equivalent-barotropic jet. *J. Marine Res.*, **60**, 19-45.

Krupitsky, A.E., and M.A. Cane, 1994: On topographic pressure drag in a zonal channel. *J. Marine Res.*, **52**, 1-23.

Krupitsky, A.E., V.M. Kamenkovich, N. Naik, and M.A. Cane, 1996: A linear equivalent barotropic model of the Antarctic Circumpolar Current with realistic coastlines and bottom topography. *J. Phys. Oceanogr.*, **26**, 1803-1824.

Kutznetsov, Y.A., 1998 CONTENT - integrated environment for analysis of dynamical systems. Tutorial. 106 pp. Available from ftp://ftp.cwi.nl/pub/CONTENT

Lautent, C., H. Le Treut, Z.X. Li, L. Fairhead, and J.L. Dufresne, 1998: The influence of resolution in simulating inter-annual and inter-decadal variability in a coupled ocean-atmosphere GCM with emphasis over the North Atlantic. *IPSL report N8.*

Lee, M.-M., and A. Coward, 2002: Eddy mass transport for the Southern Ocean in an eddy-permitting global ocean model. *Ocean Modelling*, **5**, 249-266.

Levitus, S., 1982: Climatological atlas of the world ocean. *NOAA Prof. Pap. 13, U. S. Government Printing Office, Washington, D.C.*, 173 pp.

Li, T., and T.F. Hogan, 1999: The role of the annual mean climate on seasonal and interannual variability of the tropical Pacific in a coupled GCM. *J. Climate*, **12**, 780-792.

Losch, M., 2000: Analyse hydrographischer Schnitte mit Satellitenaltimetrie. *Ph.D. dissertation*, University of Bremen, Germany, 138 pp.

Losch, M., and J. Schröter, 2001: Can we use altimetry to estimate the steady state ocean circulation? *submitted to J. Phys. Oceanogr.*

MacCready, P., and P.B. Rhines, 2001: Meridional transport across a zonal channel: topographic localization. *J. Phys. Oceanogr.*, **31**, 1427-1439.

Macdonald, A.M., 1998: The global ocean circulation: a hydrographic estimate and regional analysis. *Prog. Oceanogr.*, **41**, 281-382.

Maltrud, M.E., R.D. Smith, A.J. Semtner, and R.C. Malome, 1998: Global eddy-resolving ocean simulations driven by 1985-1994 atmospheric winds. *J. Geophys. Res.*, **103**, 30,825-30,853.

Manabe, S., R.J. Stouffer, M.J. Spelman, and K. Bryan, 1991: Transient response of a coupled ocean-atmosphere model to gradual changes of atmospheric CO_2. Part I: Annual mean response. *J. Climate*, **4**, 785-818.

Manabe, S., and R.J. Stouffer, 1993: Century-scale effects of increased atmospheric CO_2 on the ocean-atmosphere system. *Nature*, **364**, 215-218.

Manabe, S., and R.J. Stouffer, 1996: Low-frequency variability of surface air temperature in a 1000-year integration of a coupled atmosphere-ocean-land model. *J. Climate*, **9**, 376-393.

Marshall, D.P., 1995a: Influence of topography on the large-scale ocean circulation, *J. Phys. Oceanogr.*, **25**, 1622-1635.

Marshall, D.P., 1995b: Topographic steering of the Antarctic Circumpolar Current. *J. Phys. Oceanogr.*, **25**, 1636-1650.

Marshall, J., D.J. Olbers, H. Ross, and D. Wolf-Gladrow, 1993: Potential vorticity constraints on the dynamics and hydrography of the Southern Ocean. *J. Phys. Oceanogr.*, **23**, 465-487.

Marshall, J., H. Jones, R. Karsten, and R. Wardle, 2002: Can eddies set ocean stratification? *J. Phys. Oceanogr.*, **32**, 26-38.

McAvaney, B.J., C. Covey, S. Joussaume, V. Kattsov, A. Kitoh, W. Ogana, A.J. Pitman, A.J. Weaver, R.A. Woods, Z.-C. Zhao, K. AchutaRao, A. Arking, A. Barnston, R. Betts, C. Bitz, G. Boer, P. Braconnot, A. Broccoli, F. Bryan, M. Claussen, R. Colman, P. Delecluse, A. Del Genio, K. Dixon, P. Duffy, L. Dümenil, M. England, T. Fichefet, G. Flato, J.C. Fyfe, N. Gedney, P. Gent, C. Genthon, J. Gregory, E. Guilyardi, S. Harrison, N. Hasegawa, G. Holland, M. Holland, Y. Jia, P.D. Jones, M. Kageyama, D. Keith, K. Kodera, J. Kutzbach, S. Lambert, S. Legutke, G. Madec, S. Maeda, M.E. Mann, G. Meehl, I. Mokhov, T. Motoi, T. Philips, J. Polcher, G.L. Potter, V. Pope, C. Prentice, G. Roff, F. Semazzi, P. Sellers, D.J. Stensrud, T. Stockdale, R. Stouffer, K.E. Taylor, K. Trenberth, R. Tol, J. Walsh, M. Wild, D. Williamson, S.-P. Xie, X.-H. Zhang, F. Zwiers, Y.Qian (ed), and J. Stone (ed), 2001: Model evaluation. J.T. Houghton, Y. Ding, D.J. Griggs, M. Noguer, P.J. van der Linden, X. Dai, K. Maskell, and C.A. Johnson (eds): *Climate Change 2001: The Scientific Basis.* Contribution of the Working Group I to the Third Assessment Report of the Intergovernmental Panel on Climate Change, Cambridge University Press, 881 pp.

McDermott, D.A., 1996: The regulations of northern overturning by southern hemisphere winds. *J. Phys. Oceanogr.*, **26**, 1234-1255.

McDougall, T.J., and P.C. McIntosh, 2001: The temporal-residual-mean velocity. Part II: Isopycnal interpretation and the tracer momentum equations. *J. Phys. Oceanogr.*, **31**, 1222-1246.

McIntosh, P.C., and T.J. McDougall, 1996: Isopycnal averaging and the residual mean circulation. *J. Phys. Oceanogr.*, **26**, 1655-1660.

McWilliams, J.C., 1977: A note on a consistent quasigeostrophic model in a multiply connected domain. *Dyn. Atmos. Oceans*, **1**, 427-441.

McWilliams, J.C., W.R. Holland, and J.S. Chow, 1978: A description of numerical Antarctic Circumpolar Currents. *Dyn. Atmos. Oceans*, **2**, 213-291.

Meehl, G.A., and W.M. Washington, 1995: Cloud albedo feedback and the super greenhouse effect in a global coupled GCM. *Clim. Dyn.*, **11**, 399-411.

Mertz, G., and D.G. Wright, 1992: Interpretations of the JEBAR term. *J. Phys. Oceanogr.*, **22**, 301-305.

Miller, R.L., and X. Jiang, 1996: Surface energy fluxes and coupled variability in the tropics of a coupled general circulation model. *J. Climate*, **9**, 1599-1620.

Morrow, R., J. Church, R. Coleman, D. Chelton, and N. White, 1992: Eddy momentum flux and its contribution to the Southern Ocean momentum balance. *Nature*, **357**, 482-484.

Morrow, R., R. Coleman, J. Church, and D. Chelton, 1994 Surface eddy momentum flux and velocity variances in the Southern Ocean from Geosat altimetry. *J. Phys. Oceanogr.*, **24**, 2050-2071.

Munk, W.H., and E. Palmén, 1951: Note on the dynamics of the Antarctic Circumpolar Current. *Tellus*, **3**, 53-55.

Munk, W.H., 1966: Abyssal recipes. *Deep-Sea Res.*, **13**, 707-730.

Nowlin, W.D., Jr., and T. Whitworth III, 1977: Structure and transport of the Antarctic Circumpolar Current at Drake Passage from short-term measurements. *J. Phys. Oceanogr.*, **7**, 788-802.

Nowlin, W.D., Jr., and J.M. Klinck, 1986: The physics of the Antarctic Circumpolar Current. *Rev. Geophys.*, **24 No. 3**, 469-491.

Olbers, D.J., M. Wenzel, and J. Willebrand, 1985: The inference of North Atlantic circulation patterns from climatological hydrographic data. *Rev. Geophys.*, **23**, 313-356.

Olbers, D.J., and C. Wübber, 1991: The role of wind an buoyancy forcing of the Antarctic Circumpolar Current. *Strategies for Future Climate Research*, Latif, M. (ed), Max Planck Institut für Meteorologie, Germany, pp 161-191.

Olbers, D.J., V. Gouretsky, G. Seiß, and J. Schröter, 1992a: Hydrographic atlas of the Southern Ocean, Alfred-Wegener-Institut, Bremerhaven. Available from: www.awi-bremerhaven.de/Atlas/SO

Olbers, D.J., C. Wübber, J.-O. Wolff, 1992b: The dynamical balance of wind and buoyancy driven circumpolar currents, *Berichte aus dem Fachbereich Physik*, Alfred-Wegener-Institut für Polar- und Meeresforschung, Germany, 37 pp.

Olbers, D.J., and C. Völker, 1996: Steady states and variability in oceanic zonal flows. *NATOA ASI Series*, **I 44**, Decadal climate variability. Dynamics and predictability. D.L.T. Anderson, and J. Willebrand (eds), 407-443.

Olbers, D.J., 1998: Comments on "On the obscurantist physics of "form drag" in theorizing about the Circumpolar Current". *J. Phys. Oceanogr.*, **28**, 1647-1654.

Olbers, D.J., J.-O. Wolff, and C. Völker, 2000: Eddy fluxes and second-order moment balances for nonhomgeneous quasigeostrophic turbulence in wind-driven zonal flows. *J. Phys. Oceanogr.*, **30**, 1645-1668.

Olbers, D.J., and V.O. Ivchenko, 2001: On the meridional circulation and balance of momentum in the Southern Ocean of POP. *Ocean Dyn.*, **52**, 79-93.

Pacanowski, R.C., 1995: MOM 2 documentation user's guide and reference manual. *GFDL Ocean Technical Report 3*, 232 pp.

Park, Y.-H., and L. Gamberoni, 1997: Cross-frontal exchange of Antarctic Intermediate Water and Antarctic Bottom Water in the Crozet Basin. *Deep-Sea Res. II*, 44, 963-986.

Pedlosky, J., 1996: Ocean circulation theory. *Springer*, 453 pp.

Prentice, I.C., G.D. Farquhar, M.J.R. Fasham, M.L. Goulden, M. Heimann, V.J. Jaramillo, H.S. Kheshgi, C. Le Quérè, R.J. Scholes, D.W.R. Wallace, D. Archer, M.R. Ashmore, O. Aumont, D. Baker, M. Battle, M. Bender, L.P. Bopp, P. Bousquet, K. Caldeira, P. Ciais, P.M. Cox, W. Cramer, F. Dentener, I.G. Enting, C.B. Field, P. Friedlingstein, E.A. Holland, R.A. Houghton, J.I. House, A. Ishida, A.K. Jain, I.A. Janssens, F. Joos, T. Kaminski, C.D. Keeling, R.F. Keeling, D.W. Kicklighter, K.E. Kohfeld, W. Knorr, R. Law, T. Lenton, K. Lindsay, E. Maier-Reimer, A.C. Manning, R.J. Matear, A.D. McGuire, J.M. Melillo, R. Meyer, M. Mund, J.C. Orr, S. Piper, K. Plattner, P.J. Rayner, S. Sitch, R. Slater, S. Taguchi, P.P. Tans, H.Q. Tian, M.F. Weirig, T. Whorf, A. Yool, L. Pitelka (ed), and A. Ramirez Rojas (ed), 2001: The carbon cycle and atmospheric carbon dioxide. J.T. Houghton, Y. Ding, D.J. Griggs, M. Noguer, P.J. van der Linden, X. Dai, K. Maskell, and C.A. Johnson (eds): *Climate Change 2001: The Scientific Basis.* Contribution of the Working Group I to the Third Assessment Report of the Intergovernmental Panel on Climate Change, Cambridge University Press, 881 pp.

Rahmstorf, S., 1994: Rapid climate transitions in a coupled ocean-atmosphere model. *Nature*, **372**, 82-85.

Rahmstorf, S., and M.H. England, 1997: Influence of southern hemisphere winds on North Atlantic Deep Water flow. *J. Phys. Oceanogr.*, **27**, 2040-2054.

Rattray Jr., M., and J.G. Dworski, 1978: The effect of bathymetry on the steady baroclinic ocean circulation. *Dyn. Atmos.-Oceans*, **2**, 321-339.

Rhines, P.B., and W.R. Young, 1982: Homogenization of potential vorticity in planetary gyres. *J. Fluid Mech.*, **122**, 347-367.

Rintoul, S.R., 1991 South Atlantic interbasin exchange. *J. Geophys. Res.*, **96**, C2, 2675-2692.

Rintoul, S.R., and J.L. Bullister, 1999: A late winter hydrographic section from Tasmania to Antarctica. *Deep-Sea Res.*, **46**, 1417-1454.

Rintoul, S.R., C. Hughes, C., and D.J. Olbers, 2001: The Antarctic Circumpolar Current system. *Ocean Circulation and Climate, Academic Press* G. Siedler, J. Church and J. Gould, Eds., 271-302.

Rintoul, S.R., and S. Sokolov, 2001: Baroclinic transport variability of the Antarctic Circumpolar Current south of Australia (WOCE repeat section SR3). *J. Geophys. Res.*, **106 C2**, 2815-2832.

Roeckner, E., J.M. Oberhuber, A. Bacher, M. Christoph, and I. Kirchner, 1996: ENSO variability and atmospheric response in a global coupled atmosphere-ocean GCM. *Clim. Dyn.*, **12**, 737-754.

Samelson, R.M., 1999: Geostrophic circulation in a rectangular basin with a circumpolar connection. *J. Phys. Oceanogr.*, **29**, 3175-3184.

Schmitz Jr., W. J., 1995: On the interbasin-scale thermohaline circulation. *Rev. Geophys.*, **33**, 151-173.

Schneider, E.K., Z. Zhu, B.S. Giese, B. Huang, B.P. Kirtmann, J. Shukla, and J.A. Carton, 1997: Annual cycle and ENSO in a coupled ocean-atmosphere general circulation model. *Mon. Wea. Rev.*, **125**, 680-702.

Schneider, E.K., and Z. Zhu, 1998: Sensitivity of the simulated annual cycle of sea surface temperature in the equatorial Pacific to sunlight penetration. *J. Climate*, **11**, 1932-1950.

Semtner, A.J., and R.M. Chervin, 1992: Ocean general circulation from a global eddy-resolving model. *J. Geophys. Res.*, **97**, 5493-5550.

Smith, R.D., J.K. Dukowicz, R.C. Malone, R. C., 1992: Parallel ocean general circulation modeling. *Physica D*, **60**, 38-61.

Speer, K., S.R. Rintoul, and B. Sloyan, 2000: The diabatic Deacon Cell. *J. Phys. Oceanogr.*, **30**, 3212-3222.

Starr, V.P., 1948: An essay on the gerneral circulation of the earth's atmosphere. *J. Meteor.*, **5**, 39-43.

Stevens, D.P., and V.O. Ivchenko, 1997: The zonal momentum balance in an eddy-resolving general-circulation model of the Southern Ocean. *Q. J. R. Meteorol. Soc.*, **123**, 929-951.

Stocker, T.F., and D.G. Wright, 1991: Rapid transitions of the oceans's deep circulation induced by changes in surface water fluxes. *Nature*, **351**, 729-732.

Stocker, T.F., D.G. Wright, and W.S. Broecker, 1992: The influence of high-latitude surface forcing on the global thermohaline circulation. *Paleoceanogr.*, **7**, 529-541.

Stocker, T.F., and A. Schmittner, 1997: Influence of CO_2 emission rates on the stability of the thermohaline circulation. *Nature*, **388**, 862-865.

Stocker, T.H., 1998: The seesaw effect. *Science*, **282**, 61-62.

Stocker, T.F., and O. Marchal, 2000: Abrupt climate change in the computer: Is it real? *Proceedings of the National Academy of Sciences*, **97**, 1362-1365.

Stocker, T.F., G.K.C. Clarke, H. Le Treut, R.S. Lindzen, V.P. Meleshko, R.K. Mugara, T.N. Palmer, R.T. Pierrehumbert, P.J. Sellers, K.E. Trenberth, J. Willebrand, R.B. Alley, O.E. Anisimov, C. Appenzeller, R.G. Barry, J.J. Bates, R. Bindschadler, G.B. Bonan, C.W. Böning, S. Bony, H. Bryden, M.A. Cane, J.A. Curry, T. Delworth, A.S. Denning, R.E. Dickinson, K. Echelmeyer, K. Emanuel, G. Flato, I. Fung, M. Geller, P.R. Gent, S.M. Griffies, I. Held, A. Henderson-Sellers, A.A.M. Holtslag, F. Hourdin, J.W. Hurrell, V.M. Kattsov, P.D. Killworth, Y. Kushnir, W.G. Large, M. Latif, P. Lemke, M.E. Mann, G. Meehl, U. Mikoljewicz, W. O'Hirok, C.L. Parkinson, A. Payne, A. Pitman, J. Polcher, I. Polyakov, V. Ramaswamy, P.J. Rasch, E.P. Salathe, C. Schär, R.W. Schmitt, T.G. Shepherd, B.J. Soden, R.W. Spencer, P. Taylor, A. Timmermann, K.Y. Vinnikov, M. Visbeck, S.E. Wijffels, M. Wild, S. Manabe (ed.), and P. Mason (ed), 2001: Physical climate processes and feedbacks. J.T. Houghton, Y. Ding, D.J. Griggs, M. Noguer, P.J. van der Linden, X. Dai, K. Maskell, and C.A. Johnson (eds): *Climate Change 2001: The Scientific Basis*. Contribution of the

Working Group I to the Third Assessment Report of the Intergovernmental Panel on Climate Change, Cambridge University Press, 881 pp.

Stommel, H., 1957: A survey of ocean current theory, *Deep-Sea Res.*, **4**, 149-184.

Stommel, H., 1961: Thermohaline convection with two stable regimes of flow. *Tellus*, **13**, 224-230.

Stone, P.H., 1962: A simplified radiative-dynamical model for the static stability of rotary atmospheres. *J. Atmos. Sci.*, **29**, 405-418.

Stone, P.H., 1972: The meridional variation of the eddy heat fluxes by baroclinic waves and their parameterization. *J. Atmos. Sci.*, **31**, 444-456.

Tansley, C.E., and D.P. Marshall, 2001: On the dynamics of wind-driven Circumpolar Currents. *J. Phys. Oceanogr.*, **31**, 3258-3273.

Thompson, S.R., 1993: Estimation of the transport of heat in the Southern Ocean using a fine-resolution numerical model. *J. Phys. Oceanogr.*, **23**, 2493-2497.

Toggweiler, J. R., Samuels, B., 1993: Is the magnitude of the deep outflow from the Atlantic ocean actually governed by southern hemisphere winds? *The global carbon cycle*, M. Heimann (ed.), NATA ASI Series, Springer Verlag, Berlin, Germany, pp 333-366.

Toggweiler, J.R., and B. Samuels, 1995: Effect of Drake Passage on the global thermohaline circulation. *Deep-Sea Res.*, **42**, 477-500.

Toggweiler, J.R., and B. Samuels, 1998: On the oceans large-scale circulation near the limit of no vertical mixing. *J. Phys. Oceanogr.*, **28**, 1832-1852.

Tokioka, T., A. Noda, A. Kitoh, Y. Nikaidou, S. Nakagawa, T. Motoi, S. Yukimoto, and K. Takata, 1996: A transient CO_2 experiment with the MRI CGCM: Annual mean response. *CGER's Supercomputer Monograph Report Vol. 2*, CGER-IO22-96, ISSN 1341-4356, Center for Global Environmental Research, National Institute for Environmental Studies, Environment Agency of Japan, Ibaraki, Japan, 86 pp.

Treguier, A.M., and J.C. McWilliams, 1990: Topographic influences on wind-driven, stratified flow in a β-plane channel: An idealized model for the Antarctic Circumpolar Current. *J. Phys. Oceanogr.*, **20**, 321-343.

Treguier, A.M., 1992: Kinetic energy analysis of an eddy resolving, primitive equation model of the North Atlantic. *J. Geophys. Res.*, **97**, C1, 687-701.

Vallis, G.K., 2000: Large-scale circulation and production of stratification: Effects of wind, geometry, and diffusion. *J. Phys. Oceanogr.*, **30**, 933-954.

Völker, C., 1995: Barokline Strömung über periodischer Topographie: Untersuchungen an analytischen und numerischen Modellen, *Ph.D. dissertation*, Universität Bremen, Germany, 165 pp.

Völker, C., 1999: Momentum balance in zonal flows and resonance of baroclinic Rossby waves. *J. Phys. Oceanogr.*, **29**, 1666-1681.

von Storch, J.-S., 1994: Interdecadal variability in a global coupled model. *Tellus*, **46A**, 419-432.

von Storch, J.-S., V.V. Kharin, U. Cubasch, G.C. Hegerl, D. Schriever, H. von Storch, and E. Zorita, 1997: A description of a 1260-year control integration with the coupled model ECHAM1/LSG general circulation model. *J. Climate*, **10**, 1525-1543.

Voss, R., R. Sausen, and U. Cubasch, 1998: Periodically synchronously coupled integrations with the atmosphere-ocean general circulation model ECHAM3/LSG. *Clim. Dyn.*, **14**, 249-266.

Wang, L., and R.X. Huang, 1995: A linear homogeneous model of wind-driven circulation in a β-plane channel. *J. Phys. Oceanogr.*, **25**, 587-603.

Wardle, R., and J. Marshall, 2000: Representation of eddies in primitive equation models by a PV flux. *J. Phys. Oceanogr.*, **30**, 2481-2503.

Warren, B.A., J.H. LaCasce, and P.E. Robbins, 1996: On the obscurantist physics of "form drag" in theorizing about the Circumpolar Current, *J. Phys. Oceanogr.*, **26**, 2297-2301.

Washington, W.M., and G.A. Meehl, 1996: High-latitude climate change in a global coupled ocean-atmosphere-sea ice model with increased atmospheric CO_2. *J. Geophys. Res.*, **101**(D8), 12795-12801.

Weaver, A.J., and T.M.C. Hughes, 1994: Rapid interglacial climate fluctuations driven by North Atlantic ocean circulation. *Nature*, **367**, 447-450.

Webb, D.J., P.D. Killworth, A.C. Coward, and S.R. Thompson, 1991: The FRAM atlas of the Southern Ocean. Natural Envirnmental Research Council, Swindon, U.K., 67 pp.

Webb, D.J., 1993: A simple model of the effect of the Kerguelen Plateau on the strength of the Antarctic Circumpolar Current. *Geophys. Astrophys. Fluid Dyn.*, **70**, 57-84.

Webb, D.J., A.C. Coward, B.A. de Cuevas, and C.S. Gwillam, 1997: A PVM version of the Bryan-Cox-Semtner ocean general circulation model for use on array processors. *J. Atmos. Ocean. Tech.*, **14**, 175-183.

Weijer, W., W.P.M. de Ruijter, H.A. Dijkstra, and P. J. van Leeuwen, 1999: Impact of interbasin exchange on the Atlantic overturning circulation. *J. Phys. Oceanogr.*, **29**, 2266-2284.

Weijer, W., 2000: Impact of interocean exchange on the Atlantic overturning circulation. *Ph.D. dissertation*, University of Utrecht, Netherlands, 198 pp.

Weijer, W., W.P.M. de Ruijter, and H.A. Dijkstra, 2001: Stability of the Atlantic overturning circulation: competition between Bering Strait freshwater flux and Agulhas heat and salt sources. *J. Phys. Oceanogr.*, **31**, 2385-2402.

Wells, N.C., and B.A. de Cuevas, 1995: Depth-integrated vorticity budget of the Southern Ocean from a general circulation model. *J. Phys. Oceanogr.*, **25**, 2569-2582.

Whitworth III, T., W.D. Nowlin Jr., and S.J. Worley, 1982: The net transport of the Antarctic Circumpolar Current through Drake Passage. *J. Phys. Oceanogr.*, **12**, 960-971.

Whitworth III, T., 1983: Monitoring the transport of the Antarctic Circumpolar Current at Drake Passage. *J. Phys. Oceanogr.*, **13**, 2045-2057.

Whitworth III, T., and R.G. Peterson, 1985: Volume transport of the Antarctic Circumpolar Current from bottom pressure measurements. *J. Phys. Oceanogr.*, **15**, 810-816.

Wolff, J.-O., 1990: Zur Dynamik des Antarktischen Zirkumpolarstromes. *Dissertation*, University of Hamburg, Germany, 137 pp.

Wolff, J.-O., E. Maier-Reimer, and D.J. Olbers, 1991: Wind-driven flow over topography in a zonal β-plane channel: a quasi-geostrophic model of the Antarctic Circumpolar Current. *J. Phys. Oceanogr.*, **21**, 236-264.

Wolff, J.-O., 1999: Modelling the Antarctic Circumpolar Current: eddy-dynamics and their parametrization. *Environmental Modelling & Software*, **14**, 317-326.

Wu, G.-X., X.-H. Zhang, H. Liu, Y.-Q. Yu, X.-Z. Jin, Y.-F. Guo, S.-F. Sun, and W.-P. Li, 1997: Global ocean-atmosphere-land system model of LASG (GOALS/LASG) and its performance in simulation study. *Quart. J. of Appl. Meteor.*, **8**, Supp., 15-28 (in Chinese).

Yaremchuk, M., N.L. Bindoff, J. Schröter, D. Nechaev, and S.R. Rintoul, 2001: On the zonal and meridional circulation and ocean transport between Tasmania and Antarctica. *J. Geophys. Res.*, **106 C2**, 2795-2814.

Yukimoto, S., M. Endoh, Y. Kitamura, A. Kitoh, T. Motoi, and A. Noda, 2000: ENSO-like interdecadal variability in the Pacific Ocean as simulated in a coupled GCM. *J. Geophys. Res.*, **105**, 13945-13963.

Zhang, W.-H., G.-Y. Shi, H. Liu, and Y.-Q. Yu (eds), 2000: IAP Global Atmosphere-Land System Model. Science Press, Beijing, China, 259 pp.